

# Efficient laser-driven proton acceleration in the ultra-short pulse regime

## D I S S E R T A T I O N

zur Erlangung des akademischen Grades

**Doctor rerum naturalium**

(Dr. rer. nat.)

vorgelegt der

**Fakultät Mathematik und Naturwissenschaften  
der Technischen Universität Dresden**

von

Dipl. Phys. Karl Zeil

geboren am 02.02.1982 in Dresden

eingereicht am 15.02.2013

Tag der Verteidigung 20.06.2013

Die Dissertation wurde in der Zeit von 03/2007 bis 01/2013

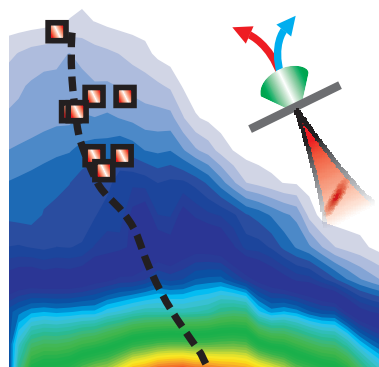
am Helmholtz-Zentrum Dresden-Rossendorf

im Institut für Strahlenphysik angefertigt

1. Gutachter: *Prof. Dr. Roland Sauerbrey*
2. Gutachter: *Prof. Dr. Jörg Schreiber*



# Abstract



The work described in this thesis is concerned with the experimental investigation of the acceleration of high energy proton pulses generated by relativistic laser-plasma interaction and their application. Using the high intensity 150 TW Ti:sapphire based ultra-short pulse laser Draco, a laser-driven proton source was set up and characterized. Conducting experiments on the basis of the established target-normal sheath acceleration (TNSA) process, proton energies of up to 20 MeV were obtained. The reliable performance of the proton source was demonstrated in the first direct

and dose controlled comparison of the radiobiological effectiveness of intense proton pulses with that of conventionally generated continuous proton beams for the irradiation of *in vitro* tumour cells. As potential application radiation therapy calls for proton energies exceeding 200 MeV. Therefore the scaling of the maximum proton energy with laser power was investigated and observed to be near-linear for the case of ultra-short laser pulses. This result is attributed to the efficient predominantly quasi-static acceleration in the short acceleration period close to the target rear surface. This assumption is furthermore confirmed by the observation of prominent non-target-normal emission of energetic protons reflecting an asymmetry in the field distribution of promptly accelerated electrons generated by using oblique laser incidence or angularly chirped laser pulses. Supported by numerical simulations, this novel diagnostic reveals the relevance of the initial prethermal phase of the acceleration process preceding the thermal plasma sheath expansion of TNSA. During the plasma expansion phase, the efficiency of the proton acceleration can be improved using so called reduced mass targets (RMT). By confining the lateral target size which avoids the dilution of the expanding sheath and thus increases the strength of the accelerating sheath fields a significant increase of the proton energy and the proton yield was observed.

# Zusammenfassung

Diese Doktorarbeit beschäftigt sich mit Experimenten zur Beschleunigung hochenergetischer Protonenpulse, erzeugt durch relativistische Laser-Plasma-Wechselwirkung und deren Anwendung. Mit Hilfe des hoch intensiven, Ti:Sa basierten 150 TW Kurzpuls-Lasersystems Draco wurde eine lasergetriebene Protonenquelle realisiert und charakterisiert. Auf Basis des etablierten TNSA (target-normal sheath acceleration) Prozesses konnten mit diesem System Protonenenergien bis zu 20 MeV erzeugt werden. Mit Durchführung eines Vergleiches zur strahlenbiologischen Wirkung von intensiven Protonenpulsen und konventionell erzeugten Protonenstrahlen bei der dosiskontrollierten *in vitro* Bestrahlung von Tumorzellen, konnte zudem die zuverlässige Funktion der Protonenquelle nachgewiesen werden. Da die Strahlentherapie als mögliches Anwendungsgebiet Protonenenergien über 200 MeV erfordert, wurde die Skalierung der maximalen Protonenenergie mit der Laserleistung für den Fall ultrakurzer Laserpulse untersucht und ein nahezu lineares Verhalten beobachtet. Dieses Resultat wurde einer effizienten, vorwiegend quasi-statischen Beschleunigung in der kurzen Beschleunigungsperiode nahe der Targetrückseite zugeschrieben. Bestätigt werden konnte diese Annahme durch eine weitere Beobachtung: Schräger Lasereinfall oder die Einführung eines Winkelchirps führen zu asymmetrischer Verteilung der direkt vom Laser beschleunigten Elektronen, was eine auffällige Ablenkung der hochenergetischen Protonen von der Targetnormalen zur Folge hat. Unterstützt durch numerische Simulationen offenbart diese neue Methode die hohe Bedeutung der „vorthermischen“ Anfangsphase des TNSA-Beschleunigungsprozesses, die der thermischen Expansion des heißen Plasmas vorangeht. Während der Expansionsphase kann die Effizienz der Protonenbeschleunigung zusätzlich mit sogenannten masse-reduzierten Targets verbessert werden. Durch Einschränkung der lateralen Targetgröße, was die Ausdünnung des expandierenden Plasmas verhindert und damit zu einer Erhöhung der elektrischen Feldstärke führt, konnte eine signifikante Erhöhung der Protonenenergie und der Protonenausbeute beobachtet werden.

# Publications by the author

## Important parts of this thesis are treated in the following publications

K. Zeil, J. Metzkes, T. Kluge, M. Bussmann, T.E. Cowan, S.D. Kraft, R. Sauerbrey, and U. Schramm. Direct observation of prompt pre-thermal laser ion sheath acceleration. *Nature Communications*, 3:874, 2012.

K. Zeil, M. Baumann, E. Beyreuther, T. Burris-Mog, T.E. Cowan, W. Enghardt, L. Karsch, S.D. Kraft, L. Laschinsky, J. Metzkes, D. Naumburger, M. Oppelt, C. Richter, R. Sauerbrey, M. Schürer, U. Schramm, and J. Pawelke. Dose-controlled irradiation of cancer cells with laser-accelerated proton pulses. *Applied Physics B*, pages 1–8, 2012.

J. Metzkes, L. Karsch, S.D. Kraft, J. Pawelke, C. Richter, M. Schürer, M. Sobiella, N. Stiller, K. Zeil, and U. Schramm. A scintillator-based online detector for the angularly resolved measurement of laser-accelerated proton spectra. *Review of Scientific Instruments*, 83(12):123301–123301–7, 2012.

J. Metzkes, T.E. Cowan, L. Karsch, S.D. Kraft, J. Pawelke, C. Richter, T. Richter, K. Zeil, and U. Schramm. Preparation of laser-accelerated proton beams for radiobiological applications. *Nuclear Instruments and Methods in Physics Research Section A: Accelerators, Spectrometers, Detectors and Associated Equipment*, 653(1):172–175, 2011.

K. Zeil, S.D. Kraft, S. Bock, M. Bussmann, T.E. Cowan, T. Kluge, J. Metzkes, T. Richter, R. Sauerbrey, and U. Schramm. The scaling of proton energies in ultrashort pulse laser plasma acceleration. *New Journal of Physics*, 12(4):045015, 2010.

S.D. Kraft, C. Richter, K. Zeil, M. Baumann, E. Beyreuther, S. Bock, M. Bussmann, T.E. Cowan, Y. Dammene, W. Enghardt, U. Helbig, L. Karsch, T. Kluge, L. Laschinsky, E. Lessmann, J. Metzkes, D. Naumburger, R. Sauerbrey, M. Schürer, M. Sobiella, J. Woithe, U. Schramm, and J. Pawelke. Dose dependent biological damage of tumour cells by laser-accelerated proton beams. *New Journal of Physics*, 12:085003, 2010.

S. Buffechoux, J. Psikal, M. Nakatsutsumi, L. Romagnani, A. Andreev, K. Zeil, M. Amin, P. Antici, T. Burris-Mog, A. Compant-La-Fontaine, E. d’Humières, S. Fourmaux, S. Gaillard, F. Gobet, F. Hannachi, S. Kraft, A. Mancic, C. Plaisir, G. Sarri, M. Tarisien, T. Toncian,

U. Schramm, M. Tampo, P. Audebert, O. Willi, T.E. Cowan, H. Pépin, V. Tikhonchuk, M. Borghesi, and J. Fuchs. Hot electrons transverse refluxing in ultraintense laser-solid interactions. *Physical Review Letters*, 105:015005, 2010.

K. Zeil, S.D. Kraft, A. Jochmann, F. Kroll, W. Jahr, U. Schramm, L. Karsch, J. Pawelke, B. Hidding, and G. Pretzler. Absolute response of Fuji imaging plate detectors to picosecond-electron bunches. *Review of Scientific Instruments*, 81(1):013307, 2010.

A. Buck, K. Zeil, A. Popp, K. Schmid, A. Jochmann, S.D. Kraft, B. Hidding, T. Kudyakov, C.M.S. Sears, L. Veisz, S. Karsch, J. Pawelke, R. Sauerbrey, T. Cowan, F. Krausz, and U. Schramm. Absolute charge calibration of scintillating screens for relativistic electron detection. *Review of Scientific Instruments*, 81(3):033301, 2010.

### **Furthermore, the author contributed to the following publications**

L. Karsch, E. Beyreuther, T. Burris-Mog, S.D. Kraft, C. Richter, K. Zeil, and J. Pawelke. Dose rate dependence for different dosimeters and detectors: TLD, OSL, EBT films, and diamond detectors. *Medical Physics*, 39(5):2447–2455, 2012.

T. Kluge, S.A. Gaillard, K.A. Flippo, T. Burris-Mog, W. Enghardt, B. Gall, M. Geissel, A. Helm, S.D. Kraft, T. Lockard, J. Metzkes, D.T. Offermann, M. Schollmeier, U. Schramm, K. Zeil, M. Bussmann, and T.E. Cowan. High proton energies from cone targets: electron acceleration mechanisms. *New Journal of Physics*, 14(2):023038, 2012.

T. Kluge, T. Cowan, A. Debus, U. Schramm, K. Zeil, and M. Bussmann. Electron temperature scaling in laser interaction with solids. *Physical Review Letters*, 107(20):205003, 2011.

C. Richter, L. Karsch, Y. Dammene, S.D. Kraft, J. Metzkes, U. Schramm, M. Schürer, M. Sobiella, A. Weber, K. Zeil, and J. Pawelke. A dosimetric system for quantitative cell irradiation experiments with laser-accelerated protons. *Physics in Medicine and Biology*, 56(6):1529, 2011.

U. Schramm, K. Zeil, C. Richter, E. Beyreuther, M. Bussmann, T.E. Cowan, W. Enghardt, L. Karsch, T. Kluge, S. Kraft, L. Laschinsky, J. Metzkes, D. Naumburger, J. Pawelke, and R. Sauerbrey Ultrashort pulse laser accelerated proton beams for first radiobiological applications. *AIP Conference Proceedings*, 1299(1):731-736, 2010.

T. Kluge, W. Enghardt, S.D. Kraft, U. Schramm, K. Zeil, T.E. Cowan, and M. Bussmann. Enhanced laser ion acceleration from mass-limited foils. *Physics of Plasmas*, 17:123103, 2010.

T. Kluge, W. Enghardt, S. D. Kraft, U. Schramm, Y. Sentoku, K. Zeil, T.E. Cowan, R. Sauerbrey, and M. Bussmann. Efficient laser-ion acceleration from closely stacked ultrathin foils. *Physical Review E*, 82(1):016405, 2010.

T. Kudyakov, A. Jochmann, K. Zeil, S. Kraft, K.H. Finken, U. Schramm, and O. Willi. High energy electron crystal spectrometer. *Review of Scientific Instruments*, 80(7):076106–076106–3, 2009.

K. Zeil, E. Beyreuther, E. Lessmann, W. Wagner, and J. Pawelke. Cell irradiation setup and dosimetry for radiobiological studies at ELBE. *Nuclear Instruments and Methods in Physics Research Section B: Beam Interactions with Materials and Atoms*, 267(14):2403 – 2410, 2009.

W. Wagner, B. Azadegan, M. Sobiella, J. Steiner, K. Zeil, and J. Pawelke. An intense channeling radiation source. *Nuclear Instruments and Methods in Physics Research Section B: Beam Interactions with Materials and Atoms*, 266(2):327 – 334, 2008.





# Contents

<b>Abstract</b>	<b>i</b>
<b>Zusammenfassung</b>	<b>ii</b>
<b>Publications by the author</b>	<b>iii</b>
<b>1. Introduction</b>	<b>1</b>
<b>2. Laser-driven proton beam delivery for radio-biological studies</b>	<b>6</b>
2.1. The Draco laser system . . . . .	11
2.2. Setup of the laser proton source for cell irradiation studies . . . . .	15
2.2.1. Proton beam generation . . . . .	16
2.2.2. Long-term performance of the laser-driven proton beam . . . . .	20
2.2.3. Cell irradiation setup . . . . .	21
2.3. Results of the <i>in vitro</i> cell irradiation study . . . . .	23
2.4. Summary and future perspectives . . . . .	26
<b>3. Efficient proton acceleration with ultra-short laser pulses</b>	<b>29</b>
3.1. Ion acceleration from thin foils in the TNSA regime . . . . .	32
3.1.1. Plasma expansion model . . . . .	37
3.1.2. Hot electron generation . . . . .	39
3.1.3. Quasi-static description and the novel case of ultra-short laser pulses	42
3.2. The intra-pulse phase . . . . .	49
3.2.1. Non-target-normal proton beam emission . . . . .	49
3.2.2. Proton beam steering by an engineered laser pulse front tilt . . . . .	54
3.2.3. Effects of different laser parameters onto the maximum proton energy	59
3.2.4. Alternative beam-steering by prepulse induced target pre-deformations	63
3.3. Conclusion and outlook - Achieving proton energies relevant for therapy . . .	66
<b>4. The reduced mass target approach</b>	<b>69</b>
4.1. Experimental setup . . . . .	72
4.2. Experimental results . . . . .	74
4.3. Simulation of preformed plasma and proton source size . . . . .	77
4.4. Influence of target edges and mounting structure . . . . .	82

4.5. Summary . . . . .	85
<b>5. Conclusion</b>	<b>87</b>
<b>A. Coupling of spatio-temporal distortions</b>	<b>90</b>
<b>B. Influence of the target material</b>	<b>94</b>
<b>Bibliography</b>	<b>95</b>

# List of Figures

1.1. Sketch of target-normal sheath acceleration . . . . .	2
2.1. Motivation of particle therapy . . . . .	7
2.2. The Draco laser system: setup, diagnostics and target chamber . . . . .	12
2.3. Experimental setup in the target chamber . . . . .	17
2.4. Typical output of the proton detectors . . . . .	18
2.5. Stability of the laser-proton radiation source . . . . .	20
2.6. Setup of the cell irradiation experiment . . . . .	21
2.7. Results of cell irradiation . . . . .	24
2.8. Shot-to-shot dose variations . . . . .	26
2.9. Design of an <i>in vivo</i> experiment at Draco . . . . .	27
3.1. The physical picture of the TNSA mechanism . . . . .	32
3.2. Scaling of the hot electron temperature with laser intensity . . . . .	41
3.3. Scaling of the maximum proton energy with laser power . . . . .	43
3.4. Linear plot of proton energy as function of laser power . . . . .	45
3.5. Illustration of the change in the scaling behavior . . . . .	47
3.6. Approximation parameter $\tau_L/2\tau_0$ plotted as function of the laser energy . . . . .	48
3.7. Spatial energy distribution of laser-accelerated proton beams . . . . .	50
3.8. Input of the 2D PICLS simulation closely resembling the experiment . . . . .	51
3.9. Modelling of the intra-pulse acceleration dynamic . . . . .	52
3.10. Evolution of the maximum proton energy with time . . . . .	53
3.11. Test experiment with angularly chirped laser pulses . . . . .	54
3.12. Temporal contrast curves for corresponding configuration of $\varepsilon$ . . . . .	55
3.13. Origin of pulse front tilt in the laser-matter interaction . . . . .	56
3.14. Influence of spatial chirp on pulse duration and pulse front tilt . . . . .	56
3.15. Spectral decomposition of a short laser pulse in the focal plane . . . . .	57
3.16. Simulated plasma density distribution after prepulse interaction with target . . . . .	59
3.17. Maximum proton energy as function of laser incidence angle and polarization . . . . .	60
3.18. Influence of temporal pulse contrast on maximum proton energy scaling . . . . .	62
3.19. Proton acceleration from a foil target after shock wave deformation . . . . .	64
3.20. Comparison of proton energy scaling models . . . . .	68
4.1. Principle of TNSA when applying reduced mass targets . . . . .	70

---

4.2. Proton energy as function of target surface size obtained at 100 TW LULI . . . . .	71
4.3. Experimental setup and design of reduced mass targets . . . . .	72
4.4. Results of experiments with small gold disk targets with different thickness . . . . .	75
4.5. Hot electron refluxing and homogenization of the electron sheath . . . . .	76
4.6. Simulation of preplasma conditions as function of lateral target size . . . . .	78
4.7. Simulated spatial proton emission distribution for different target sizes . . . . .	80
4.8. Influence of electric fields at target edges on proton emission distribution . . . . .	82
4.9. Maximum proton energy as function of the target mounting geometry . . . . .	84
4.10. Increase of proton dose per pulse when using small gold disk targets . . . . .	86
A.1. Lens performing a Fourier transform operation . . . . .	92
B.1. Proton energy as function of the target material . . . . .	94

# 1. Introduction

Laser based acceleration of charged particles has recently attracted considerable interest. Due to the extreme fields intense laser light generates during the interaction with matter, a hot plasma is formed in which particles can gain high kinetic energies in the gigaelectronvolt range for electrons and tens of megaelectronvolts per nucleon for ions. This is possible, because with the invention of the chirped-pulse amplification (CPA) technique [1] in the 1980s modern high power lasers (10 TW - 1 PW) are capable of providing laser intensities in the range of  $10^{18} - 10^{22} \text{W/cm}^2$  in the laboratory. Since electrons, oscillating in such intense laser fields that reach the order of teravolts-per-meter, may gain a kinetic energy that is in the order of the electron rest mass within half a laser period, these light intensities are called 'relativistic' and also give the research field of relativistic laser-plasma physics its name.

In contrast to that, ions, possessing a much higher inert mass, cannot gain relativistic kinetic energies from the laser field directly. This would require laser intensities in the order of  $10^{24} \text{W/cm}^2$ , a technology that is presently not available. However, during the interaction of a high intensity laser pulse with a solid or near-solid density target it is possible to partially transfer the electron energy to the heavier ions and to efficiently accelerate them.

The most common concept to describe laser-driven ion acceleration is target-normal sheath acceleration (TNSA) introduced by Wilks *et al.* [2]. A sketch illustrating an experiment in the TNSA regime is shown in Fig. 1.1(a). Such experiments are conducted in vacuum and as hydrogen is always present in the contaminants at the surfaces of the laser targets, micrometer thick metal foils in the most simple case, most experiments focus on proton acceleration. At the laser illuminated target front side, the laser generates a plasma, where laser energy is absorbed and hot plasma electrons are pushed into the target. The electrons propagate through the foil and exit at the rear side, forming an electron cloud, called Debye sheath. As a result, a large quasi-static electric field is set up ( $\sim \text{TV/m}$ ) that leads to ionization of the light ions at the target surface (hydrogen, carbon) and that accelerates these ions to megaelectronvolt energy into target-normal direction. In general, the field strength increases with electron density and the average kinetic energy of the electrons in the thermal sheath, whereas the latter is usually referred to as the hot electron temperature of the plasma. The plasma then expands [3] in longitudinal and transverse directions leading to a continuous decrease in electron density and temperature, while energy is transferred to the proton ensemble.

A representative proton spectrum obtained with the 150 TW ultra-short pulse laser system Draco (**D**resden **L**aser **A**cceleration **S**ource) is presented in Fig. 1.1(b), showing the broad

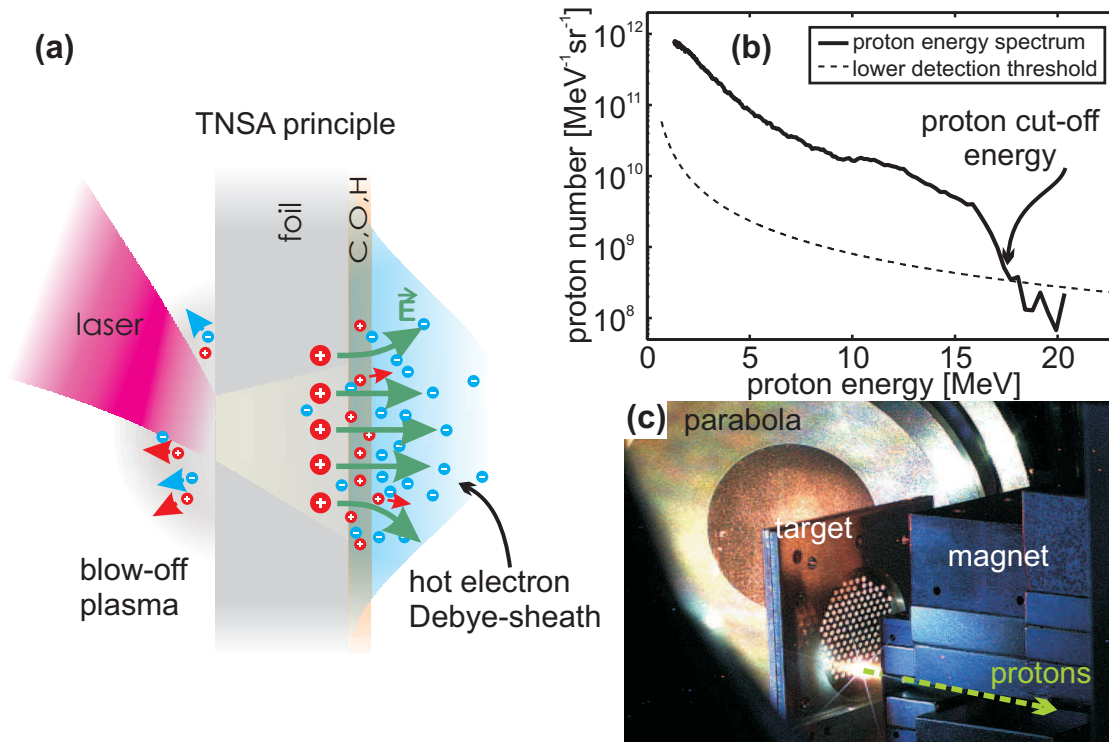


**Fig. 1.1.:** (a) Schematic presentation of the TNSA process. The laser irradiates the target front surface and the extreme electric field strength of the laser generates a plasma in which energetic electrons are accelerated. Those electrons propagate through the foil and leave it at the rear side, forming an electron cloud, the hot electron Debye sheath. This leads to a large quasi-static electric field and thus ionization of light ions in the contaminant layer and to acceleration of those ions to megaelectronvolt energy. The typical spectrum measured with a magnetic spectrometer in (b) shows a broad exponentially decaying energy distribution with a cut-off energy around 17 MeV. (c) Photograph depicts the relativistic laser-matter interaction at the instant of a single laser shot of the Draco laser system. Focused by an off-axis parabolic mirror (visible in the background), the laser beam irradiates a titanium target foil mounted in a frame, visible in the center of the picture. In the generated plasma flash, that illuminates the parabola, energetic protons (green arrow) are accelerated and propagate through an energy selective magnetic filter used in the cell irradiation experiment to be presented in chapter 2.

energy distribution that is typical for TNSA. The hard cut-off of the spectrum (here at 17 MeV) is characteristic for the maximum available accelerating field, and therefore widely used to study the acceleration process as function of the different laser and target parameters. The unique properties of laser-driven proton pulses, such as the high bunch charge at initially short pulse duration and the excellent beam optical quality [4] triggered the discussion about potential applications. Laser-driven proton pulses could be used as probes for electric fields in laser-driven inertial confinement fusion [5] and in relativistic laser-plasma research [6, 7], where the large energy bandwidth even allows for improved time mapping by the correlation between time-of-flight and energy. The high charge of the pulses combined with the excellent transverse emittance further motivates the injection of laser-accelerated bunches into synchrotrons [8, 9, 10, 11].

Especially important for the scope of this thesis is the potential medical application, namely the application of the laser-driven accelerator technique for the development of compact proton sources for radiation therapy [12, 13, 14, 15, 16, 17]. Radiation therapy, however, requires proton energies of up to 250 MeV at a dose rate of a few Gy per minute and thus a pulse repetition rate at least of the order of 1 Hz. Thereby the crucial and still unresolved issue is the need for an increase in maximum particle energy. At present, maximum proton energies achieved with high-energy high-power lasers operating in single pulse mode range to around 70 MeV [18]. Although the radiation doses available in such single pulses seem promising for use in this field, the average achievable current, and thus the pulse repetition rate has to be improved. Only with the recent generation of table-top 100 TW Ti:Sapphire lasers, operating at pulse repetition rates of up to 10 Hz, energies exceeding 10 MeV (for references see Sec. 3.1.3) became accessible for applications where also the average dose rate is of interest, e.g., for providing sufficiently short treatment duration of a few minutes.

To identify feasible routes toward high proton energies at reasonable pulse repetition rates, the underlying physics for the established TNSA process [19, 20] but also for novel acceleration processes, such as the relativistic transparency regime [21, 22, 23, 24] or the radiation pressure dominated acceleration regime [25, 26, 27, 28, 29, 30, 31] are presently under systematic evaluation. This is in particular important for further laser development which, of course, is equally indispensable for the development of devices suitable for medical applications as the demonstration of the competitiveness of the laser-plasma accelerator with conventional sources in terms of precision, reliability and reproducibility imposing enormous technical challenges as well.

## Structure of the thesis

The first task of this thesis was the development of a setup for the generation of a reliable laser-driven proton source at the Draco laser system. Draco is a 150 TW Ti:Sapphire based high intensity laser that was installed at the HZDR in 2008 and that provides ultra-short pulses (30 fs) when tightly focused (focal spot around  $3\ \mu\text{m}$  FWHM) leading to intensities on target of up to  $10^{21}\text{W}/\text{cm}^2$ , and in addition, excellent temporal pulse contrast in the order of  $10^{-10}$ . In parallel to the obvious purpose of the laser-driven proton beam to conduct experiments on fundamental questions of the laser-plasma interaction with solid targets, of particular importance was the demonstration of the source in a real application, here a systematic radiobiological study of radiation induced biological damage based on an *in vitro* cell system. Such an application imposes strict requirements not only on basic proton beam parameters such as sufficiently high proton energy ( $> 10\ \text{MeV}$ ), proton yield and pulse repetition rate but calls also for high reproducibility, reliability and therefore stable and automated operation of the source.

Therefore in the first part of this thesis (chapter 2) an overview of the Draco laser chain, including the diagnostic of the laser pulse parameters achieved on target will be given and the implemented setup for the proton beam generation and the detector systems necessary

for the characterization of the proton beam parameters are introduced. Using the TNSA acceleration mechanism, an optimal target and laser configuration is presented that was used for the first dose-controlled irradiation of *in vitro* cancer cells successfully performed with laser-accelerated proton pulses. Parts of this highly multidisciplinary study, predominantly concerning the implementation of online and offline dosimetry and the radiobiological methods were conducted within a close collaboration with the onCOOPtics project (Zentren für Innovationskompetenz-Verbundprojekt: „onCOOPtics - Hochintensitätslaser für die Radioonkologie“).

Independent from the medical application, but taking the introduced source of stable proton beams as a reference to correlate measurements conducted in different campaigns, the thesis will then focus on the fundamental physics question of how to increase the proton energy. This is necessary for the next level of radiobiological studies, such as the irradiation of tumors in animals (*in vivo*), and it is mandatory for clinical application of laser-driven proton beams in the near future. Yet, TNSA remains the most simple and robust approach guaranteeing highest proton energy for given laser parameters and thus scaling this mechanism by direct increase of laser power presently seems to be the most effective way to reach higher proton energies. Therefore, the experiments conducted in this thesis were mainly focused on TNSA using micrometer thick targets and related effects.

After a brief revision of the theoretical concepts of TNSA (Sec. 3.1), in chapter 3 the proton energy scaling with laser power for the particular case of ultra-short laser pulses (Sec. 3.1.3) and the implication of the ultra-short time-scale onto the underlying physics of the acceleration mechanism will be addressed. It will be shown, that protons efficiently gain energy during the ultra-short initial period, the intra-pulse phase, of the acceleration process (Sec. 3.2) and that this matter of fact has certain implications for optimization procedures and intensity scalings. To identify the intra-pulse acceleration phase, prominent non-target-normal emission of energetic protons is used. This reflects an engineered asymmetry in the field distribution of promptly accelerated electrons during the laser-plasma interaction induced by applying oblique laser incidence or angularly chirped laser pulses. The concept of this novel method is discussed with the help of particle-in-cell simulations as well as experimental results obtained for the investigation of the influence of various laser parameters, such as angle of laser incidence on target, laser polarization, laser pulse energy and temporal laser pulse contrast (Sec. 3.2.2, 3.2.3, 3.2.4).

TNSA is described as an expansion of the plasma sheath surrounding the target, that drives the proton acceleration. Therefore the maximum acceleration is limited due to the rarefaction of the plasma in the longitudinal and transverse directions with time, leading to a continuous decrease in electron density and temperature. One promising approach to circumvent this problem is the confinement of the lateral target surface, as will be the main topic of chapter 4. By using reduced mass targets (RMT), the electron spreading along the target surface is restricted, leading to a time-averaged hotter and denser plasma sheath that improves the conditions for efficient proton acceleration.



Based on lithographic technology, reduced mass targets with different lateral size, thickness and mount geometry were developed in order to study their laser-proton acceleration performance as function of the target geometry. Irradiating the targets with Draco laser pulses results in enhanced proton energy and proton yield when comparing with results obtained with planar foils. In particular, the experimental investigation of the target thickness dependence reveals that the proton energy increase depends on the target thickness representing a novel signature to describe the functionality of this target concept.

## 2. Realization of a laser-driven proton beam delivery system for radio-biological studies

Cancer represents the second highest cause of death in industrial societies. Today, at a steadily increasing rate, already more than 50% of all cancer patients are treated with photon or electron radiotherapy during the course of their disease. Radiotherapy by protons or heavier ion beams, due to their inverse depth dose profile (Bragg peak, see Fig. 2.1), can achieve better physical dose distributions than the most modern photon therapy approaches. In the case of ions heavier than protons, the higher relative radiobiological effectiveness [32, 33] might be of additional therapeutic benefit. It is estimated that at least 10-20% of all radiotherapy patients may benefit from proton or light ion therapy [34, 35] and indications are currently evaluated in clinical trials worldwide. Yet, making widespread use of this potential calls for very high levels of clinical expertise and quality control as well as for enormous economical investment and running costs associated with large-scale accelerator facilities. The former point is presently being addressed in clinical research with, e.g., advanced real-time motion compensation techniques, while the latter asks for more compact and cost-effective yet equally reliable particle accelerators.

As a promising alternative to conventional proton sources, compact laser-plasma based accelerators have been suggested [12, 13, 14, 36, 15, 16, 17], which yield unsurpassed accelerating field gradients in the megavolt per micrometer range. Furthermore, high power laser systems could not only provide laser-driven proton radiation (LDPR) with a high pulse dose rate for therapeutic purposes, but diagnostic radiation as well. This combination could enable novel schemes of image guided radiotherapy, in particular for the irradiation of moving targets.

As already discussed in chapter 1 LDPR originates from hydrogenated contaminants on almost any solid target surface when irradiated with sufficiently intense laser pulses [2]. Electrons are heated to megaelectronvolt temperatures during the interaction, and driven out of the target volume. In the corresponding electric field, the protons at the surface efficiently gain energy. Over the last decade, intense proton pulses with energies exceeding several 10 MeV have been reached with large single-shot laser facilities. Yet, only with the recent generation of table-top 100 TW Ti:Sapphire lasers, operating at pulse repetition rates of up to 10 Hz, energies exceeding 10 MeV [19, 37, 29, 38] (see also chapter 3) became

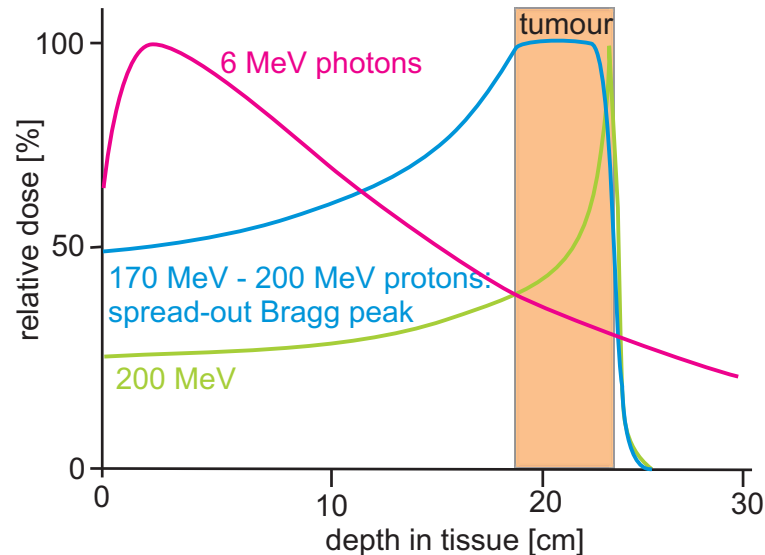


**Fig. 2.1.:** *Motivation of particle therapy. The advantage of using protons or heavier ions for radiotherapy in comparison to widely used X-rays or electrons can easily be understood by the different energy transfer characteristics shown in the picture. In matter, protons and heavier ions show only little spatial scattering, and in contrast to electrons and X-ray radiation, the dominant part of their kinetic energy is deposited close to the end of their trajectory in the well-known Bragg peak, here spread-out Bragg peak when a certain range of proton energies is applied. This feature allows for a more precise irradiation of a tumor at a considerably reduced dose deposition in healthy surrounding tissue.*

accessible for applications where also the average dose rate is of interest, e.g., for providing sufficiently short treatment duration of a few minutes. For the anticipated future application in radiation therapy a further increase in the proton energy of up to 200-250 MeV is required, which is currently addressed by the investigation of novel acceleration schemes [39, 29], more sophisticated target designs [40, 18] (c.f. chapter 4) as well as by ongoing laser development.

Equally indispensable for the development of devices suitable for radiobiological studies and medical applications is the competitiveness of the laser-plasma accelerator with conventional sources in terms of precision, reliability and reproducibility. Research in this field can adequately be performed with available technology and, in particular, presently accessible particle energies. The challenge is the development of a laser-based treatment facility taking into account the specific properties of LDPR, such as pulse dose and pulse dose rate, which are higher than those provided by conventional techniques by orders of magnitude, and the demonstration of its potential for clinical application. This task is addressed by a translational research process, meaning the transfer of the results of the complex and interdisciplinary basic research area into clinical practice [41], starting from *in vitro* cell irradiation, over experiments with animals, to clinical studies. Vice versa the realization of a translational step represents a benchmark of the development status of the laser-driven dose delivery system itself.

Starting with cell irradiation experiments the relative biological effectiveness (RBE) of such laser-driven proton beams has to be determined. In general, the RBE is given by

the fraction of the dose delivered by a reference radiation (here conventionally accelerated protons) to the dose delivered by the given radiation (laser-driven protons) when yielding the same biological effect, whereas the general basis of RBE measurements is the determination of dose-effect curves for *in vitro* cell systems. To obtain a radio-biologically substantial result, several tumor and normal tissue cell lines as well as different biological endpoints have to be investigated. Although it is unlikely, in the therapeutically relevant dose range of a few Gy non-linear radiobiological effects may arise for pulsed proton beams due to multiple damages in the cell within one pulse and thus below the time-scale of repair mechanisms. Complementary to studies with conventional beams [42] several groups put effort into *in vitro* investigations of such possible non-linear RBE effects due to the extreme pulse dose [43, 44, 45] using single shot exposure of a few Gy per pulse from laser-plasma accelerators. However, in those articles the proton dose applied to the cells was only analyzed retrospectively which does not allow for a controlled delivery with prescribed dose values as recommended for animal irradiation and mandatory for patients.

In order to illustrate the technical challenge for the conducting of radiobiological *in vitro* experiments on a laser-accelerator-driven cell irradiation site, the next paragraph summarizes the most relevant requirements [46]. Meeting all that requirements and in particular reaching the order of the clinical precision standard, the first direct, and dose controlled comparison of the radiobiological effectiveness of LDPR and conventionally accelerated protons *in vitro* in a full scale systematic cell irradiation campaign was realized within the frame of this thesis and will be presented in this chapter [46, 47].

### Requirements for radiobiological *in vitro* experiments

- As living cells have to be irradiated in air, a vacuum exit window for the proton beam is mandatory.
- Due to the comparatively low energy of presently available laser-accelerated protons ( $\sim 10$  MeV) all components used in transmission in front of the cell monolayer have to be as thin as possible in order to minimize energy loss.
- All types of background radiation causing cell damage such as X-rays or electrons have to be suppressed, eg., by blocking the direct view from the laser target to the cell sample or by magnetic filtering.
- The delivered proton intensity should be high enough to guarantee irradiation times of the order of few minutes to avoid the influence of any effects not related to the irradiation.
- In order to derive the biological effectiveness of laser-accelerated proton beams dose-effect-curves with radiation doses in the range of about 0.1 to 10 Gy have to be measured.

- The large shot-to-shot intensity fluctuations up to now observed for laser-accelerated proton beams as compared to conventional sources makes the delivery of a prescribed dose by a single pulse impossible. It requires the application of several pulses in combination with online dose monitoring for each individual irradiation.
- The beam diameter has to be optimized with regard to the geometry of the cell sample. This implies a homogeneous dose distribution over an area typically in the range of about 1 to 25 cm<sup>2</sup>.
- The precise evaluation of the absolute dose delivered by polyenergetic proton beams requires the knowledge of the proton energy spectrum.
- In contrast to monoenergetic proton beams common in medical applications, no absolute dosimetry protocol exists for the laser-accelerated proton pulses at low energies and therefore has to be established.
- Precise absolute dosimetry is nearly impossible when protons are fully stopped in the cell monolayer. As a practical consequence, low energy protons (below  $\sim 5$  MeV in front of the irradiation system) have to be filtered out.
- Because of the biological heterogeneity and dose dependence of radiobiological effects numerous cell samples and several independent replications of the experiments have to be performed.
- Supplementary cell samples (controls) have to be prepared but not irradiated for the determination of the impact of ambient conditions and the whole experimental procedure on the cells and on the examined biological effect.
- A cell laboratory next to the laser facility is necessary for cell culturing, sample preparation and analysis of the biological effect after irradiation. In parallel to the laser experiment, reference irradiations are required for the classification of the obtained biological results and for the comparison with other laboratories.

**Scientific environment and role of medical application project within the thesis** The application of laser-accelerated proton pulses for cancer therapy has been heavily promoted by the laser-plasma community as the ideal application matching the needs for compact and affordable technology in clinical application. Several national and international activities, often combining the expertise of laser-plasma physics, accelerator physics, radio-biology, and medicine, have been started over the last years to explore the potential of this approach. The most important projects are: Japan (PMRC – Photo Medical Research Center, Kansai), Great Britain (LIBRA – Laser Induced Beams of Radiation and their Application, Birmingham/Glasgow/Belfast etc.), France (SAPHIR – Source Accélérée de Protons par laser de Haute Intensité pour la Radiologie, Paris/Marseille/Orsay etc.), Italy

(PROMETHEUS – PROtons, ions and coherent X-rays facility based on high power laser for MEDical research, oncological THERapy, bio-imaging and radio-biology USEs, Bologna etc.) and two projects in Germany, the Munich centre for Advanced Photonics (MAP) and onCOOPTics in Dresden where this thesis is partly embedded in. The onCOOPTics project (Zentren für Innovationskompetenz-Verbundprojekt: „onCOOPTics - Hochintensitätslaser für die Radioonkologie“) aims for the development of laser-driven particle beams for radiation therapy and is supported by the German Federal Ministry of Education and Research (BMBF). It consists of three partners in Dresden (Germany), the ZIK (Zentrum für Innovationskompetenz) OncoRay and the ZIK ultra optics as well as the HZDR. This collaboration ensures that laser-driven radio-oncology as a novel concept of radiotherapy is integrated in a much broader program including molecular targeting, radiobiology, image-guided therapy, *in vivo* dosimetry and basic laser development.

In 2008, Amplitude Technologies delivered a 150 TW Ti:Sapphire based laser system, named Draco (Dresden laser acceleration source), that was installed in new clean room laboratories inside the ELBE accelerator building at the HZDR. This close proximity to accelerator infrastructure has many advantages, such as radiation shielding. Furthermore it allows for combined experiments of the ELBE electron beam and the high power laser such as Thomson scattering experiments, that were conducted in parallel to ion acceleration experiments in the last years. The ELBE building hosts a cell laboratory and an X-ray reference irradiation site, that are indispensable for all kind of radio-biological studies.

Beginning with an empty laboratory, the first central task within the frame of this thesis was the development of the setup for the generation of a reliable laser-driven proton source at the Draco laser system as described in this chapter. To some extent, that also included the establishment and the operation of the laser infrastructure and the implementation of additional laser diagnostics. Reproducible laser parameters on target, such as laser energy, pulse duration, focal spot size and temporal contrast as well as the identification of optimal target properties, precise target alignment but also development, characterization and implementation of appropriate proton beam diagnostics were the most important issues to be solved for the generation of a reliable laser-driven proton beam [19].

The next sections will focus on the setup of the Draco laser including the laser diagnostics and the concept of the proton acceleration system. To illustrate the achieved performance of the laser-driven proton beam, the results of the successful cell irradiation campaign demonstrating stable system operation for many weeks of beam-time as published in Ref. [46, 47] are presented at the end of this chapter. This work was conducted in close collaboration with the onCOOPTics team that focused in particular on the dosimetric and radiobiological methods and analysis [48, 49, 50] whereas this thesis concentrated on operation and design of the laser-driven proton acceleration experiment. In addition, there was a strong overlap for the development of particle detectors and dosimeters in particular for the investigation of saturation effects of several detector devices using the high bunch charge electron pulses

from the tunable ELBE accelerator source [51, 52, 53, 54].

## 2.1. The Draco laser system

The Draco laser is a Pulsar 200 system developed by Amplitude Technologies. It is based on the chirped pulse amplification (CPA) scheme introduced by Strickland and Mourou [1] and exhibits Ti:Sapphire crystals as primary gain medium pumped with frequency doubled, flash lamp pumped Nd:YAG laser modules. The laser system was designed to deliver ultra-short pulses of about 25 fs duration with a pulse energy up to 4–5 J on target (see Tab. 2.1). Special measures were taken to optimize the temporal contrast of the laser pulse and the implementation of actively controlled components for shaping the pulse spectrum and spectral phase enables an optimal pulse compression. A schematic drawing of the complete laser chain including the major laser diagnostic parts and a picture of the focusing performance inside the target chamber for ion acceleration is presented in Fig. 2.2.

The laser pulse is generated in a Ti:Sapphire oscillator, manufactured by Femtolasers. When mode-locked, the oscillator delivers pulses at 78 MHz with an average power of 560–600 mW. The central wavelength is 800 nm and the bandwidth amounts to about 95 nm (FWHM). At the oscillator output a 10 Hz pulse train (seed pulses) is separated using a pockels cell and transferred into a booster amplifier module comprising a saturable absorber (SA) as passive intensity dependent filter for temporal contrast enhancement of the oscillator pulses. In the booster the seed pulse is amplified by a high gain multipass amplifier up to the microjoule level. Passing through the SA cleans the pulse from amplified spontaneous emission (ASE) background generated in the oscillator. Due to the linear dispersion, the laser pulse encounters during propagation through all transmission components of the booster amplifier, the pulse duration at the SA amounts already to about 4 ps. Consequently, residual ASE components beneath the dispersed temporal pulse envelope cannot be removed by the intensity dependent filter and remain as pulse pedestals after compression (c.f. the discussion of temporal contrast measurements below).

Having left the booster amplifier, the seed pulses enter the CPA stage, beginning with the pulse stretcher, where the pulses are temporally stretched to about half a nanosecond duration. The stretcher design is based on an all-reflective Öffner triplet combination, avoiding on-axis coma and chromatic aberration. Only spherical aberration and astigmatism may appear. After amplification the pulses are re-compressed to short duration using a classical two-grating compressor design optimized for high transmission efficiency (65% compared to the energy level directly behind the last amplifier) and adaption to the stretcher ensures flattest spectral phase dispersion in the overall system.

The stretched seed pulses are coupled into the cavity of a regenerative amplifier (RA), where the pulse energy is increased up to the millijoule level. The resonator defines a TEM<sub>00</sub> transverse mode, and thus ensures an excellent beam profile propagating into the following multipass amplifiers. Together with two acousto-optic programmable gain control filters

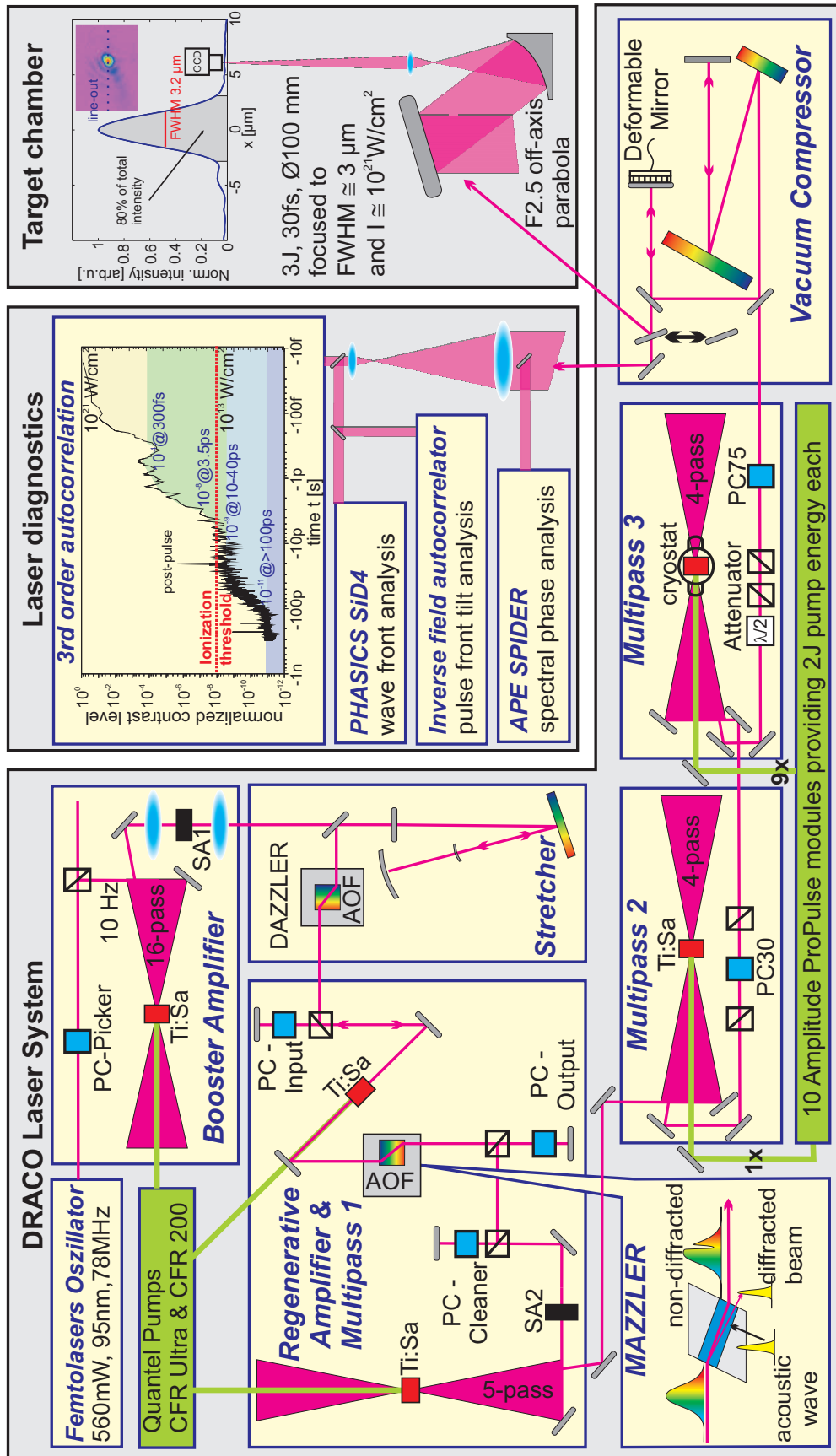


Fig. 2.2.: Illustration of the Draco laser chain, including laser diagnostics and target chamber.



parameters	$E_L$ [J]	$\tau$ [fs]	Strehl ratio	intensity [W/cm <sup>2</sup> ]	prepulse contrast	ps contrast
design	4	23-30	0.3	$> 10^{21}$	$< 10^{-7}$	$10^{-10}$
experiment	2-3	30	$> 0.9$	$\approx 10^{21}$	$< 10^{-10}$	$10^{-11}$ at 100 ps

**Tab. 2.1.:** Comparison of the design parameters of the 150 TW Draco system and those reproducibly achieved and used for the experiments discussed in this thesis. The improvement of the experimental parameters was achieved by adding further components to the original laser setup, such as a deformable mirror (better Strehl ratio), a fast pockels cell (PC30) to suppress prepulses and a second saturable absorber to reduce the ASE pedestal leaking out of the RA. All parameters refer to conditions on target. The intensity is derived using a focal spot diameter (FWHM) of  $3\ \mu\text{m}$ . Contrast is given as the power ratio with reference to the maximum pulse power as discussed below. The ps-contrast level refers to the ASE pedestal a few hundreds of picoseconds prior to the main pulse (see main text for detailed discussion).

(AOF), one intra-cavity (MAZZLER) and another one directly ahead of the RA entrance (DAZZLER, both from Fastlite) the RA represents the core of the laser system.

One main limitation for laser amplification is the spectral gain narrowing in the amplifier chain which reduces the temporal compressibility of the pulse (due to Fourier Transform properties). With the MAZZLER this effect is pre-compensated by actively introducing spectral losses into the RA cavity using an acoustic wave that diffracts unwanted spectral components out of the resonator as depicted bottom left in Fig. 2.2. This ensures a spectrally constant amplifier gain of the non-diffracted cavity beam and enlarges the global amplification bandwidth from initially 30 nm to up to 80 nm, thus enabling pulse durations of below 25 fs after compression. The shape of the filtering acoustic wave is calculated on the basis of pulse spectra measured behind the multipass 1 stage and optimized iteratively. The gain narrowing in the two last multipass amplifiers is small due to their moderate overall gain.

Similarly, the DAZZLER is used to independently control the spectral phase of the pulse. In combination with a spectral phase measurement of the compressed pulse using a SPIDER (spectral phase interferometer for direct electric-field reconstruction) by APE, that is situated at the end of the laser chain, higher order dispersion effects in the laser system are pre-compensated by a computer controlled loop resulting in spectral phase modulations of less than  $\pm\pi/3$  over the whole spectrum.

When amplification saturation is reached the seed pulse is extracted from the RA cavity by switching the output pockels cell (PC-Output). In order to optimize the contrast ratio between output pulse and the other round trips (separated by 12 ns), the leakage pulses are additionally suppressed by means of a pulse cleaning pockels cell (PC-Cleaner) right behind the RA and another one behind multipass 2 (PC30 with 4 ns rise-time). The ASE background generated in the RA cavity is removed by a second saturable absorber installed on the transfer path to the next amplifier.

Further amplification of the pulse energy up to 6 J at a pulse repetition rate of 10 Hz is realized by 3 stages of multipass amplifiers. The seed pulse is freely propagating and its size

is continuously enlarged by a series of Galilean type telescopes up to the final beam diameter of about 10 cm in front of the compressor chamber.

The first multipass amplifier crystal is pumped with an energy of 120 mJ (at 532 nm) from a single frequency doubled YAG laser (CFR 200 from Quantel). The second multipass amplifier is pumped with 1.8 J delivered by one Propulse+ Nd:YAG laser and the third amplifier crystal (5 cm edge length and 3 cm thick) can be pumped with up to 18 J from 9 ProPulse+ lasers manufactured by Amplitude Technologies. Cryogenic cooling in the last amplifier yields a significant increase of the thermal conductivity of the crystal and therefore ensures a stable beam profile and reduced wave front distortion for variable pumping power and thus variable beam energy.

Behind multipass number 2 and 3 large aperture pockels cells PC30 and PC75 have been installed to protect the system against high energy back reflections from the laser plasma interaction, which can be additionally amplified in the amplifier crystals that are still pumped. Using these pockels cells and an additional attenuator, consisting of a large aperture half wave plate and a pair of thin film polarizers behind the multipass 3 the beam energy can be continuously attenuated by about 4 orders of magnitude without insertion of additional components to provide appropriate and flexible diagnostic beams with optically identical properties.

After pulse compression in vacuum (vacuum compressor chamber), in order to avoid non-linear intensity effects such as self-phase modulation or beam filamentation due to self-focusing in air, the beam is either delivered to the laser diagnostic table (attenuated to a few percent) or it is transported into the dedicated target chamber.

**Laser diagnostics** In order to provide identical dispersion conditions between inside the target chamber and on the diagnostic table for the analysis of the spectral phase with the SPIDER diagnostic a small part of the collimated beam is picked immediately behind the compressor exit window. Afterwards, the beam size is reduced for further diagnostics using a large aperture telescope (see Fig. 2.2). As mentioned above, the SPIDER measurement is used to pre-compensate for phase distortions with the DAZZLER and thus to optimize and measure the laser pulse duration. Potential pulse-front tilts are interferometrically monitored using an inverse field autocorrelator [55] and minimized over the full aperture. Wavefront corrections are performed with a large aperture deformable mirror installed inside the compressor chamber. For the closed loop correction, performed on a daily basis, the surface of the mirror is imaged onto a wavefront sensor (SiD4 manufactured by Phasics).

Inside the target chamber the wavefront corrected beam of about 90-100 mm diameter is tightly focused using an off-axis parabolic mirror with a focal length of 250 mm (23° off-axis angle) to a spot size of about 3  $\mu\text{m}$  diameter (FWHM). This is illustrated by the enlarged image of the focal spot (insert top right Fig. 2.2, linear rainbow colour scale) measured inside the target chamber with an aberration corrected large distance microscope lens. Latter is mounted on large travel range motorized stages in order to move it out of the beam and

thus to provide a permanent installation as a reference. The horizontal line-out (top right Fig. 2.2) shows that 80% of the laser energy can be concentrated inside the focal spot. Consequently, peak intensities of up to  $10^{21}$  W/cm<sup>2</sup> can be achieved on target. The pointing stability yields a focus fluctuation less than the focal spot size.

As mentioned above in the design of the laser system special measures were taken to optimize the temporal pulse contrast. By means of two saturable absorbers, one cleaning the short energy boosted oscillator pulse at a pulse duration of a few picoseconds and a second, installed behind the regenerative amplifier, the ASE background from both cavities is significantly suppressed. A representative contrast curve normalized to the main pulse intensity at  $t = 0$  is depicted at the top of Fig. 2.2. Note, that the experimental data between 10 and 100 fs is resolution limited due to the measurement technique (temporal dispersion in doubling crystals). For the same range the SPIDER measurement yields a pulse duration of 30 fs. The autocorrelator trace shows that a pulse contrast ratio level of few  $10^{-11}$  can be achieved over several 100 ps before the intensity starts to increase about  $t = -100$  ps ahead of the main pulse up to a level of about  $10^{-9}$  (this level may fluctuate on a daily basis). The ionization threshold intensity of  $(10^{12} - 10^{13})$ W/cm<sup>2</sup> is exceeded at  $t = -3$  ps for the first time. On the nanosecond time-scale the ASE pedestal as well as prepulses leaking out of the regenerative amplifier or originating from cross-talk in the multipass amplifiers are verified with a fast photodiode (rise-time of 200 ps) using calibrated absorption filters and a fast oscilloscope. The ASE signal begins to become measurable about 4 ns before the main pulse and reaches an energy contrast, which integrated over 100 fs (time resolution of the third order autocorrelator) is consistent with the intensity contrast measurement for few 100 ps. Potential ns-prepulses from the RA and the first two multipass amplifiers were ruled out with a dynamic range of better than ten orders of magnitude by shifting the time delay window of PC30 prior to the main pulse and thus using it as an additional time dependent attenuator for the main pulse.

The parameters, which have routinely been achieved on target for experiments are listed in Tab. 2.1 and compared with the design parameters of the system. Besides the establishment of appropriate alignment protocols, the improvement of the experiment parameters was mainly achieved by adding further components to the original laser setup. The deformable mirror enabled the optimization of the focal spot (Strehl ratio), the fast pockels cell (PC30) suppressed the prepulses and the second saturable absorber was successfully implemented to reduce the ASE pedestal leaking out of the RA.

## 2.2. Setup of the laser proton source for cell irradiation studies

In parallel to the implementation of the Draco laser system, next-door an experimental area was installed and equipped with a vacuum chamber (footprint of  $112 \times 219$  cm<sup>2</sup>) dedicated to

the generation of laser-driven ion and proton radiation. The infrastructure for the transport of the laser beam to the target area as well as an off-axis parabolic mirror for beam focusing had to be set up. Appropriate diagnostics for focal spot optimization and target alignment as well as for the characterization and optimization of the generated proton beam was developed and will be presented in the following. Special care was taken to use components that in principle are compatible to a laser operation of 10 Hz.

Applying this setup to conduct first proton acceleration experiments in the TNSA regime using flat metal foils as target, yielded proton energies of up to 17 MeV, at that time unprecedented for high intensity laser pulses of 30 fs duration [19]. This surprising and at the same time very promising result represented the fundament for the radiobiological studies described in this chapter and published in Ref. [46, 47, 49, 56].

Furthermore, the same experimental setup and diagnostic components were used to investigate the underlying physical mechanisms of the proton acceleration process and their potential correlations with laser parameters and target properties as will be addressed in the chapters 3 and 4 of this thesis. For that a reference laser-target configuration was established and characterized for a period of several months (Sec. 2.2.2). It was directly applied for the cell irradiation experiments presented below and later used to optimize and determine the proton beam performance on a daily basis in order to relate the data obtained in all the physics experiments within the frame of this thesis.

### 2.2.1. Proton beam generation

The experimental setup as sketched in Fig. 2.3 has to meet the requirements for both, the laser beam transport and focusing with large aperture optics in vacuum (see Sec. 2.1) and the generation as well as the detection of the proton beam with its peculiar properties calling for a system of multiple and complementary detectors.

Intense proton pulses generated with an ultra-short pulse laser as Draco in the TNSA regime exhibit a high number of protons of about  $10^{12}$  protons per pulse, typically distributed according to an exponentially decaying energy spectrum (few keV to few 10 MeV) as explained in Sec. 3.1. Initially, the proton pulse is generated within a few hundreds of femtoseconds but during propagation to the detector the non-relativistic proton bunch is significantly broadened by the difference in time-of-flight of the individual particles to up to a few nanoseconds. As the name target-normal sheath acceleration (TNSA) already implies, the proton beam is predominantly emitted in target normal direction. The divergence angle amounts to about  $\pm 20^\circ$  but decreases with increasing proton energy. Furthermore, the laser-plasma interaction causes an important amount of background radiation, such as high energetic electron radiation but also secondary X-ray radiation that has to be taken into consideration for the detector design.

As sketched in Fig. 2.3(a), targets were routinely irradiated with p-polarized light at an incident angle of  $\delta = 45^\circ$ . Different angles of incidence can be achieved by simple rotation

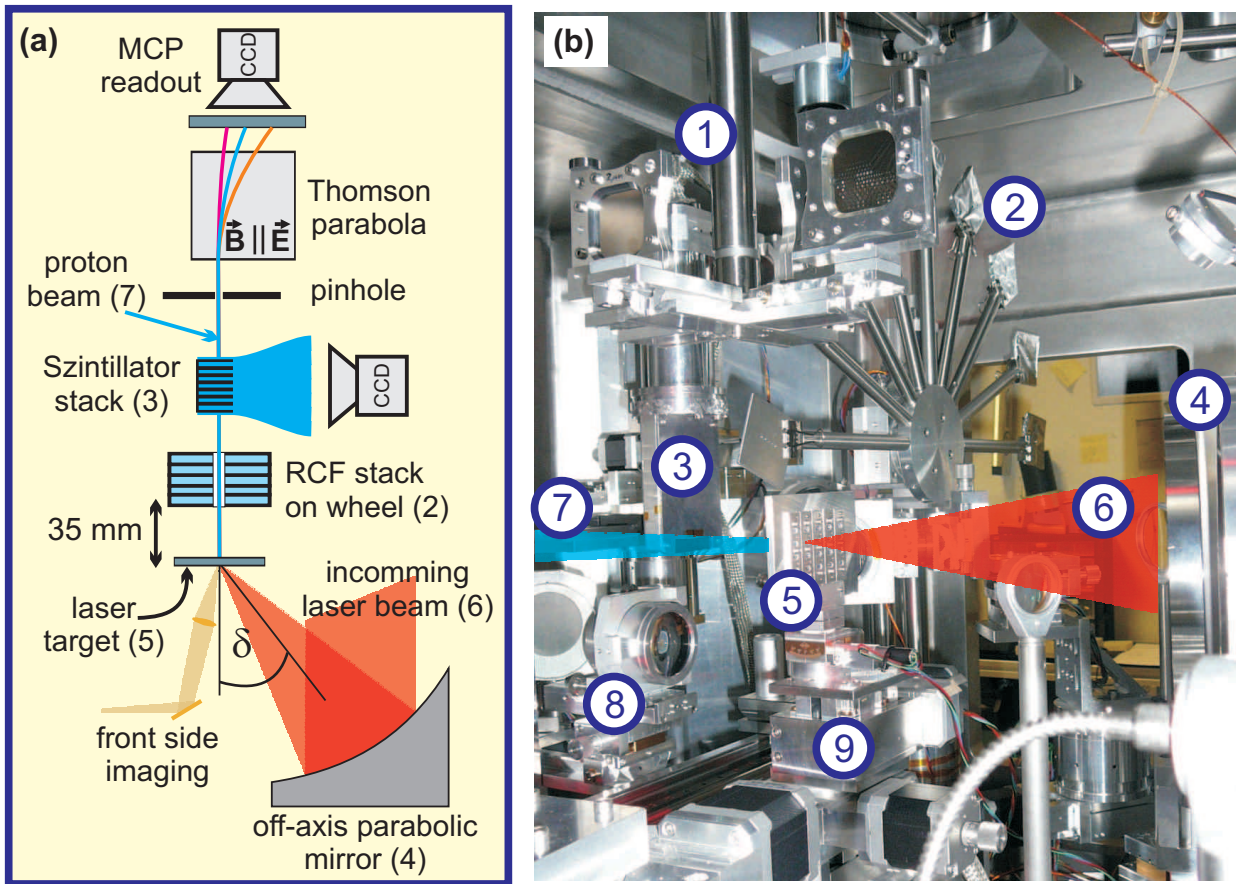
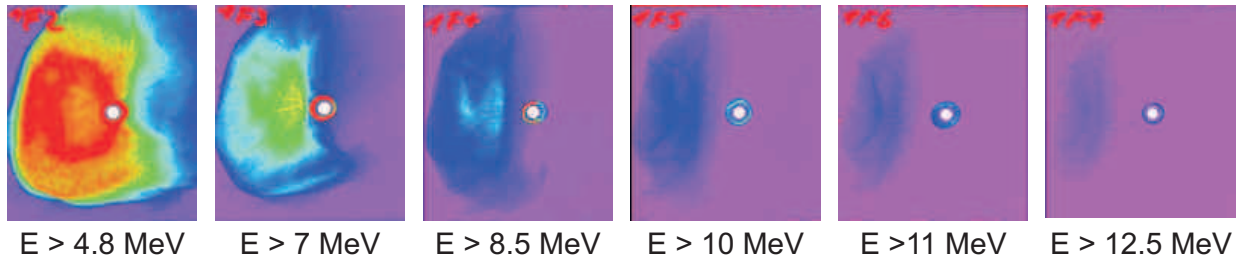


**Fig. 2.3.:** (a) Schematic overview of the experimental setup and the proton diagnostics used in the present experiments.  $\delta$  denotes the incident angle of the laser with respect to the target-normal direction. The complete proton beam is detected with RCF stacks positioned at about 35 mm behind the target and, through a hole in the center of the RCF stack, the proton spectrum is measured with a Thomson parabola spectrometer for a small solid angle in the target-normal direction. Additionally, a stack of plastic scintillator read-out with a CCD can be used to measure the angular proton emission distribution along the horizontal plane (more details in Ref. [57]). (b) For illustration of the real design a photograph shows the inside view of the target chamber for a setup of normal incidence of the laser beam  $\delta = 0$  (see chapter 3). Indicated components are as follows 1: target exchange device, 2: RCF wheel, 3: scintillator stack detector, 4: off-axis parabola, 5: target, 6: incoming laser beam, 7: proton beam propagating to the Thomson parabola entrance, 8: focus diagnostic, 9: target manipulation stages.

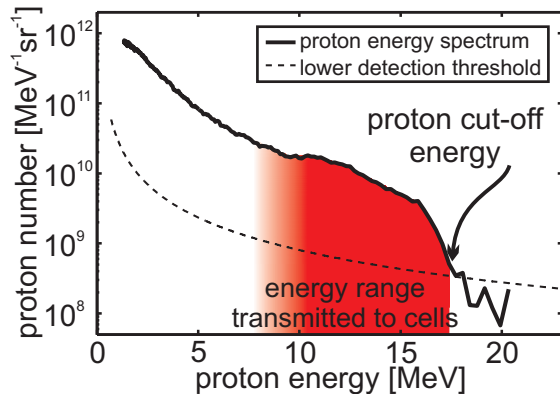
of the target to keep the alignment of the incoming laser constant. For this the detectors have to be moved accordingly that in principle does not cause any problem as the vacuum chamber is big enough and therefore very flexible. The considerable amount of light reflected back into the system at small angles of incidence  $\delta \gtrsim 0^\circ$  is completely suppressed by use of additional pockels cells in the laser system (see Fig. 2.2) in order to protect the system from severe damage.

For most experiments presented in this thesis thin metal foil targets predominantly made of titanium or gold were used. To ensure really tightened target surfaces, necessary for an exact definition of the target-normal direction, the foils together with their target mounts

## (a) Typical RCF stack sample



## (b) Thomson parabola trace



## (c) Sample image of stacked scintillator detector

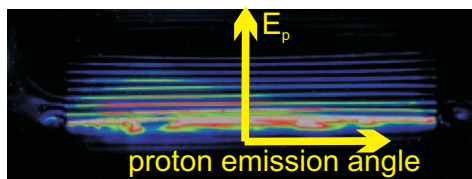


**Fig. 2.4.:** Representative proton detector output (c.f. Fig. 2.3) using  $2 \mu\text{m}$  thick flat titanium foil as target and a laser energy of  $3 \text{ J}$ ,  $30 \text{ fs}$  pulse duration,  $p$ -polarization and oblique laser incidence (see also next section). (a) An RCF stack sample trace is displayed as a false color image. (b) A proton energy spectrum with a cut-off energy of  $17 \text{ MeV}$  recorded with the Thomson parabola spectrometer is shown. (c) A sample image recorded with the stacked-scintillator detector is depicted. The colored lines correspond to the angular proton emission distribution projected on the horizontal beam axis. The different scintillator layers providing a coarse energy resolution.

(generally made of aluminum) were cooled down in a freezer or in liquid nitrogen and screwed together afterwards. By warming up the foil gets tightened due to the different coefficient of thermal expansion of the materials.

The mount of the target as well as all important mounts of optical components are motorized to ensure sufficient reproducibility of the setup. This is especially important for the alignment of complex setups to remain stable for the complete campaign. A special target foil exchange device allows about 1000 shots without breaking the vacuum (see photo in Fig. 2.3).

Positioning in the focal plane is continuously monitored between consecutive laser shots by backside imaging as well as front side imaging of the focal spot of an alignment laser beam exactly co-propagating with the high power beam. This results in an alignment precision for the focus depth of  $\pm 10 \mu\text{m}$  that is sufficiently exact to maintain a stable proton beam performance beginning to decrease with a shift from the best focal position by about  $\pm 20 \mu\text{m}$  [57].

The angular resolved energy distribution of the proton pulses accelerated from the target rear side under target-normal direction are detected using stacks of radiochromic films

(RCF). The stacks consist of one GafChromic HD layer followed by several GafChromic EBT layers, covered with  $13\ \mu\text{m}$  Al foil and mounted 35 mm (if not stated differently) behind the target. The RCF stacks are mounted on a motorized wheel in order to irradiate up to 14 stacks before opening of the target chamber becomes necessary. The used EBT films are absolutely dose calibrated [49, 48]. The stacking of many RCF slices provides a coarse energy resolution due to the range-energy relationship of the stopping power. From the RCF data the proton spectrum can be reconstructed and since the complete proton beam can be recorded, a calculation of the conversion efficiency of laser to total proton energy is possible [58]. A typical value of the conversion efficiency measured at Draco is about 0.5% (considering only protons with an energy exceeding 4 MeV, [19]). An RCF stack sample trace is displayed as a false color image in Fig. 2.4(a) illustrating the proton beam profile, decreasing in size with increasing proton energy. The hole in the RCF layers, visible as white circles corresponds to the target-normal direction and enables further proton beam analysis behind the stack. The RCF stack sample shows a deflection of the most energetic protons, of a few degree from target-normal into the direction of the initial laser propagation axis. This robust signature is linked to the acceleration mechanism and will be discussed in detail in chapter 3.

As an RCF stack is an offline detector meaning vacuum has to be broken for the analysis, an online detection of the angular proton distribution along one spatial dimension can be used that is based on a stack of 0.2 mm thick plastic scintillating screens, each of them covered with a light-tight foil. The upper side surface of the stack is imaged to a camera (see sample image in Fig. 2.4(c)) providing an energy selective projection of the angular distribution for each individual layer. Design and characterization of this novel detector system is treated in Ref. [57].

To detect proton spectra with higher spectral resolution and to distinguish different ion species a Thomson parabola spectrometer consisting of parallel magnetic (560 mT) and electric fields ( $3.7 \cdot 10^5$  V/m) is used. The parabolic ion traces are recorded using a multi-channel plate (MCP) with phosphor anode imaged to a 12 bit CCD camera in order to provide online analysis of the obtained ion spectra in the energy range of 1-30 MeV (details are given in Ref. [59]). A sample spectrum recorded with the spectrometer for a well performing shot onto a  $2\ \mu\text{m}$  titanium foil target is depicted in Fig. 2.4(b). As expected for the TNSA process it shows an exponential proton spectrum, here with a cut-off energy of 17 MeV.

For the detection of electrons co-propagating with the analyzed proton beam, the Thomson parabola possesses a second MCP with CCD read-out that allows to record electron traces in the energy range of 10 keV to 20 MeV [60]. The separation of electrons, protons and ions can also be realized by the different time-of-flight of the particles. A dedicated time-of-flight detector based on an MCP exhibiting a fast signal rise time of less 200 ps was developed [59] and can be used complementary to the Thomson parabola for a small solid angle.

## 2.2.2. Long-term performance of the laser-driven proton beam

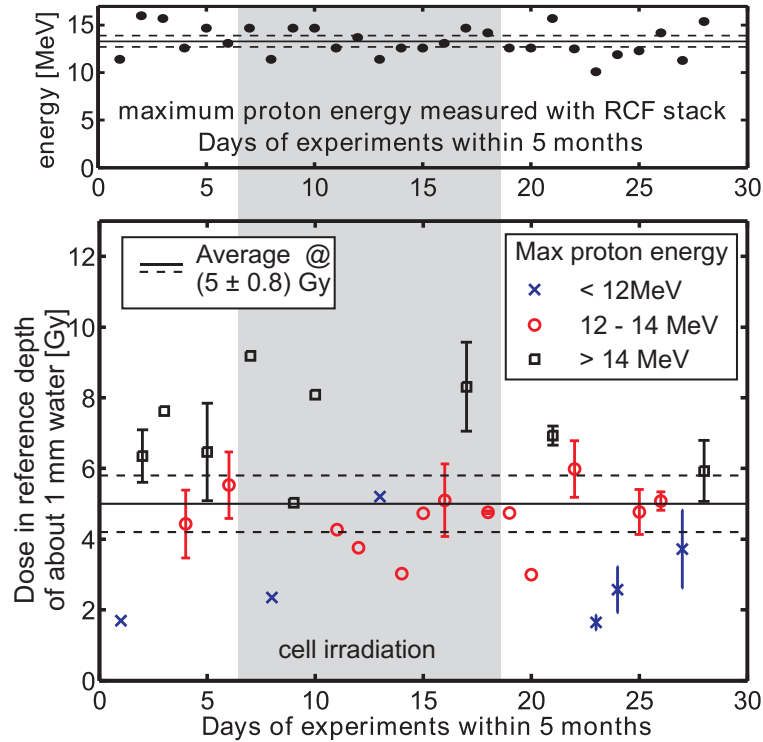


**Fig. 2.5.:** *Stability of the laser-proton radiation source. The reference pulse dose was evaluated for 28 days within 5 months, including the cell irradiation experiment marked in grey. As the relevant parameter of the exponential spectrum the dose in a reference depth of about one millimeter water (this range requires an initial proton energy  $> 10$  MeV) is plotted (bottom), where all reference data collected on one experiment day is averaged. Additionally, the characteristic proton cut-off energy ( $E_{\max}$ ) is coded into the colour of the data points. Its correlation with the dose is expected for an exponential energy spectrum. For better illustration, the maximum proton energy of each reference shot is plotted separately again and shown on the top.*

In order to compare the performance of different experiment days within one experimental campaign as well as from other campaigns, a dedicated robust reference laser-target configuration was defined. Reliably reproducible laser parameters namely a pulse energy of about 2.3 J on target and a pulse duration of 30 fs (FWHM) are applied. The contrast conditions and focusing (about 3  $\mu\text{m}$  FWHM focal spot diameter) are maintained as discussed in the previous section. The laser pulse illuminates a 2  $\mu\text{m}$  thick titanium foil at  $\delta = 45^\circ$  incidence and p-polarization. By using the Thomson parabola the daily proton beam performance, here the cut-off energy of the exponential spectrum is optimized and fluctuations during operation can be tracked. Afterwards, dose and spectrum of reference pulses are measured with an RCF stack recording the complete proton energy distribution for single reference shots (Fig. 2.5). The pulse dose measured on the fifth film layer, corresponding to a reference depth of about one millimeter in water, and the characteristic cut-off value of the exponential proton energy spectrum ( $E_{\max}$ ) as depicted in Fig. 2.5, were used to characterize the proton beam. The overall average pulse dose of  $(5 \pm 0.8)$  Gy and the overall average



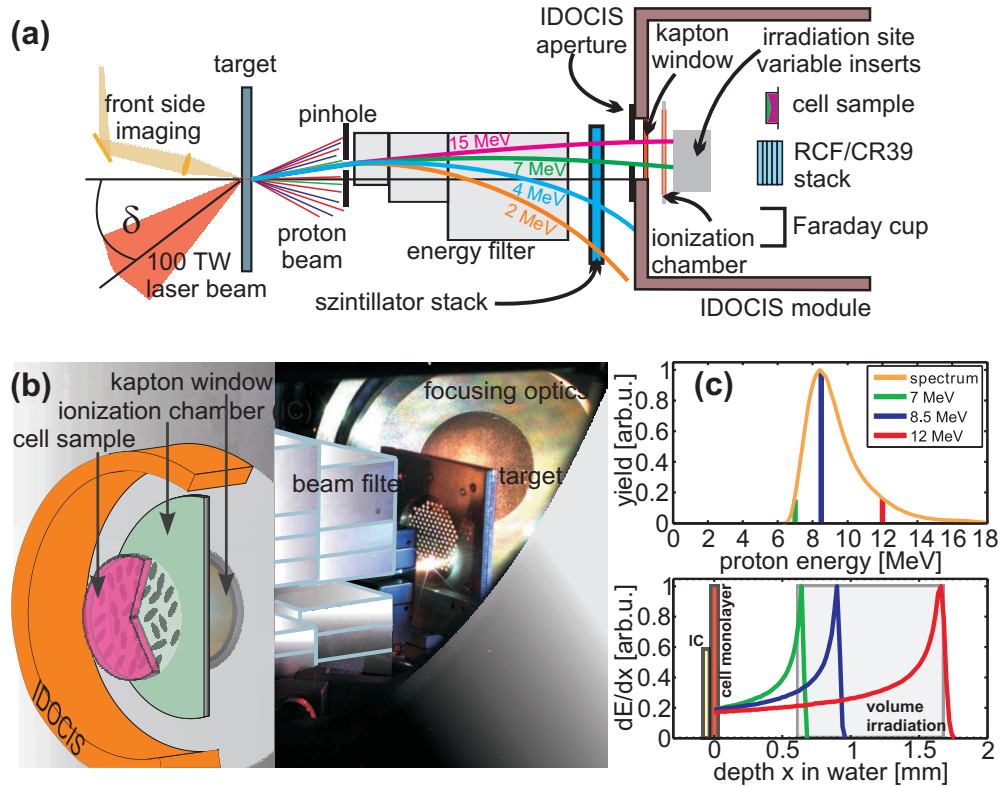


**Fig. 2.6.:** (a) Schematic overview of the experimental setup, the laser-proton acceleration, the proton energy filter and the air-filled integrated dosimetry and cell irradiation system (IDOCIS). Between the energy filter and the IDOCIS entrance aperture the stacked scintillator can be introduced to monitor the transmitted proton spectrum [56]. (b) For further illustration a picture showing the experimental irradiation setup for the generation of LDPR at the instant of a single laser shot is presented on the right. The laser pulse is focused by the off-axis parabolic mirror in the background onto the thin target foil, where protons are accelerated in the generated plasma flash and then propagate towards the IDOCIS module. (c) The normalized proton energy spectrum at the cell location is shown. For the representative energies 7, 8.5 and 12 MeV the normalized energy deposition as function of the depth in water is depicted. As illustrated, the cell monolayer is irradiated in the plateau of the corresponding Bragg curves. Contrarily, volumetric irradiation will be performed in the range of the Bragg peaks.

maximum proton energy ( $13.3 \pm 0.6$ ) MeV confirm reproducible system performance at the level required for radiobiological experiments over a period of five months.

### 2.2.3. Cell irradiation setup

For the *in vitro* cell irradiation study carried out at the Draco laser the experimental setup (c.f. Fig. 2.3) was modified as sketched in Fig. 2.6. In a short distance of 2 cm behind the target the energetic protons pass a magnetic dipole filter [56] applied to clean the pulse of all protons with energies below 8 MeV as it is illustrated by the red shaded area in the sample spectrum of Fig. 2.4(b). The energy filter consists of three dipole magnet segments providing high magnetic field strength between 0.8 and 1 T with increasing gap size to account for the beam divergence in the non-dispersive plane and a squared entrance pinhole of  $2 \times 2 \text{ mm}^2$ .

The segmentation of the dipole magnet structure allows to reduce the iron yoke sizes so that the dipole filter can be positioned close to the proton source at a distance of only 18.5 mm maximizing the acceptance angle of the filter.

The configuration and the positioning of the filter system was optimized for the measured angular emission distribution (see RCF trace in Fig. 2.4(a)) that exhibits a small deflection from the target-normal into the incoming laser direction. Making use of this deflection the transport efficiency with respect to the isotropically emitted secondary radiation background was optimized as described in Ref. [56]. Furthermore, the dispersion of the magnet and the position of the aperture in front of the irradiation site shifted next to the target-normal axis (see Fig. 2.6(a)) intrinsically blocks the direct line-of-sight between the interaction point and the irradiation site and thus suppresses secondary radiation generated in the laser-plasma.

Directly following the magnetic filter the integrated dosimetry and cell irradiation system (IDOCIS) is located [49]. It was developed according to the challenges regarding the dosimetry of laser-accelerated polyenergetic proton beams. As listed in the beginning of this chapter, an online dosimetry and cell irradiation device integrating different detectors that in combination and after calibration provide absolute dose information is required. The interior components of the IDOCIS module for dosimetry and cell irradiation are separated from the vacuum of the target chamber by a thin plastic window. In addition to the inset for the cell sample, the IDOCIS module features an inset for a Faraday cup (FC, design adopted from Ref. [61]) and further insets for RCF stacks (GafChromic EBT and EBT2) and CR39 nuclear track detectors. The FC and RCF dosimetric systems were used to determine the absolute dose delivered to the cell sample. For that purpose an absolute calibration for both detectors was carried out before performing the irradiation experiments with laser-accelerated protons for proton energies of 5-60 MeV at the eye tumor therapy center at the Helmholtz Zentrum Berlin (HZB), Germany [49]. Directly behind the entrance window the IDOCIS module integrates a thin transmission ionization chamber (IC) optimized for lowest ion energies and thus consisting of 3 metalized kapton foils (each only 7.5  $\mu\text{m}$  thick). The IC is permanently placed in front of the different insets and is used to establish the relationship between FC and RCF to the real-time control of the dose delivery. It is therefore cross-calibrated to FC and RCF before and after each cell irradiation taking saturation effects due to different collection efficiencies into consideration [54].

During the irradiation dose homogenization on the sample is ensured by multiple rotation of the cell sample. The optimization and control of the homogeneous 2D dose distribution in the plane of the cell monolayer ( $2 \times 6 \text{ mm}^2$  in size) and the estimation of the contribution of the inhomogeneity (less than 5%) to the dose error was performed with RCF and CR39 nuclear track detectors. An important prerequisite for the control of the dose deposited into the thin cell monolayer is the precise knowledge of the proton energy spectrum. The normalized proton energy spectrum at the cell location is shown in Fig. 2.6(c). It was calculated on the basis of a spectrum measured with the Thomson parabola spectrometer (c.f. Fig. 2.4) before the irradiation campaign. Here, the use of sufficiently high proton

energy at cell layer position ( $>6.5$  MeV) ensured a constant linear energy transfer (LET), and therefore significantly less uncertainty than if the Bragg peak would be attempted to be positioned at the depth of the cell monolayer. This is illustrated by the normalized energy deposition as function of the depth in water for representative energies 7, 8.5 and 12 MeV depicted below the energy spectrum in Fig. 2.6(c). As illustrated, the cell monolayer is irradiated in the plateau of the corresponding Bragg curves. Additionally, stacks of RCF and CR39 were used to cross-check the applied energy spectrum in the plane of the cell monolayer.

During the irradiation experiments, the stability of the spectral filtering was monitored with the stacked scintillator detector introduced in the previous section [57] positioned between the dipole filter and the IDOCIS entrance aperture. Imaging of the upper side of the scintillator layers provides an energy selective projection of the horizontal beam profile behind the dispersive dipole filter.

### 2.3. Results of the *in vitro* cell irradiation study

Following the demonstration of the biological efficacy of LDPR in proof-of-principle experiments by others and our group [62, 46] and further investigations of possible non-linear RBE effects due to the extreme pulse dose [43, 44, 45] the presented work focuses on the demonstration of a full scale systematic cell irradiation campaign meeting all the requirements listed in the beginning of this chapter and in particular reaching the order of the clinical precision standard [47]. The successful direct and dose controlled comparison of the radiobiological effectiveness of LDPR and conventionally accelerated continuous proton beams from a tandem Van-de-Graaf accelerator shows the maturity of the developed laser-driven dose delivery system for relevant radiobiological *in vitro* studies. The presentation of the results in this section only comprises the most important details for the treatment of the cell samples and the biological endpoint. For an exact description of the methods and protocols, in particular the analysis of the obtained radiobiological results and their interpretation refer to Ref. [50].

For the presented *in vitro* irradiation experiment, the radiosensitive human squamous cell carcinoma cell line SKX was used [63]. Cells were seeded one day before irradiation on a thin biofilm as bottom of a chamber slide. Before irradiation 1 ml of cell culture medium was added, the well was closed with sterile parafilm and the sample was positioned in the horizontal LDPR beam (see Ref. [64, 65] for further details). The cells were irradiated with a mean dose of 81 mGy per shot (0.43 Gy/min) in the dose range between 0.5 and 4.3 Gy while the applied dose was controlled by means of the ionization chamber in front of the cells.

The biological effectiveness of LDPR and conventionally accelerated protons was characterized by determination of the yield of residual DNA double-strand breaks remaining 24 h

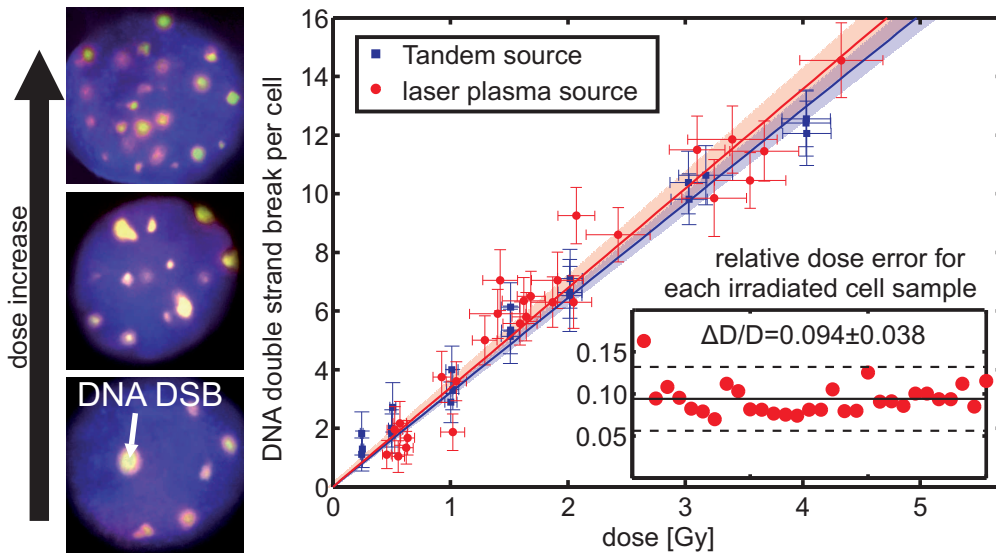


**Fig. 2.7.:** Results of cell irradiation. (Left) Fluorescence microscopy pictures (1000 fold magnification) of SKX tumor cell nuclei irradiated with different doses delivered by the laser-accelerated protons. Each formation of co-localized  $\gamma$ -H2AX plus 53BP1 foci (colored yellow-pink) indicate a DNA double strand break used to quantify radiation induced biological damage. (Right) The averaged number of DNA DSB plotted and linearly fitted as function of the applied dose for each cell sample irradiated with LDPR (red) in comparison with a continuous proton reference beam (blue). The red and blue shaded areas correspond to the confidence intervals ( $2\sigma$ ) of the fits. The inset shows the relative dose uncertainty for each sample irradiated with LDPR.

after irradiation, that has been previously shown for this cell line to correlate closely with cell survival [66]. The biological endpoint of residual DNA double-strand breaks (DSB) was analyzed by the immunofluorescence  $\gamma$ -H2AX/53BP1 staining technique [67, 68]. The average number of radiation induced DNA DSB per cell nucleus was counted for each irradiated cell sample and evaluated as a function of the applied dose. An in-house tandem Van-de-Graaf accelerator served as reference radiation source providing 7.2 MeV protons delivered as a continuous beam with a dose rate of 1.1 Gy/min in a homogeneous beam spot of 35 mm<sup>2</sup>. The equipment and the dosimetry methods, e.g. including IDOCIS module and detectors, cell vessel geometry, horizontal beam application etc., were absolutely identical for both radiation sources (c.f. [49]). As the irradiation setup was initially developed for the polychromatic beam of the laser-plasma accelerator, no additional filtering was applied in case of the mono-energetic tandem beam. For the dosimetry the spectrum has no further implications because the cell sample is positioned ahead of the Bragg Peak. Moreover, the location of both radiation sources and a cell laboratory on one site guarantees the direct comparability of radiobiological outcome for laser-driven and conventionally accelerated proton beams. In order to connect the temporally different experiment campaigns (LDPR and conventionally accelerated protons), and to identify deviations in the biological response arising from the application of variable cell sample geometries, reference irradiations with standard 200 kV X-rays (filtered with 7 mm Be and 0.5 mm Cu) were performed in parallel

to each proton experiment.

The dose effect curves of the laser-driven proton pulses (red dots) and the conventionally accelerated continuous proton beam (blue squares) are compared in Fig. 2.7. This direct comparison reveals no significant difference in the radiobiological effectiveness as indicated by the substantially overlapping confidence intervals ( $2\sigma$ ) of the almost identical linearly fitted curves. This radiobiological result is in good agreement with an experiment performed with conventionally accelerated proton beams at the Munich Tandem Van-de-Graaf accelerator [42, 69]. Making use of different pulse modes, that study focused on the dependence of the RBE on the proton pulse dose rate by comparing the effect of short-pulses (few ns) and continuous beams of 20 MeV proton energy without the need to qualify LDPR. Consistently, other groups predominantly focusing their attention on the investigation of possibly non-linear effects of the biological efficacy when using extreme high doses (up to 5 Gy) per pulse [43, 44, 45] and retrospective dose evaluation found no significant biological effects when applying ultra-short bursts of laser-driven protons with high dose rate, neither. It thus seems that all studies performed for different cell-lines and making use of different sources confirm that in the therapeutically relevant dose range of a few Gy, even if applied in a single pulse of only few nanoseconds duration, non-linear radiobiological effects due to simultaneous multiple damages in cells and thus below any time-scale of repair mechanisms are unlikely to arise.

Furthermore, as an even more important result of the experiment presented here, a similar level of the relative dose error  $\Delta D/D$  could be reached experimentally for both techniques and for each irradiated cell sample. This level remains below 10% as depicted in the inset of Fig. 2.7 and reaches the order of the clinical precision standard of 3-5%. The key to this, for laser based acceleration unprecedented level of precision is the synergetic combination of first, the reduction of the uncertainty in the dose delivery caused by beam fluctuations and detector responses using two independent absolute dose formalisms, and second, the reliable operation of the laser-driven proton source based on well-controlled laser conditions on target.

The measurement of the precise dose applied to the cell monolayer is based on the implementation of RCF and a Faraday cup into the irradiation site as two distinct, dose rate independent, and absolutely calibrated dosimetry systems, as mentioned in the previous section. Using these systems the absolute dose value and the relative dose uncertainty were determined for each irradiated cell sample individually, by repeated cross-calibration of the real-time monitor signal of the transmission ionization chamber to RCF and FC directly before and after each irradiation. Performing a weighted average of the RCF and FC signals, in combination with the use of sufficiently high proton energies at the cell monolayer position ( $>6.5$  MeV, see Fig. 2.6(c)), allowed for this significant reduction of the measurement uncertainty.

Sufficiently high shot-to-shot reproducibility measured with the IC as an online dose monitor of the proton pulses for the irradiation of single cell samples was already demonstrated

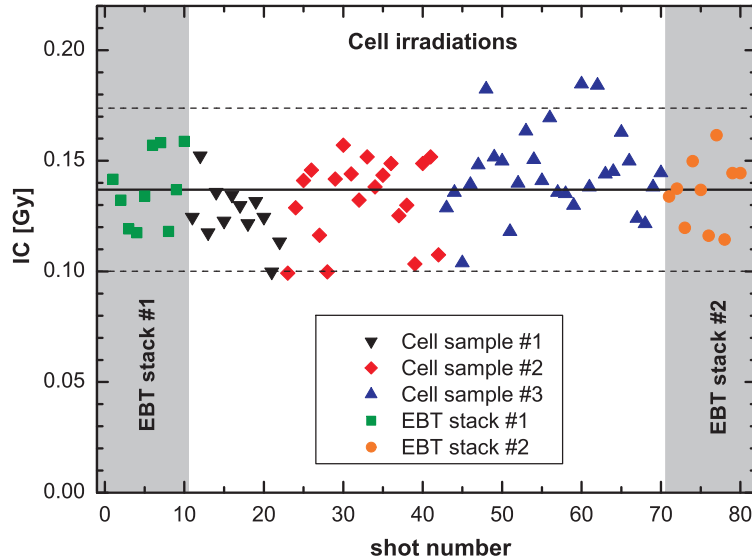


**Fig. 2.8.:** Shot-to-shot dose variations over all EBT film stack and cell irradiations measured during the proof-of-principle experiment published in Ref. [46]. The mean obtained dose rate of  $0.137$  Gy for all irradiation is shown as a black solid line, whereas the  $2\sigma$  confidence band is indicated with dashed lines.

in a first proof-of-principle [46] and is plotted in Fig. 2.8. There the mean dose per shot of  $(0.137 \pm 0.039)$  Gy during cell and EBT stack irradiation exhibits shot-to-shot variations of about  $\pm 28\%$  for a 95% confidence level. As the IC provides the online dose information for every applied pulse, the delivery of the prescribed doses to the cell samples is possible with a maximum uncertainty in units of the dose of one pulse. Further automation of the laser start-up protocol, monitoring, and the implementation of the target alignment procedure extended this stability over a total operation period of three weeks comprising several thousands of shots. Long term reliability of the proton beam generation at the level required for radiobiological experiments was confirmed by monitoring dedicated proton test pulses on 28 days out of 5 months as was already shown in Fig. 2.5.

## 2.4. Summary and future perspectives

In summary, the results of the presented experiment demonstrate for the first time that a complete dose delivery system, consisting of a laser-plasma accelerator, beam delivery, and dedicated dosimetry can meet the standards established for conventional experiments on the radiobiological effectiveness of ionizing radiation not only in proof-of-principle, but in a full scale campaign running for several weeks. As the test case, the direct comparison of the biological effectiveness of pulsed laser-accelerated protons and conventionally accelerated continuous proton beams making use of cell monolayers matching the currently available particle energies of  $\sim 10$  MeV was used. The biological effect was found to be independent from the temporal pulse structure. But the key result is that for the laser-driven proton dose delivery system a level of uncertainty reaching the order of the clinical precision standard

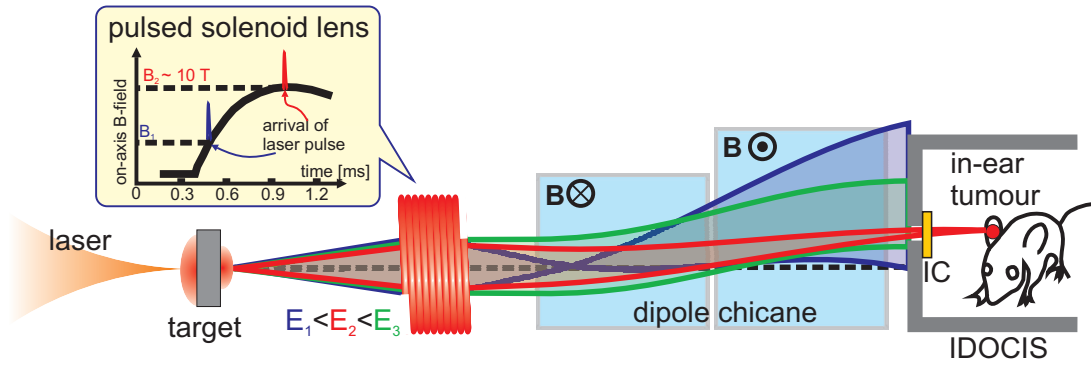


**Fig. 2.9.:** Setup of an *in vivo* experiment to apply a homogeneous depth dose distribution to a tumor growing in the ear of a mouse ( $\propto 1 \text{ mm}^3$ ). The cell irradiation setup presented in Fig. 2.6 is extended by a pulsed solenoid to increase the transport efficiency and to ensure a homogeneous proton depth dose distribution in the tumor. The generated polyenergetic divergent proton beam drifts through a pulsed magnetic solenoid lens [11]. By tuning the temporal delay of the laser pulse arrival relative to the current pulse driving the solenoid the proton energy spectrum can be actively shaped on a shot-to-shot basis as illustrated in the box on the top. The transmission of a certain proton energy ensemble ( $E_1 < E_2 < E_3$ ) through the dipole chicane into the IDOCIS module is optimized according to the on-axis magnetic field ( $B_2$  or  $B_1$ ) at the moment the pulse passes the coil.

could be achieved. Thereby, the methods and components of the presented approach such as real-time transmission dose monitoring can be directly scaled to higher proton energies, later required for proton cancer therapy. However further comprehensive radiobiological investigations have to be performed, thus the work presented here has to be extended to several tumor and normal tissue cell lines as well as to different biological endpoints.

The next step in translational research will be the extension of the experiments to the irradiation of three-dimensional tissues and tumors in animals. In comparison to the studies on biological effects in two-dimensional cell monolayers, these experiments are far more complex and require not only higher, but also tunable proton energies in order to provide a homogeneous spread-out Bragg peak (SOBP). As an outlook a setup of an *in vivo* experiment to apply a homogeneous depth dose distribution to small tumors growing in the ear of mice close to the surface ( $\propto 1 \text{ mm}^3$ ) is shown in Fig. 2.9. The cell irradiation setup presented in Fig. 2.6 is extended by a pulsed solenoid providing a high transport efficiency of up to 20 – 25% [11]. By tuning the delay between laser pulse and solenoid trigger in a multi-shot approach, the energy dependent beam collimation allows to actively shape the spectral intensity of the proton energy spectrum given for the cell location in Fig. 2.6(c). Thus, a homogeneous proton depth dose distribution can be applied to the tumor without the need to shape the energy distribution in the plasma acceleration process.

Independently from the dose delivery system, a further increase in the proton energy of up to 200-250 MeV is required for future proton radiation therapy. In the laser-plasma acceleration community this is presently addressed by exploring novel acceleration schemes [39, 29, 70, 71], target development as well as laser development.

On the basis of the here presented and well characterized proton beam as a reference, but independent of the collaboration within the medical application program, this thesis will now focus on the underlying physical mechanisms of the laser-proton acceleration process in the next chapters. For ultra-short laser pulses, in the next chapter the scaling of the proton energy as function of the laser intensity and acceleration time-scales will be addressed. Afterwards, chapter 4 deals with the investigation of laterally confined targets (reduced mass targets) and their potential ability to increase the proton cut-off energy and to enhance the proton yield per single laser shot.



### 3. Efficient proton acceleration with ultra-short laser pulses

With the invention of the CPA technique [1] laser pulse durations in the sub-picoseconds range and therefore laser intensities in the relativistic regime ( $> 10^{18}\text{W/cm}^2$ ) became accessible for experiments of relativistic laser-matter interaction. Only about fifteen years ago, laser-driven plasmas were discovered to act as an efficient source of high energy (range of few megaelectronvolts per nucleon) ion, and mainly proton beams and first dedicated proof-of-principle experiments have been realized. Since around the year 2000, the target-normal-sheath-acceleration (TNSA) [2, 72] has been established as a robust source of intense multi 10 MeV proton pulses for a wide range of laser and target parameters [73, 74, 19, 75]. Mainly originating from hydrogenated contaminants on the target surfaces, the ions gain initial energy in the electric field that arises when electrons laser-heated to megaelectronvolts temperatures are driven out of the solid target volume (see Fig. 1.1 in chapter 1). For sufficiently long pulses (typically exceeding 100 fs) this mechanism is known to lead to exponential ion energy spectra with a characteristic maximum cut-off energy.

In particular, the achievable ultra-high peak current makes laser-driven ion beams suitable for applications such as inertial confinement fusion or as alternative compact accelerator source for radiation therapy (c.f. chapter 2). Focusing on laser-driven proton pulses, at present, maximum proton energies achieved with high-energy high-power lasers operating in single pulse mode range up to around 70 MeV [18] (for very few particles possibly even 100 MeV [76]). Radiation therapy, however, requires proton energies of up to 250 MeV in order to reach deep seated tumors. Besides the further development of high power laser facilities, the goal of reaching this energy level requires the investigation of the underlying physics and the optimization of the laser-plasma acceleration processes as well as the exploration of novel acceleration mechanisms (refer also to a recent review article by Daido *et al.* [77]). The following list briefly summarizes the most important topics in the field of laser-driven proton acceleration (TNSA related as well as others) addressed in the last few years, all in principle with the same goal, namely, to achieve an increase of the kinetic energy and the yield of the proton beams, to actively control or shape the particle spectrum and to increase the conversion efficiency of laser energy into proton energy:

- Within the TNSA regime, the possibility to accelerate quasi-monoenergetic ion bunches was demonstrated by restriction of the ion source to a small volume where the sheath field is homogeneous, transversely [78, 79] or by thickness reduction [80].

- Recent experiments have shown that a restriction of the target area may confine the dilution of the electron sheath and allow for more efficient re-heating and thus increased proton energies [40, 81] (c.f. chapter 4).
- The TNSA mechanism strongly depends on efficient electron heating at the critical density surface of the target front side, potentially modified by preplasma formation. Therefore the proton acceleration performance as function of the preplasma conditions was investigated by many groups using plasma mirrors or tailored prepulse contrast [82, 83, 84, 37] as well as conical target designs [85, 18, 86]. In particular for ultra-relativistic pulses, the laser light can be absorbed throughout the target volume when relativistic transparency sets in [21, 22, 23, 24].
- As alternative mechanism, radiation pressure acceleration was proposed theoretically [25, 26, 27, 28, 87] (and many others) and investigated experimentally (e.g. [29, 30, 31]). Here, the particles gain energy directly from the radiation pressure of the laser beam. In order to obtain radiation pressure dominated acceleration in experiments, the electron heating has to be strongly reduced by applying circularly polarized light in order to suppress the  $\mathbf{v} \times \mathbf{B}$  force. Furthermore, extreme laser pulse contrast is required to enable the use of ultra-thin targets in order to provide a thin layer of particles to be accelerated. Such contrast conditions are commonly achieved by implementation of plasma mirrors. When the laser interacts with the target the light pressure compresses electrons to a dense layer that is pushed into the target. This gives rise to huge charge separation fields that in turn accelerate the complete ion layer. Although, this mechanism inherently leads to monoenergetic ion spectra and linear energy scaling with laser intensity, unfortunately, it is still a severe challenge to reach radiation pressure dominated conditions in experiments with present laser systems. Thus neither a significant increase in ion energy nor the promising scaling with laser energy could be demonstrated in experiments so far.
- Very recently, laser shock acceleration was proposed and observed in experiments using near-critical-density gas targets and long wavelength CO<sub>2</sub> lasers [70, 39]. Yet, the yield of the observed quasi-monoenergetic proton bunches is significantly smaller when compared to common TNSA results, by several orders of magnitude. However, recent multidimensional particle in cell simulations suggest that injection of the laser-driven shock into a tailored plasma gradient leads to monoenergetic proton beams with therapy relevant energies when state-of-the-art 100 TW class laser pulses are applied [71].

Yet, TNSA remains the most simple and robust approach yielding highest proton energy for given laser parameters and stable operation, as already demonstrated in chapter 2 for the Draco laser by a systematic radiobiological study [46, 47]. Exploring feasible routes toward high proton energies at reasonable pulse repetition rates, the work in this chapter aims for the investigation of the scaling of the TNSA acceleration regime in particular when

operated with an ultra-short pulse high-intensity Ti:sapphire based laser system as Draco.

Generally, the field strength in TNSA increases with electron density and the electron temperature of a thermal plasma sheath around the target surfaces, that is generated by the high power laser as will be discussed in the next section. TNSA is described as an expansion of this plasma sheath, that drives the proton acceleration but is limited due to the dilution of the plasma in the longitudinal and transverse directions with time, leading to a continuous decrease in electron density and temperature, while energy is transferred to the proton ensemble. There are possibilities to circumvent this problem, e.g., by confining the target surface, as mentioned above (refer to chapter 4).

For sufficiently long pulses (typically exceeding 100 fs) and high pulse energy (multiple tens of joules), the TNSA mechanism is known to generally lead to exponential proton energy spectra, with a cut-off energy around 70 MeV [18] that scales with the square-root of the laser intensity. In particular the long pulse duration ensures that the accelerating fields are maintained for a sufficiently long time. However, potential applications require high repetition rate proton pulses such comparably large high energy laser systems cannot provide with. In contrast to that, the use of ultra-short pulse lasers, with high repetition rate but comparably low pulse energies of only a few joules, for reaching energies above 100 MeV seemed to be discouraging at the time when the Draco laser was installed and when the proton acceleration setup was implemented (see chapter 2). However, first promising proton acceleration experiments conducted at Draco in the TNSA regime yielded proton energies of up to 17 MeV, at that time unprecedented for high intensity laser pulses of less than 100 fs duration [19].

The reason for this result is that the application of ultra-short pulses shifts the interest to time-scales where the early phase of the plasma expansion process has to be revisited. Within typical laser pulse durations of 30 fs, the motion of relativistic electrons is restricted to only several micrometer, and thus longitudinal recirculation, a significant transverse expansion or cooling can be neglected during the initial acceleration phase. The original hot electron distribution, depending strongly on the governing laser absorption mechanism and likely to be anisotropic and thus non-thermal in a three dimensional picture, will directly feed the accelerating field. In the second section of this chapter, it will be demonstrated that protons efficiently gain energy during this ultra-short initial period, the intra-pulse phase. The identification of this prethermal intra-pulse phase of the acceleration process furthermore helps to understand the change of the quasi-static proton energy scaling model by Schreiber *et al.* [75] from square-root to near-linear dependence on the laser power when ultra-short pulses are applied as presented in section 3.1.3. The experimental observation of the intra-pulse phase by prominent non-target-normal proton beam emission and its correlation to the effective acceleration time-scale by the help of PIC simulations and further experimental aspects, represents a major result obtained within the frame of this thesis (published in Ref. [20]).

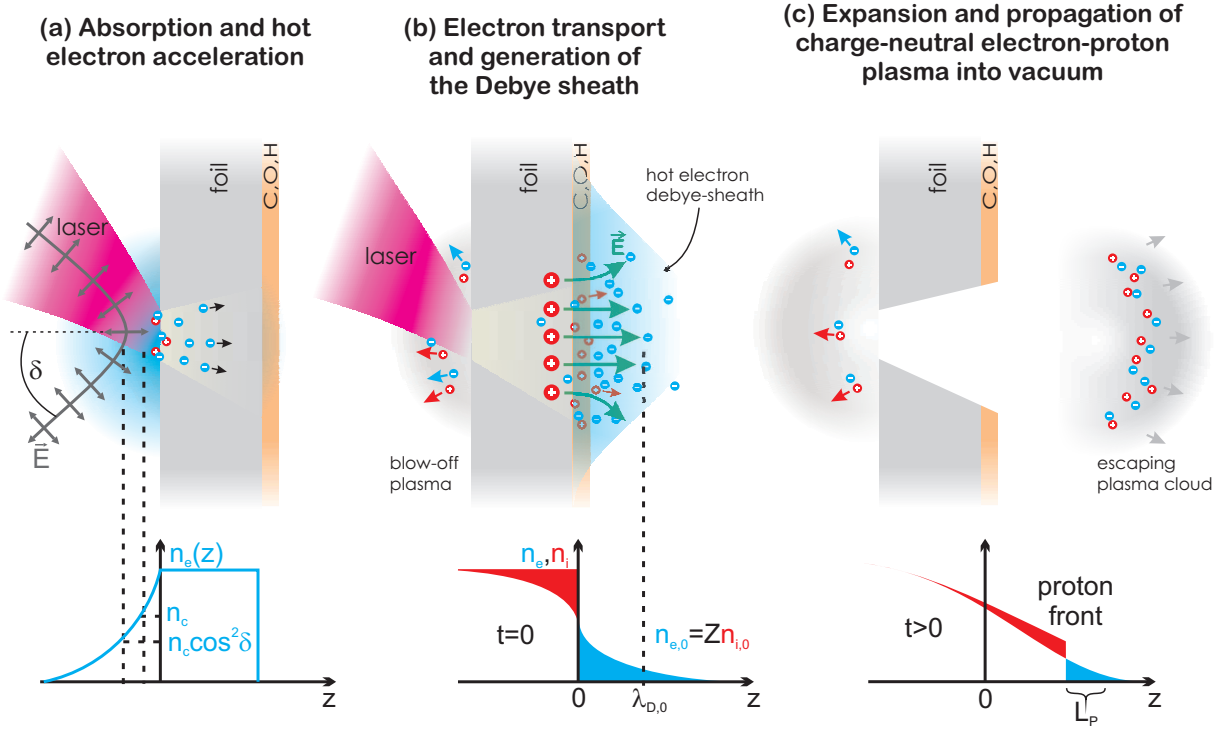


**Fig. 3.1.:** Physical picture of the TNSA process from (a) to (c). The laser with incidence angle  $\delta$  is reflected at the critical density ( $n_c$ ) surface at the target front side. The extreme field strength of the laser generates a plasma and in the vicinity of the critical density of the exponentially decreasing plasma profile laser energy is absorbed by the plasma and hot electrons are accelerated into the target. Those electrons travel through the foil and exit at the rear side, forming an electron cloud with an extension of about a Debye length  $\lambda_{D,0}$ . As a result a large quasi-static electric field is set up ( $\sim TV/m$ ) that leads to ionization of light ions of the contaminant layer and acceleration of those ions to megaelectronvolt energy in the quasi-neutral plasma cloud escaping from the target. In the bottom part of the figure the evolution of the electron and ion density ( $n_e, n_i$ ) with time is shown (further description in the main text). At  $t > 0$ ,  $L_p$  denotes the plasma scale length and is given by  $L_p = \lambda_{D,0}(n_{e,0}/n_e)^{1/2}$  (3.16).

### 3.1. Ion acceleration from thin foils in the TNSA regime

First introduced by Hatchett *et al.* [72] and Wilks *et al.* [2], TNSA has proven to be a potent process for the generation of intense multi 10 MeV proton and ion pulses from laser plasmas at a large number of laser systems. As necessary to interpret the experimental data obtained in this work, this section is dedicated to a revision of the physical picture of the TNSA mechanism displayed in Fig. 3.1. This includes detailed discussion of the three essential phases of the TNSA scheme in Fig. 3.1: (a) laser absorption and hot electron generation, (b) generation of the hot electron Debye sheath and (c) the expansion of the electron-proton plasma into vacuum. Starting with Sec. 3.1.3, experimental data obtained with the Draco laser and novel theoretical considerations building on the established Schreiber model [75] are discussed.

As discussed in chapter 1 and the introduction of this chapter laser-driven ion acceleration

is a secondary process, because ions, due to their high inert mass can only be accelerated in a strong quasi-static charge separation field generated by laser-accelerated electrons in the first place. This can most easily be shown by considering the motion of an electron with mass  $m_e$  experiencing the electric  $\mathcal{E}_L = \mathcal{E}_{L,0} \cos \Theta$  and magnetic  $\mathbf{B}_L = \mathbf{B}_{L,0} \cos \Theta$  field of a plane wave, with  $\Theta = \omega_L t - k_L z$  and  $k_L = 2\pi/\lambda_L$ . For linear polarization of the wave in  $x$ -direction and propagation in  $z$ -direction, the electron motion is described by the relativistic Lorentz equation

$$\mathbf{F} = \frac{d\mathbf{p}}{dt} = -e(\mathcal{E}_L + \mathbf{v} \times \mathbf{B}_L). \quad (3.1)$$

Here  $\mathbf{p} = \gamma m_e \mathbf{v}$ , with  $\gamma = (1 - v^2/c^2)^{-1/2}$  being the relativistic factor and  $\mathbf{v}$  the electron velocity. For a laser with frequency  $\omega_L$  (and wavelength  $\lambda_L$ ), the electron quiver velocity given by

$$v_{\perp} = \frac{e\mathcal{E}_{L,0}}{\gamma m_e \omega_L} \sin \Theta, \quad (3.2)$$

and induced by the electrical component of the Lorentz force

$$F_{\perp} = e\mathcal{E}_{L,0} \cos \Theta \quad (3.3)$$

approaches the speed of light for  $\mathcal{E}_{L,0} \rightarrow \infty$  and the magnetic component of the Lorentz force cannot be neglected anymore. The parameter describing this transition is the dimensionless electric field strength  $a_0 = p_{\perp}^{max}/cm_e$  defined as the maximum electron quiver momentum  $p_{\perp}^{max} = \gamma m_e v_{\perp}^{max}$  (c.f. 3.2) normalized to  $cm_e$ . In practical units the expression

$$a_0 = \sqrt{\frac{I_L \lambda_L^2}{1.37 \times 10^{18} \text{Wcm}^{-2} \mu\text{m}^2}}, \quad (3.4)$$

can be derived where  $I_L = \frac{1}{2} \varepsilon_0 c \mathcal{E}_{L,0}^2$  denotes the laser intensity. This means that for an optical wavelength  $\lambda_L \approx 1 \mu\text{m}$ , intensities above  $10^{18} \text{W/cm}^2$  are called relativistic intensities. The direct acceleration of ions to velocities approaching the speed of light  $v_i \lesssim c$  implies

$$\frac{Z m_e}{M_i} a_0 \sim 1, \quad (3.5)$$

with  $M_i$  denoting the ion mass and  $Z$  the ion charge number and thus would require  $a_0 \sim 2000$ , or intensities in the region of  $I_L > 10^{24} \text{W/cm}^2$ , respectively. Using currently available laser intensities in the range of  $I_L = 10^{20} - 10^{22} \text{W/cm}^2$  (c.f. [88]), laser-driven ion acceleration is therefore only feasible as a secondary process. The ions rest more or less immobile and the electrons can oscillate in the laser field. While for  $a_0 \ll 1$  only transverse oscillations with  $\omega_L$  are possible, in the relativistic case ( $a_0 \gg 1$ ) the magnetic component of the field causes an additional oscillatory motion in  $z$ -direction with  $2\omega_L$  and an average drift velocity of [89]

$$v_D = \frac{a_0^2}{4 + a_0^2} c. \quad (3.6)$$

However, up to now only plane waves were treated, whereas in reality this assumption is immediately violated by the ultra-short laser pulses, exhibiting an intensity envelope strongly varying in time and space through tight focusing, necessary for achieving such high intensities in the experiments. As a result, strong radial intensity gradients are created. While for the case of plane waves, electrons initially at rest return to that state whenever the external field is turned off, and therefore any gain of energy is inhibited, the introduction of the spatially confined intensity envelope leads to net acceleration of electrons. The laser field amplitude and therefore  $a_0$  depends on the spatial coordinate and as soon as an electron reaches a point with less field during a laser cycle, it experiences less restoring force and cannot return to its initial position anymore. The electron is therefore pushed to regions of less intensity or, in other words, of less electric field pressure. Effectively, the so called ponderomotive force

$$\mathbf{F}_p = -mc^2 \nabla \gamma_p(\mathbf{r}) \quad \text{with} \quad \gamma_p(\mathbf{r}) = \sqrt{1 + \frac{a_0^2(\mathbf{r})}{2}} \quad (3.7)$$

experienced by the electrons can be introduced [90]. In the non-relativistic limit (e.g. [91, 89]), the instructive expression

$$\mathbf{F}_p = -\frac{e^2}{4m_e \omega_L^2} \nabla \mathcal{E}_{L,0}^2(\mathbf{r}). \quad (3.8)$$

can be derived, where the ponderomotive force is proportional to the gradient of the cycle-averaged quiver energy of an electron oscillating in the laser field.

Similarly, electrons can gain energy when the laser interacts with a plasma. At high laser intensities the electrical laser field is large enough to field-ionize target atoms and create a plasma. Already short prepulses, pedestals preceding the main pulse ( $I_L > 10^{12} \text{W/cm}^2$ ) or, ultimately, the rising edge of the main laser pulse (e.g. temporal pulse contrast in Fig. 2.2) create a preformed plasma, such that the major part of the pulse, in fact, is always interacting with a plasma. In a simple model a plasma is characterized by an electron population of density  $n_e$ , which when pushed by the laser, is pulled back by the background of the quasi immobile ions and thus oscillates with the plasma frequency

$$\omega_p = \sqrt{\frac{n_e e^2}{\varepsilon_0 \gamma m_e}}. \quad (3.9)$$

Together with the frequency  $\omega_L$  of the laser and neglecting collisions, the refractive index of the plasma is given by

$$n(\omega_L) = \sqrt{1 - \frac{\omega_p^2}{\omega_L^2}} = \sqrt{1 - \frac{n_e}{n_c}}, \quad (3.10)$$

where  $n_c$  denotes the critical density, which in practical units (for  $\gamma = 1$ ) reads

$$n_c = \frac{\varepsilon_0 \gamma m_e \omega_L^2}{e^2} = 1.1 \times 10^{21} (1 \mu\text{m}/\lambda)^2 \text{cm}^{-3}. \quad (3.11)$$

For  $\omega_p < \omega_L$  or  $n_e < n_c$ , respectively, the plasma is called underdense and the laser propagates through the transparent medium. Just for the sake of completeness, it shall be mentioned that a laser modulated plasma wave, which can be generated by focusing a high intensity ultra-short pulse laser onto a gas target, allows for acceleration of electron bunches with narrow bandwidth, gigaelectronvolt energies and high bunch charge (refer to laser wakefield acceleration [92, 93, 94, 95]).

The other case,  $\omega_p > \omega_L$  or  $n_e > n_c$  refers to a dense or overcritical plasma as it is the prevalent scenario of the laser solid interaction in TNSA. Since the refractive index (3.10) of the plasma is purely imaginary, the plasma is opaque for the incident laser beam. Only an evanescent component of the laser field can penetrate into the overdense region up to a characteristic skin depth  $l_s \simeq c/\omega_p$  assuming an exponential plasma density profile and p-polarized light. The laser pulse is then reflected at the surface, where the electron density equals the critical density (3.11) which for the case of oblique laser incidence is a function of the angle of incidence  $n_e = n_c \cos^2 \delta$  [89] (see Fig. 3.1(a)).

Similar to the case of the ponderomotive potential, electrons can gain net energy when pushed behind the critical density surface by the laser field, because there is less restoring force. This is the case, when the oscillation amplitude of the electrons, due to the electric field (Brunel heating [96]) or due to the  $\mathbf{v} \times \mathbf{B}$  force ( $\mathbf{v} \times \mathbf{B}$  heating [97, 98]) exceeds the skin depth  $l_s$ . Another physical effect that enables effective absorption is resonance. When propagating to its turning point the laser light wave resonantly excites a plasma wave at the critical density surface. The resonantly-driven field can become sufficiently intense that wave-breaking occurs and electrons entering the oscillation field are efficiently accelerated into the target bulk (resonance absorption [91]). Only recently, Mulser *et al.* [99] discovered that anharmonic resonance excitation of single electrons is able to accelerate fast electrons to energies well beyond the simple quiver energy.

For the most cases of the interaction of the laser with an overdense plasma, electrons are accelerated into the target and can be assumed to be exponentially distributed with an average kinetic energy of  $k_B T_e$  in the range of few megaelectronvolts. As in plasma physics this acceleration process is commonly called electron heating, the population of the accelerated electrons is referred to as hot electrons with  $T_e$  denoting its hot electron temperature. Inside the target the hot electrons are shielded by cold electrons of the bulk material. In the case of a thin target foil the electrons leave the target but are immediately re-attracted by the huge positive charge of the remaining target ions. Thus the electrons start to oscillate through the target by exiting the target at the front and the rear surfaces. In a quasi-static picture a hot electron sheath with an average extension of a Debye length

$$\lambda_D = \sqrt{\frac{\varepsilon_0 k_B T_e}{n_e e^2}} \quad (3.12)$$

is generated around the target, where  $n_e$  again denotes the hot electron density. The Debye length expresses the characteristic distance a discrete charge is shielded or screened in the

plasma [91]. The charge separation field of this initial stationary state  $t = 0$  between sheath electrons with density  $n_{e,0}$  and the cold quasi-immobile target ions with density  $n_{i,0}(z > 0) = 0$  (for definition of coordinates see bottom part of Fig. 3.1(b)) can be estimated by assuming an electron density which follows a Boltzmann distribution, with a constant electron temperature (isothermal)

$$n_e = n_{e,0} \exp(e\Phi/k_B T_e) \quad (3.13)$$

where  $n_{e,0} = Z n_{i,0}$  is the density of the unperturbed plasma, with  $Z$  being the ion charge number. Integration of the corresponding one-dimensional Poisson equation for the electrostatic potential  $\Phi$  [100] yields the electric field at the ion front ( $z = 0$ )

$$\mathcal{E}_{front,0} = \sqrt{\frac{2n_{e,0}k_B T_e}{e_N \epsilon_0}} \propto \frac{k_B T_e}{e\lambda_D}, \quad (3.14)$$

where  $e_N$  denotes Euler's number. With megaelectronvolt temperatures  $k_B T_e$  and the Debye length (3.12) being in the micrometer range one obtains a field strength of TV/m. This is large enough to field-ionize atoms at the target surfaces, under usual vacuum conditions stemming from a contaminant layer of hydrogen, oxygen and carbon or, if intended, from the target itself [78, 80], and to accelerate them in target-normal direction to final energies of up to several 10 MeV per nucleon, as schematically shown in Fig. 3.1.

The maximum energy the ions can gain is a function of their charge to mass ratio as well as of the strength of the accelerating fields and of the duration for which those fields are maintained. Having the smallest ion mass and the largest charge to mass ratio, protons reach the highest final energy. Otherwise, the final energy of a single ion strongly depends on the time it starts to be accelerated and its original position with respect to the laser axis as the field strength decreases with the distance to the focal region with axial symmetry. It is evident, that the initial field strength depends on the initial kinetic energy and density of the hot electron distribution, and therefore their optimization represents the main goal in order to achieve highest proton energies.

The exact mechanism how ions gain their energy during the interaction process is still a matter of discussion. Two established models, widely used in the community to predict maximum ion energy as well as ion spectrum are discussed in the following sections. Both basically start with the same initial state of a formed Debye sheath as described above. However, while the plasma expansion model by Mora *et al.* [101] evaluates the quasi-self-similar time evolution of an expanding plasma based on a hydrodynamic concept, in the model by Schreiber *et al.* [75] the maximum achievable ion energy is derived by integrating the equation of motion applying a static electric field potential. In both models, the pulse duration is a characteristic criteria to truncate the acceleration after a certain time. Another approach, basically evaluating the strong charge-separation field induced by a negatively charged cloud of electrons at the rear target-vacuum interface may be consulted in Ref. [102,



103, 104]. Furthermore, it has to be mentioned, that many groups in the community develop particle in cell codes in order to numerically treat the same mechanisms and to explore the underlying physics.

### 3.1.1. Plasma expansion model

Inspired by the pioneering theoretical work by Gurevich *et al.* [105], the concept of plasma expansion into vacuum has been studied over the last decades, both experimentally and theoretically. The strength of the concept for the description of laser ion acceleration relies on its capability to explain a variety of effects observed in experiments. In order to provide the basic ideas of the plasma expansion model, the work by Mora *et al.* [101] predicting maximum ion energy and spectrum is reviewed in the following.

Starting with the step like ion density profile in half space (one-dimensional) as described in the previous section, the laser induced ion plasma expanding into the vacuum can be described as an isothermal and free plasma expansion by use of the equations of continuity and motion [91, 89]. Assuming quasi-neutrality  $n_e = Zn_i$  leads to the self-similar solution for density and ion front velocity

$$\begin{aligned} n_e &= n_{e,0} \exp\left(-\frac{x}{c_s t} - 1\right) \\ v_{front,i} &= c_s + x/t \end{aligned} \quad (3.15)$$

where  $c_s = (Zk_b T_e / M_i)^{1/2}$  denotes the ion sound speed. The index 0 refers to the initial condition  $t = 0$ .

For the system evolving in time ( $t \rightarrow \infty$ ), the self-similar solution has no physical meaning, as long as the density scale length  $L_p = c_s t$  of the expanding ion plasma is smaller than the local Debye length [101]

$$\begin{aligned} \lambda_D(t) &= \sqrt{\frac{\varepsilon_0 k_B T_e}{n_e(t) e^2}} = \lambda_{D,0} \sqrt{\frac{n_{e,0}}{n_e(t)}} \\ &= \lambda_{D,0} \exp\left(\frac{1 + x/c_s t}{2}\right), \end{aligned} \quad (3.16)$$

because all charge separation fields to drive any expansion are completely shielded. Therefore, it is reasonable to estimate the position of the ion front by truncating the density profile at the point where local Debye length  $\lambda_D$  equals the density scale length  $L_p = c_s t$  which yields

$$1 + x/c_s t = 2 \ln(\omega_{p,i} t) \quad \text{and with (3.15)} \quad v_{front,i} = 2c_s \ln(\omega_{p,i} t) \quad (3.17)$$

where  $\omega_{p,i} = \sqrt{n_{e,0} Z e^2 / M_i \varepsilon_0}$  denotes the ion plasma frequency (c.f. (3.9)). The resulting

front velocity implies an electric field at the ion front of

$$\mathcal{E}_{front} = \frac{2c_s M_i}{Zet}. \quad (3.18)$$

Mora *et al.* [101] introduced a simple interpolation formula between (3.14) and (3.18)

$$\mathcal{E}_{front} \approx \sqrt{\frac{4n_{e,0}k_B T_e}{\varepsilon_0 (2e_N + \omega_{p,i}^2 t^2)}}. \quad (3.19)$$

that is valid at any time. By integration of  $v_{front}(t) = \int_0^t ZeE_{front}(t')/M_i dt'$ , the ion front velocity can be calculated at any time and one finally obtains expressions for the final cut-off ion energy as function of the time

$$E_{max} \simeq 2Zk_B T_e \left[ \ln \left( \tau(t) + \sqrt{\tau^2(t) + 1} \right) \right]^2 \quad (3.20)$$

with  $\tau = \omega_{p,i}t/\sqrt{2e_N}$  and the ion spectrum per surface unit

$$\frac{dN}{dE}(E, t) = \frac{n_{i,0}c_s t}{\sqrt{2Zk_B T_e E}} \exp \left[ -\sqrt{\frac{2E}{Zk_B T_e}} \right] \quad (3.21)$$

commonly referred to as the popular isothermal plasma expansion model by Mora.

Note, that so far the model only treats the plasma rarefaction applying an infinite reservoir of energy that maintains a constant electron temperature (isothermal) during the expansion, while in reality the electrons cool down with time by transferring their thermal energy to the plasma ions. Addressing this issue, several studies [3, 106, 107] investigated the time evolution of the electron distribution function as well as the role of the cold electron population, in order to take into account the finite amount of laser energy for the hot electron generation and to provide an intrinsic limitation for the diverging maximum ion energy in (3.20). Therefore the effective acceleration time  $t_{acc}$  in  $\tau = \omega_{p,i}t_{acc}/\sqrt{2e_N}$  not only limits the expansion process from a more heuristic point of view, but as a pulse duration dependent quantity its physical meaning is closely related to the cooling of the hot electron distribution. Using an empirical approach for the acceleration time by estimating  $t_{acc} = 1.3 \times \tau_L$  with  $\tau_L$  denoting the pulse duration of the laser, Fuchs *et al.* [73] successfully applied the plasma expansion model to relate the maximum proton energy obtained at different laser systems, predominantly long pulse systems providing pulse durations of several hundreds of femtoseconds. For ultra-short pulses  $\tau_L < 100$  fs, the same group [108] introduced the empirical expression  $t_{acc} = 1.3 \times (\tau_L + t_{min})$  (for intensities of  $\geq 3 \times 10^{19}$  W/cm<sup>2</sup>) taking a minimal time  $t_{min} = 60$  fs for the energy transfer from electrons to the ions into account. Moreover, the ion spectra measured in various experiments typically exhibit an exponentially decaying behavior which is in good agreement with the prediction of the model (3.21).

The plasma expansion model has been widely used in the last decade not only to predict

ion energies but also to describe different experimental signatures. Just to mention a few examples, the laminar kind of the plasma sheath expansion explains the ultra-low emittance of the accelerated proton beam, that has been observed by Cowan *et al.* [4]. Spectral modulations of the ion spectra due to screening effects between multiple ion species were identified [109, 110] and finally, the sheath expansion concept helped to explain the results of proton radiography [6] or proton beam steering [111, 112].

However, it has to be pointed out again that the model represents a treatment in one dimension only. Multi-dimensional scenarios are usually investigated using numerical modeling with hydrodynamic or particle in cell simulation codes. Moreover, the time evolution of the initial conditions of the semi-finite plasma slab, namely a time-dependent development of the initial electron density distribution and a possibly effective ion acceleration during this phase (later referred to as prethermal phase see Sec. 3.2) has never been considered so far, but would be important to be included into the model as will be demonstrated by the experimental results discussed later in this chapter. Finally, for the prediction of the maximum ion energy as well as the ion spectrum using equations (3.20) and (3.21), the exact knowledge of the hot electron temperature  $T_e$  and its scaling with the laser intensity is mandatory. This in fact requires a detailed understanding of the laser to plasma energy conversion mechanisms, that will be briefly addressed in the next section.

### 3.1.2. Hot electron generation

The issue of the laser-plasma interaction physics is still a controversial topic, because it consists of many competing effects caused by laser intensity, target material, temporal laser contrast ratio, and so on. Therefore a detailed picture is very demanding, because all external parameters have to be considered, but often are unknown in the experiments. Since the 1980s, a variety of different absorption mechanisms have been proposed to describe the interaction of ultra-short intense laser pulse interaction with dense matter. However, due to the huge challenge to determine the experimental conditions, but also due to the complex interplay of the underlying physical principles in the large laser intensity range of more than ten orders of magnitude during a single interaction event, it is very difficult to isolate an absorption mechanism, either experimentally or even in a simulation.

For low intensities up to about  $10^{15}\text{W}/\text{cm}^2$  [89], collisional absorption processes dominate, where electrons oscillate in the incident laser field and dissipate their energy by collisions with ions and other electrons in the plasma. Although the laser intensities of present laser systems exceed this intensity range by orders of magnitude, the intensity level of a preceding ASE pedestal or short pulse prepulses may in fact lead to significant collisional heating of a preplasma and can therefore significantly contribute to a change of the interaction conditions, and thus of the absorption physics for the intense main pulse.

For the absorption of the intense main pulse several collisionless absorption mechanisms were proposed, whereas for the Draco laser parameters, namely highly relativistic intensities

( $10^{21}\text{W}/\text{cm}^2$ ) and small but significant preplasma (scale length  $L_p \lesssim \lambda$ ), the  $\mathbf{v} \times \mathbf{B}$  force [97] dominates the electron acceleration process. This will be confirmed by experimental observations as well as PIC simulation results, both obtained for the Draco laser parameters, and discussed in Sec. 3.2.3. Therefore, the following considerations on the scaling of the hot electron temperature  $k_B T_e$  will be predominantly based on the  $\mathbf{v} \times \mathbf{B}$  force. Detailed treatment of further important absorption mechanisms such as resonance absorption playing a role for a preplasma scale length of  $L_p \gtrsim \lambda$  as well as the well-known Brunel heating [96] occurring for weakly relativistic laser intensities ( $a_0 \sim 1$  where the  $\mathcal{E}$  field component of Lorentz force dominates) and very sharp plasma gradients ( $L_p \ll \lambda_L$ ) requiring extreme laser pulse contrast (c.f. [113]), may be consulted in Ref. [91, 89, 90, 114].

For  $\mathbf{v} \times \mathbf{B}$  dominated absorption, the hot electron temperature is assumed to correspond to the average energy of an exponential electron distribution, given by the cycle-averaged kinetic energy  $W$  of an electron oscillating in the electromagnetic field of a laser [2, 72]

$$W = m_e c^2 (\bar{\gamma} - 1) = k_B T_e, \quad (3.22)$$

where  $\bar{\gamma}$  is the relativistic factor averaged over a laser-cycle. This kinetic energy  $W$  is equivalent to the transverse electron quiver energy in  $x$ -direction, parallel to plasma surface (see Fig. 3.1). Analyzing the simple time-average [89, 90, 115] of the  $\gamma$  factor in (3.22) (defined by the relativistic energy-momentum relation  $\gamma = (1 + p^2/m_e^2 c^2)^{1/2}$ ) one finds

$$\bar{\gamma} = \langle \gamma \rangle_t = \left\langle \sqrt{1 + \frac{p_x^2}{m_e^2 c^2}} \right\rangle_t \approx \sqrt{1 + \frac{a_0^2}{2}}. \quad (3.23)$$

where  $a_0$  denotes the normalized electric field amplitude defined in (3.4). This yields the popular ponderomotive scaling of the hot electron temperature [2, 72]

$$k_B T_e = m_e c^2 \left( \sqrt{1 + \frac{a_0^2}{2}} - 1 \right) \simeq 1 \text{ MeV} \sqrt{\frac{I \lambda^2}{10^{19} \text{ W}/\text{cm}^2 \mu\text{m}^2}}. \quad (3.24)$$

Note, that strictly speaking, this scaling is based on a non-relativistic treatment, because the longitudinal  $\mathbf{v} \times \mathbf{B}$  force in  $z$ -direction is ignored by the calculation of the simple time-average of the transverse electron quiver energy, which in fact only holds true for  $a_0 \ll 1$ . However, from momentum conservation using the relativistic Lorentz equation it can be deduced that in a first approximation, the ponderomotive force is balanced by the electric force arising from charge separation fields in the plasma [90, 116] as soon as electrons are shifted with respect to the ion background. In particular for the case of relativistic intensities  $a_0 \gg 1$  this is important, because independent of the laser incidence angle transverse electron motion is always transformed into longitudinal energy that is absorbed by the plasma [115]. Therefore, it is reasonable to maintain the assumption, that at the critical density surface, where the relativistic pulse is basically absorbed any longitudinal forces can be neglected and

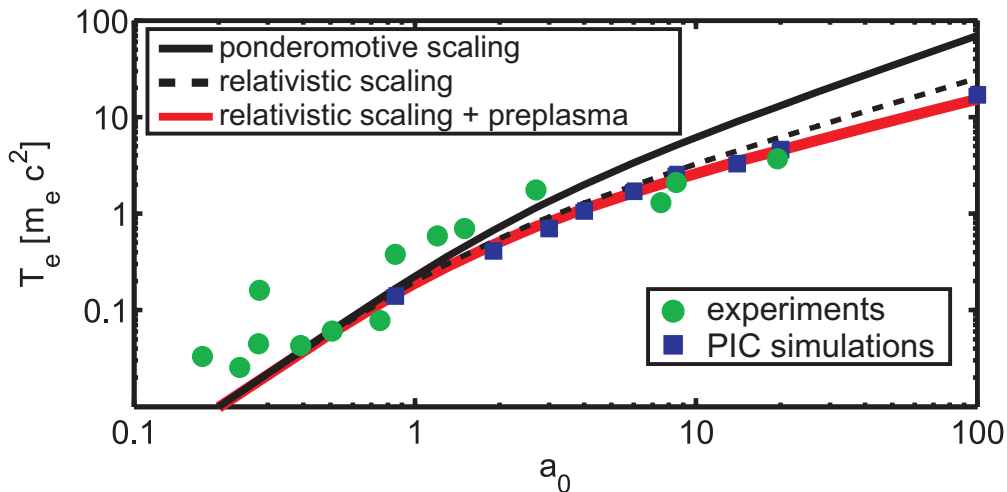


**Fig. 3.2.:** Comparison of various temperature scalings with selected experimental values from literature (all values correspond to setups using normal laser incidence on target) and PIC simulations. For further details, the reader may refer to the publication by Kluge *et al.* [117], where this figure is extracted from. The different scaling curves are explained in the main text: black solid line corresponds to the ponderomotive scaling eq. (3.24), the black dashed line to the relativistic scaling eq. (3.25) and the red solid line to an implicit solution of the relativistic scaling when a long preplasma is taken into account (see Ref. [117]).

to deduce the electron temperature by calculating the energy of the relativistic transverse electron quiver motion.

A rigorous relativistic treatment, however, excludes the simple cycle-average method [90], because the laboratory time is no Lorentz invariant anymore, but transforms as  $t' = t/\gamma$ , called the proper time  $\tau$  of the electron in the co-moving system. This implies that the distribution of electrons with regard to the laboratory time is not uniform anymore. In a recent publication, Kluge *et al.* [117] demonstrated, that this problem can be circumvented by switching to the Lorentz invariant phase coordinate for calculating the ensemble average of the transverse electron energy distribution of  $m_e c^2(\bar{\gamma} - 1)$  in equation (3.23). The basic concept is that, unlike the case of the time coordinate, the electron distribution with respect to the invariant proper time can easily be calculated ( $dN/d\tau = \text{const}$ ).

Furthermore, presuming a negligible preplasma scale length, a novel hot electron temperature scaling

$$\begin{aligned}
 k_B T_e &= m_e c^2 \frac{a_0}{4} & (a_0 \ll 1) & \quad (3.25) \\
 k_B T_e &= m_e c^2 \left\{ \frac{\pi a_0}{\ln 16 + 2 \ln a_0} - 1 \right\} & (a_0 \gg 1) &
 \end{aligned}$$

can be derived. The first line of this equation represents a direct approximation of the ponderomotive scaling (3.24) whereas the  $a_0 \gg 1$  case predicts much weaker scaling with the laser field amplitude.

As shown in Fig. 3.2, the model predictions (black dashed line) compare very well with PIC

simulation as well as experimental measurements of the hot electron temperature available in literature (for more details see Ref. [117]). In the regime of  $a_0 \ll 1$ , the simple ponderomotive scaling (black solid line) is still accurate. But for relativistic intensities  $a_0 \gg 1$ , the ponderomotive scaling overestimates the hot electron temperature increase. The analysis of a case including a large amount of preplasma to be present in front of the foil surface, e.g. due to laser prepulses or ASE, yields an expression for the average kinetic energy that has to be integrated numerically [115, 117]. An according solution is overlaid in Fig. 3.2 as red solid line showing perfect agreement with the PIC simulations when considering a near-critical density plasma.

### 3.1.3. Quasi-static description and the novel case of ultra-short laser pulses of Draco

As mentioned above, the model by Schreiber *et al.* [75] represents another approach to model the achievable ion (here mainly protons are considered) energy from laser-driven plasma acceleration. In that particular concept, the proton energy is estimated by integrating the equation of motion in a static electric field generated by a positive surface charge at the target rear side that is created when the hot electron cloud leaves the target. Thus, without consideration of the time-dependent plasma expansion, the quasi-static character TNSA exhibits, is emphasized. As it turns out, the maximum achievable proton energy scales similarly with the laser intensity as predicted by the plasma expansion model (c.f. equation (3.24)) but it has no explicit dependence on the hot electron temperature [75], that was given attention to in the previous section. Here the physical problem of the laser energy conversion into plasma energy is shifted to the absorption efficiency, as the quantity that contains the complex physics.

But before reviewing the theoretical concept of Schreiber's model, the compilation of important experimental measurements of the maximum proton energy values as function of the laser power shown in Fig. 3.3 is discussed. The data was obtained for a large variety of laser parameters in the last years. In particular recent data obtained throughout this thesis with ultra-short pulses of Draco triggered novel aspects of the proton energy scaling with laser power that were interpreted by re-consideration of the model in the limit of ultra-short pulse durations (refer also to Ref. [19]).

When the Draco system at the HZDR came online (in 2009), laser-driven proton acceleration with maximum proton energies well above 10 MeV could only be observed when high power high energy glass lasers were applied for the irradiation of thin foils as summarized by the open circles in Fig. 3.3. At that time, maximum energies reached with short pulse lasers were generally limited to only a few MeV as illustrated by the coloured diamonds where the colour represents the typical ranges of pulse durations of such lasers of  $\tau_L = 30 \dots 100$  fs. While for the aforementioned long pulse high power lasers with  $\tau_L \gg 100$  fs a clear scaling of the maximum proton energies with the square-root of the laser power could be established

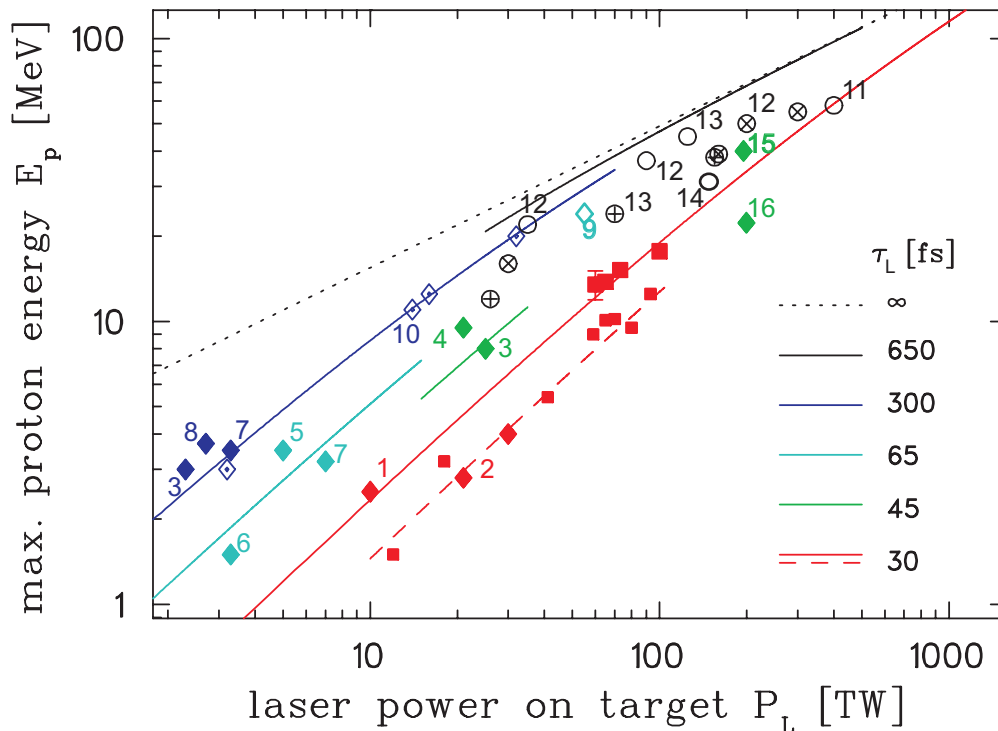


**Fig. 3.3.:** *Scaling of the maximum proton energy with laser power. Red squares represent experimental results obtained with the Draco laser varying the laser energy between 0.3 and 3 J (small squares:  $d = 5 \mu\text{m}$  target thickness, big square:  $d = 2 \mu\text{m}$ ). Filled diamonds stand for experiments performed with Ti:sapphire lasers of around 1 J energy (1: Lund [118], 2: J-Karen [119, 9], 3: MBI [75, 120], 4: LOA [121], 5: Saclay [113], 6: Astra [122], 7: Jetti [123], 8: Atlas [82]), partially (3,7) operated at longer pulse length than usual. (15,16) correspond to very recent results (2012) at J-Karen (7 J, 40 fs) [124] and Astra Gemini ( $\sim 8$  J, 40 fs) [125]. The open diamond (9) represents a 5 J experiment at Janusp [126], the dotted diamonds (10) show results of an energy scan applying up to 10 J on target at LULI [73]. Open circles (11,12,13,14) stand for single shot experiments at the glass laser facilities LLNL NovaPW [127], RAL Vulcan [128], Los Alamos Trident [129, 130] and Phelix GSI [131]. Marked circles represent energy scans ranging up to 300 J performed at Vulcan and Trident [74, 129]. The colour code of the experimental points corresponds to the different pulse duration regimes given in the legend for the curves following eq. 3.28. Representative sets of parameters are chosen for  $(r_L [\mu\text{m}], d [\mu\text{m}], \vartheta [^\circ])$ , i.e. (1.7-2.3, 2, 10) for  $\tau_L = 30 - 65$  fs with the exception of the dashed red line where  $d = 5 \mu\text{m}$ , (3, 15, 15) for  $\tau_L = 300$  fs, and (5, 15, 30) for  $\tau_L > 500$  fs. The efficiency  $\eta = 0.2$  is chosen for the short-pulse case as described in the text.*

experimentally [73] no obvious dependence could be obtained from the short pulse laser data, having been partly due to the fact that these sub 10 TW lasers were operating close to the MeV proton energy threshold. As reported in the following, this situation has changed with the implementation of 100 TW class ultra-short pulse lasers ( $\tau_L \sim 30$  fs) not only at the HZDR but also in other laboratories worldwide.

The red squares in Fig. 3.3 represent results from systematic studies at Draco (for setup refer to Sec. 2.2) where the laser energy has been varied while keeping its pulse duration and focusing parameters constant. Maximum proton energies of up to 17 MeV, and even up to 20 MeV using normal laser incidence on target, have been reached within this work and

have thus considerably extended the energy range accessible with compact ultra-short pulse laser systems.

In the last couple of years this range of achievable maximum proton energy of 10–15 MeV from TNSA using 100 TW class ultra-short pulsed lasers ( $\tau_L \leq 50$  fs) has been confirmed in several experiments by different groups, such as LOA (14 MeV, private communication by A. Flacco), MBI [132](about 8 MeV), INRS [133] and Hercules [37]. In particular, recent results of the achieved maximum proton energy exceeding 20 MeV, with high proton yield measured with RCF stacks at the Astra Gemini laser with  $\sim 8$  J on target and 40 fs pulses [125] and, most recently, CR39 measurements using foils of aluminum ( $0.8 \mu\text{m}$ ) and stainless steel ( $2 \mu\text{m}$ ) irradiated at the J-Karen laser [124] using 7 J and 40 fs pulses ( $I \sim 10^{21} \text{W}/\text{cm}^2$ ) at oblique incidence showing protons with energies exceeding 40 MeV (see also Fig. 3.3) are very encouraging.

Yet another important result shown in Fig. 3.3, is that for the ultra-short pulse durations the scaling of the maximum proton energy with laser power has been found to significantly deviate from the well-established square root scaling. To emphasize this finding, the Draco data is re-plotted in Fig. 3.4 using a linear energy scale instead of the log scale. In the same figure a very similar data set recently measured at the MBI [132] and showing excellent agreement is included. This faster near-linear proton energy scaling with laser power for ultra-short laser pulses can basically be understood as a consequence of the three-dimensional field distribution in the vicinity of the target rear surface. As mentioned above, the analytical model by Schreiber *et al.* [75] will be used in a novel interpretation to illustrate the transition between the two scaling regimes.

### Proton energy scaling for ultra-short pulses

Schreiber's model is based on the assumption that a relativistic laser pulse of pulse duration  $\tau_L$  accelerates  $N_e$  electrons from the target front side to an average energy  $E_e$ . The total number of electrons is determined by the efficiency  $\eta$  of the conversion of laser energy  $E_L$  into electron energy  $N_e E_e = \eta E_L$ . The electron bunch of length  $\tau_L c$  leaves the target rear side spread to a circular area of radius  $R = r_L + d \tan \vartheta$ , where  $r_L$  denotes the radius of the laser focal spot,  $d$  the thickness of the irradiated thin foil and  $\vartheta$  the half-angle of the propagation cone. As a consequence a positive surface charge  $Q_e/(\pi R^2)$  is induced at the rear side of the target. It leads to the on-axis potential distribution

$$\Phi(r = 0, \zeta) = -\frac{Q_e}{2\pi\epsilon_0 R} \cdot \left(1 + \zeta - \sqrt{1 + \zeta^2}\right) \quad (3.26)$$

where  $\zeta = z/R$  stands for the normalized propagation direction normal to the foil. Electrons of average energy  $E_e$  are forced to turn around at a distance  $\zeta_t = E_e/E_\infty$  assuming  $\zeta_t \ll 1$ . The equation of the equilibrium number of electrons outside of the foil with the induced surface charge  $Q = 2N_e(\zeta_t R)/(\tau_L c)$  allows for the rewriting of the potential barrier  $E_\infty =$



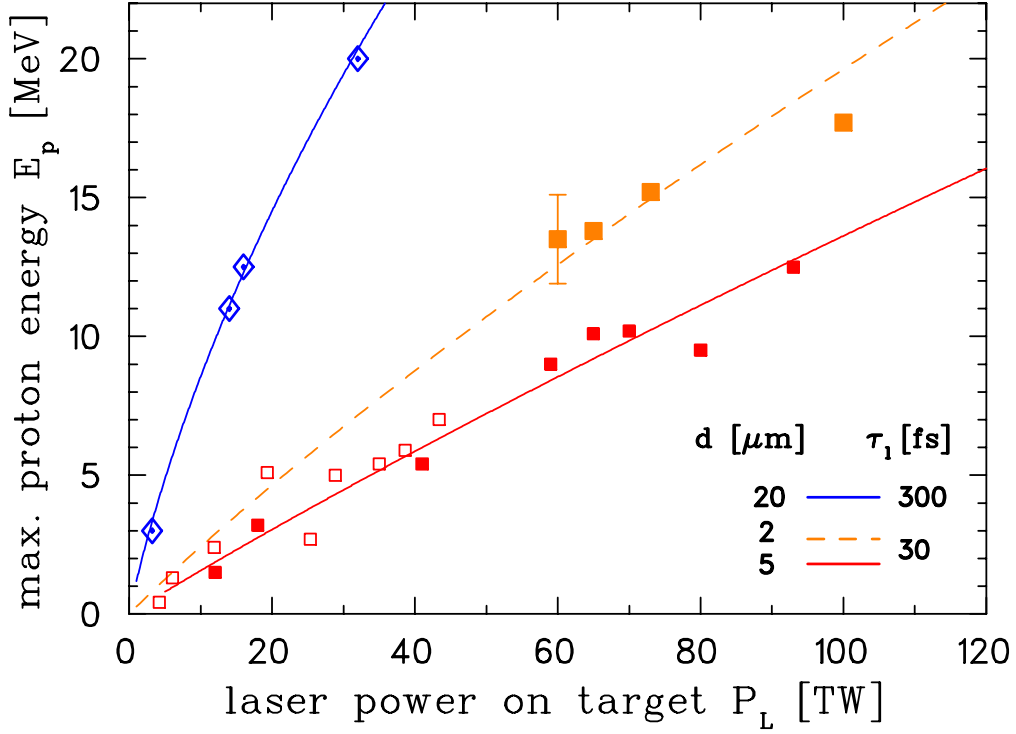


**Fig. 3.4.:** Selection of maximum proton energy sets with laser power using a linear energy scale to further illustrate the transition in scaling with the laser pulse duration applied. Again the data points obtained at the Draco laser as in Fig. 3.3 (filled squares for  $d = 5 \mu\text{m}$  in red and for  $d = 2 \mu\text{m}$  in orange) are plotted and directly compared with a very similar data (empty red squares) set obtained at the MBI facility (45 fs pulses with up to 1.2 J on target, focal spot size about 4-5  $\mu\text{m}$ ) and published in Schnuerer et al. [132]. The latter were obtained with normal laser incidence on target and therefore the power was scaled to match the intensity at oblique incidence ( $45^\circ$ ).

$Qe^2/(2\pi\epsilon_0 R)$  in eq. 3.26 as a function of the laser power  $P_L = E_L/\tau_L$

$$E_\infty = 2m_e c^2 \sqrt{\frac{\eta P_L}{P_e}} \quad (3.27)$$

using the relativistic power unit  $P_e = m_e c^3/r_e = 8.7 \text{ GW}$ . Up to this point, no assumption has been required about the energy distribution of the hot electrons. Nevertheless, when applying an exponential distribution with  $E_e = k_B T_e$ , the turning point of electrons with  $E_e$  running up the potential corresponds to the hot electron Debye length  $\lambda_D$  and the surface field is consistent with the one resulting from solving Poisson equation (3.14) and used as the initial condition for the plasma expansion model in Sec. 3.1.1.

The energy of a laser-accelerated proton is now deduced from the potential caused by the induced surface charge at the actual position of the proton  $\zeta$  to  $E_p(\zeta) = -e\Phi(r=0, \zeta) = -E_\infty \cdot (1 + \zeta - \sqrt{1 + \zeta^2})$ . The size of the surface charge thus influences the energy gain of protons close to the surface ( $\zeta = z/R < 1$ ). For a quantitative analysis of the maximum energy  $E_{max}$  a proton can reach, the integration of the equation of motion up to the duration

of the laser pulse leads to an implicit function [75] that can be approximated by

$$\begin{aligned}
 E_{max} &= E_{\infty} \cdot \tanh^2 \left( \frac{\tau_L}{2\tau_0} \right) \\
 &\rightarrow E_{\infty} \cdot \left( \frac{\tau_L}{2\tau_0} \right)^2 \propto \eta P_L \quad \text{for } \tau_L \ll 2\tau_0 \\
 &\rightarrow E_{\infty} \propto \sqrt{\eta P_L} \quad \text{for } \tau_L \gg 2\tau_0.
 \end{aligned} \tag{3.28}$$

The reference time  $\tau_0 = R/v_{\infty} = R/(2E_{\infty}/m_p)^{1/2}$  is used to emphasize the time the proton remains in the vicinity of the accelerating surface charge. It directly follows that for acceleration times and thus pulse durations shorter than twice the reference time  $\tau_0$  the scaling of the maximum proton energy with laser power is near-linear. This situation applies for the Draco data presented in Fig. 3.3, where for  $P_L \sim 100$  TW the reference time amounts to  $\tau_0 \sim 20$  fs and the pulse duration to  $\tau_L = 30$  fs. Using the measured focal radius of  $r_L = 1.7 \mu\text{m}$ , a well established propagation angle of  $\vartheta = 10^\circ$  and assuming a conversion efficiency of  $\eta = 20\%$  (adapted to match the plotted data) our experimental data is well described by eq. (3.28), where the red solid line in Fig. 3.3 corresponds to a target thickness of  $d = 2 \mu\text{m}$  and the dashed line to  $d = 5 \mu\text{m}$ . As it is not the intention here to discuss the absolute proton energies achievable with long pulse lasers but only the scaling behavior in relation to the short pulse case, the increase of the absorption efficiency to up to 50% [73], being well established for the long pulse laser class, has been ignored in all the curves in Fig. 3.3.

The transition of the two scaling regimes (3.28) is qualitatively illustrated in Fig. 3.5. As introduced above, the accelerating fields can be regarded as originating from the potential (3.26) of the circular positive surface charge  $Q$  (radius  $R$ ) which is built up by hot electrons accelerated by the laser and ejected at the target rear. Thus, the on-axis electric field distribution in a first order approximation is given by  $\mathcal{E}(z) \propto 1 - z/\sqrt{z^2 + R^2}$  with  $z$  being the propagation distance of the proton. As long as protons stay in the vicinity of the target (distance from target  $R$ ) they experience the field of the laterally confined charge distribution, whereas at larger distance a point like source can be approximated. In conclusion the accelerating field  $\mathcal{E}(z)$  a proton experiences in the vicinity of the target ( $z_1, z_2 < R$  for  $\tau_L \ll 2\tau_0$ ) scales stronger with the laser power than far away from the target ( $z_1 < R < z_2$  for  $\tau_L \gg 2\tau_0$ ).

### Limits of the scaling at increased laser power

For higher powers of ultra-short pulses the influence of the source size diminishes, as the reference time  $\tau_0$  decreases and the same holds true for longer laser pulses and thus increasing acceleration times. For all cases the scaling converges to the square-root scaling for  $\tau_L \gg 2\tau_0$ , leading to the curvature of, e.g., the red solid line in Fig. 3.3. The corresponding black dotted line in Fig. 3.3 therefore represents an upper limit of the proton energy for a given

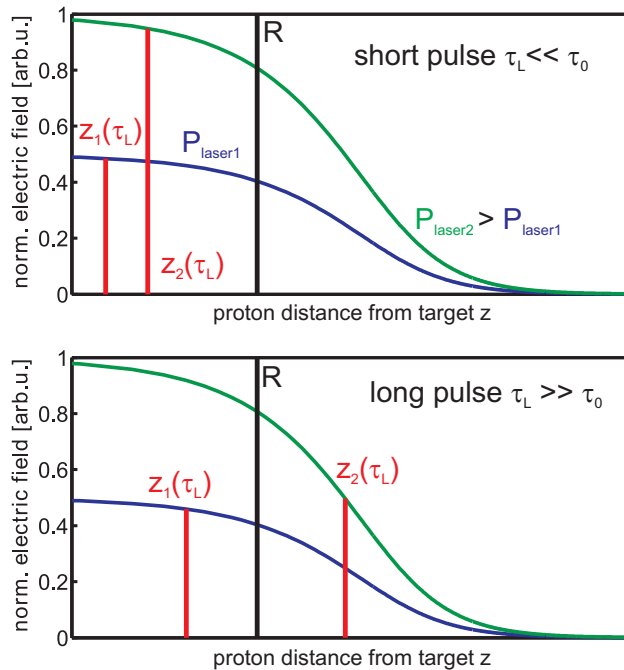


**Fig. 3.5.:** Illustration of the discussed change in the scaling behavior with pulse duration. The normalized electrical field  $\mathcal{E}(z) \propto 1 - z/\sqrt{z^2 + R^2}$ , induced by different laser powers  $P_{\text{Laser1}}$  (blue) and  $P_{\text{Laser2}}$  (green), is plotted as function of the distance of the proton to the target  $z$  for short (top) and long (bottom) pulse durations.

laser power, provided the conversion efficiency is assumed to be constant. However, for a constant laser pulse duration,  $\tau_0$  only weakly decreases with increasing laser pulse energy  $\tau_0 \propto E_L^{-1/4}$ , which in principle means, that the near-linear scaling of (3.28) can be applied for ultra-short pulse ( $\tau_L = 20 - 30$  fs) lasers up to the petawatt level, where the ratio  $\tau_L/2\tau_0$  remains below one. This is illustrated in Fig. 3.6(a) by plotting  $\tau_L/2\tau_0$  as function of the laser pulse energy for different values of the laser pulse duration.

Note, that apart from the transition between the different intensity scaling regimes, intrinsically the model favors short laser pulse durations in terms of optimal acceleration conditions. While keeping all other parameters constant, for a certain laser energy, the maximum proton energy

$$E_{max} \propto \sqrt{\frac{E_L}{\tau_L}} \tanh^2 \left( \text{const.} \times \sqrt[4]{E_L \tau_L^3} \right) \quad (3.29)$$

is optimized either by a long effective acceleration time, represented by the  $\tanh^2$ -term and favoring high values of  $\tau_L$ , or by a large laser power and therefore short laser pulse durations. The latter leads to a large potential barrier  $E_\infty$  and thus contributes to a higher amplitude of the accelerating field. While the  $\tanh^2$ -term saturates for large arguments, the preceding factor in (3.29) becomes dominant when the laser energy is increased and thus the maximum proton energy is optimized for shorter laser pulses. Applying laser and target parameters according to the Draco experiments, Fig. 3.6(b) shows the curve of the optimal

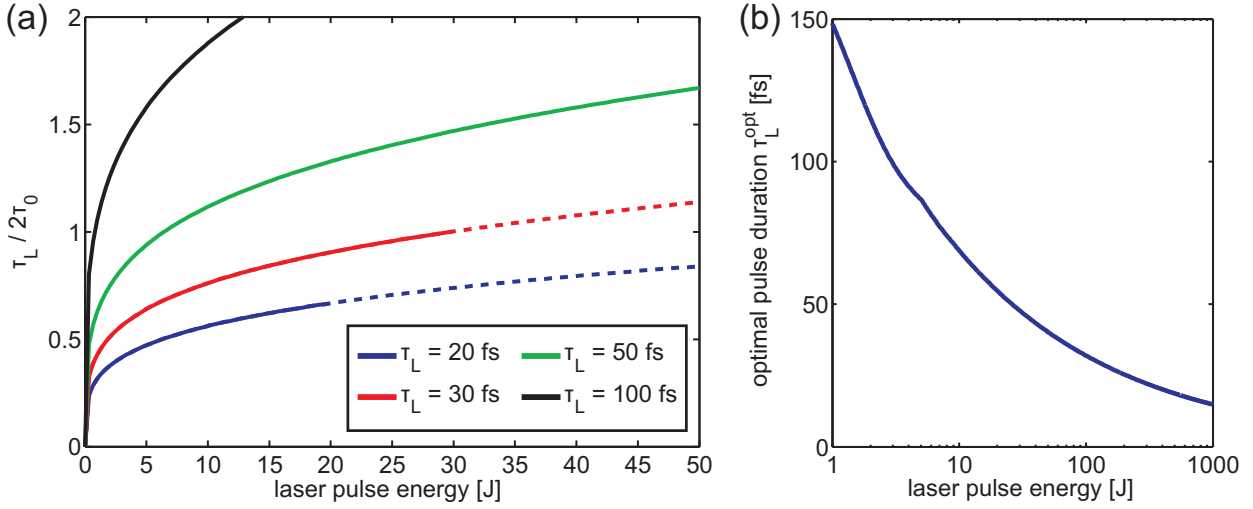


**Fig. 3.6.:** (a) Ratio  $\tau_L/2\tau_0$  plotted as function of the laser energy and different laser pulse durations. Once the laser energy yields a power larger one petawatt the curves continue as dashed lines. The curves were calculated using Draco parameters  $r_L = 1.7 \mu\text{m}$ ,  $d = 5 \mu\text{m}$ ,  $\vartheta = 10^\circ$  and  $\eta = 0.2$ . (b) For the same parameters the trend of the optimal pulse duration  $\tau_L^{opt}$  with increasing laser energy is shown.

laser pulse duration  $\tau_L^{opt}$  as function of the laser pulse energy, calculated by differentiating (3.29) with respect to  $\tau_L$  and setting  $dE_{max}/d\tau_L = 0$ . A more detailed analysis presented in Ref. [134] reveals that the  $\tau_L^{opt}$  decreases with increasing laser energy by  $\tau_L^{opt} \propto E_L^{-1/3}$ . In a physical picture, this simply means that with increasing laser energy, a short acceleration duration with initially high electrical fields becomes more efficient than a longer effective acceleration duration with lower accelerating fields.

Yet, one has to be aware of the fact, that the model strongly simplifies the acceleration dynamics. However, as shown in Fig. 3.3 it can successfully be used to describe maximum energies and pulse duration dependencies and well describes the principle behavior of recent experimental findings. The demonstrated high proton acceleration performance of modern ultra-short pulse laser systems therefore justifies the quasi-static assumptions of the model. Investigating the time-scale of the acceleration process, this argumentation will be even further supported by the novel experimental findings on prominent non-normal proton beam emission induced by prompt prethermal electron acceleration along the oblique laser incidence direction, presented in the next section.

## 3.2. Prominent non-normal proton emission as diagnostic for an efficient intra-pulse acceleration phase

The ongoing development of ultra-short pulse high-intensity Ti:Sapphire based laser systems into the multi-PW range shifts the interest to the ultra-short time-scales of the acceleration process. The asymptotic behavior of the Schreiber model for ultra-short laser pulses changing into a near-linear scaling of the maximum proton energy with laser power for ultra-short acceleration times is a result of the picture that the particles never leave the vicinity of the finite source area. This immediately raises the question, whether the expansion of a thermalized hot electron Debye sheath during the laser pulse duration can lead to an efficient proton acceleration (refer to Sec. 3.1.1). Within typical ultra-short laser pulse durations of 30 fs the motion of relativistic electrons is restricted to only several micrometers and thus longitudinal recirculation, a significant transverse expansion or cooling can be neglected during the initial acceleration phase. The original hot electron distribution, strongly depending on the governing laser absorption mechanism and likely to be anisotropic and thus non-thermal in a three dimensional picture, will directly feed the accelerating field. In this section, it will be demonstrated for the ultra-short (pulse duration  $\sim 30$  fs) highly relativistic (intensity  $\sim 10^{21}$  W/cm<sup>2</sup>) laser pulses of Draco, that the ultra-short initial period, here called the intra-pulse phase, of the proton acceleration process becomes relevant. The experimental finding that an important part of the acceleration takes place before the plasma has time to evolve not only justifies the application of the theoretical models in the limit of quasi-static conditions in the first place, but also may explain the underlying physics leading to the surprisingly high proton acceleration performance achieved with ultra-short pulse laser systems in the recent years (around 20 MeV at Draco, or 40 MeV from J-Karen [124]). The core idea of the presented experiments and simulations to identify this prethermal intra-pulse phase of the acceleration is the observation of prominent non-target-normal emission of energetic protons reflecting an engineered asymmetry in the field distribution of promptly accelerated electrons by using oblique laser incidence on target and even more explicit by altering the spatio-temporal intensity envelope of the focused laser beam (see Sec. 3.2.2).

### 3.2.1. Non-target-normal proton beam emission using oblique laser incidence

In the proton acceleration experiment presented in Fig. 3.7 the ultra-short laser pulse (30 fs duration, peak intensity of about  $8 \cdot 10^{20}$  W/cm<sup>2</sup>) impinges under an angle of  $\delta=45^\circ$  onto a micrometer thick solid target. A detailed description of laser parameters, laser diagnostics, target preparation and diagnostics is given in Sec. 2.1 and Sec. 2.2. The energetic protons are recorded a few centimeters behind the foil using a radiochromic film (RCF) stack, from

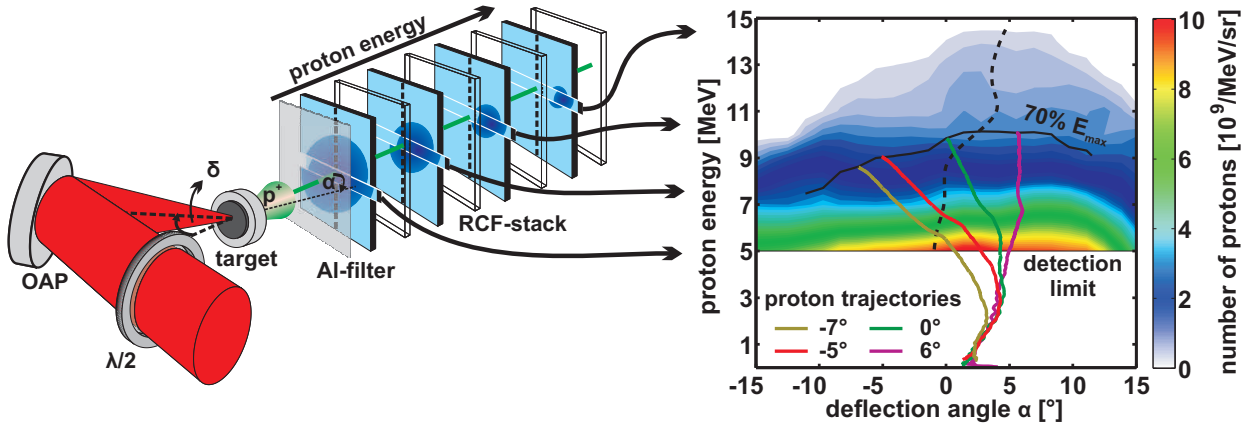


**Fig. 3.7.:** *Spatial energy distribution of laser-accelerated proton beams. The accelerating laser pulse is tightly focused by an off-axis parabolic mirror (OAP) under oblique incidence ( $\delta = 45^\circ$ ,  $p$ -polarization) onto a  $2\ \mu\text{m}$  thick titanium foil target and proton emission is recorded with stacks (about 15 layers) of radiochromic film (RCF). The reconstruction of the particle number per energy for horizontal slices yields the angularly resolved proton spectrum, where the dashed line represents the centroid of the angular distribution. Scaled trajectories for protons reaching 70% of the maximum energy at different final emission angles are added.*

which the spatial energy distribution can be reconstructed with large angle acceptance. To allow for online measurements of the proton deflection angle the scintillator stack detector (see Fig. 2.3) was used and a Thomson parabola was routinely applied as well to complement the maximum proton energy measurements. As shown by the spatial energy distribution of laser-accelerated proton beams shown right in Fig. 3.7, a deflection of the most energetic protons of about  $5^\circ$  from target-normal into the direction of the initial laser propagation axis is observed while lower energy protons exhibit a symmetric pattern with a larger divergence angle. In the following, this directed deflection of energetic protons will be correlated with the directed acceleration of hot electrons in the presence and thus on the time-scale of the ultra-short laser pulse.

For a time-resolved analysis of the interaction process the 2D3V particle in cell code PICLS [135, 136] was applied. Similar to the experimental conditions, the code was employed to simulate the interaction of a Gaussian shaped laser pulse with 30 fs duration and linear  $p$ -polarization with a solid target at an angle of incidence of  $45^\circ$ , as illustrated in Fig. 3.8. The target, a  $1\ \mu\text{m}$  thick titanium foil covered on both sides with a 30 nm thick layer of hydrogen and carbon atoms is located  $35\ \mu\text{m}$  from the starting edge of the simulation box. The focal spot size of  $5\ \mu\text{m}$  FWHM yields a peak intensity of  $10^{21}\text{W}/\text{cm}^2$ . The simulation box consists of  $19440 \times 8330$  cells with 55 cells per  $\lambda = 800\ \text{nm}$  and 2 ions per species and cell. The resulting electron density in the bulk is  $122n_c$  when fully ionized. Ionization and collisions are included in the simulation. For the realistic simulation of prepulse induced effects like the expansion of surface layers of the foil the measured temporal profile of the laser pulse was used starting at  $t = -3.5\ \text{ps}$  where the ionization threshold is reached.

Fig. 3.9 shows snapshots of simulated spatial energy distributions for electrons (upper

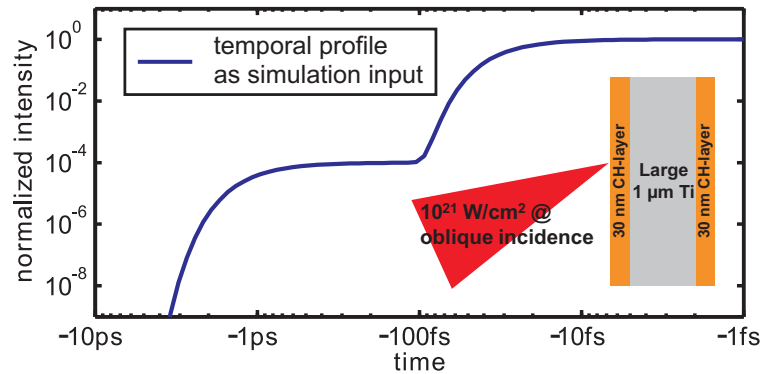


**Fig. 3.8.:** Setup of the 2D PICLS simulation of the experiment presented in Fig. 3.7. Laser and target configurations are illustrated. For the realistic simulation of prepulse induced effects the temporal pulse profile measured by third order autocorrelation is taken into account. Adapted to the trace of Fig. 2.2 the shoulder of the pulse contrast starting from 3 ps until the arrival of the main laser pulse at a level of  $10^{-4}$  is included in the simulation. Thus, all intensity contributions above the ionization threshold are included in the simulation.

row) and protons (lower row) plotted as a function of the emission angle for consecutive time steps. At  $t = 0$  fs the peak of the laser pulse reaches the target front surface. Electrons are ejected from the target rear along the direction of the incident laser beam ( $45^\circ$ ). The strong correlation of the electron distribution with the direction of the incoming laser light ( $45^\circ$ ) at this early (the intra-pulse) phase of the interaction is additionally visualized by the electric field component parallel to the surface ( $E_y$ ) exhibiting a strong asymmetry (bottom of Fig. 3.9). Already at  $t = 44$  fs ( $\sim 1.5\tau_L$ ) the initial asymmetry of spatial electron emission distribution and accordingly the asymmetry of  $E_y$  have almost vanished. In contrast to that, protons, starting immediately (refer to  $t = 22$  fs, laser is almost turned off) to gain energy by following the highest field gradients, conserve the initial deflection angle during the subsequent laminar and self-similar expansion of the sheath [4] that further drives the proton front (visible also in the  $E_x$  field map). In the corresponding field maps the proton momentum gain in non-target-normal direction is also indicated by inclusion of trajectories (black solid lines) of those protons that finally reach highest energies (above 90% of the maximum energy  $E_{>0.9}$ ).

This simulation illustrates how the intra-pulse dynamic of the promptly accelerated electrons translates into a signature that can be experimentally detected at any later time, the deflection of the angular proton spectrum. For the most energetic protons  $E_{>0.9}$  the green dashed line in Fig. 3.10 shows the increase of the deflection angle with time during the intra-pulse phase and its stagnation during the expansion phase. For a quantitative distinction of both phases, the increase of the maximum energy of protons propagating under sample angles of  $6^\circ$  (blue),  $-1^\circ$  (black) and  $-5^\circ$  (red), being related to the maximum field integral, is shown additionally. More precisely, sample angle means, that at each time step in the simulation the maximum proton energy of all protons being emitted at that particular angle, is determined. According to the resulting time evolution, in the intra-pulse phase and

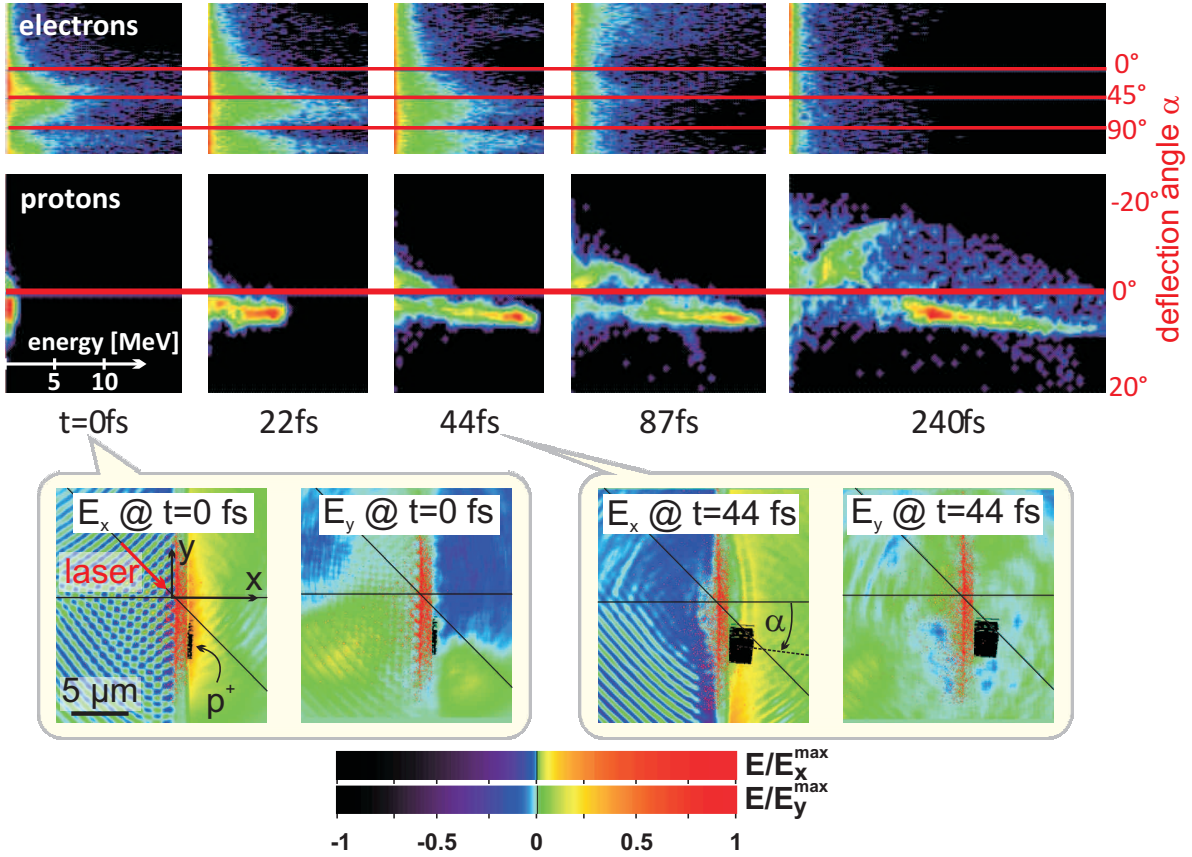


**Fig. 3.9.:** *Modelling of the intra-pulse acceleration dynamics. (Top) False colour coded images of simulated spatial energy distributions for electrons (upper row) and protons (lower row) plotted as a function of the emission angle  $\alpha$  for consecutive time steps. At  $t=0$  fs the peak of the laser pulse reaches the target front surface. The intensity of the images, corresponding to the number of particles, is logarithmically scaled and normalized to the individual maximum. The energy scale included in the first proton distribution is valid for all electron and proton images. The spectral modulations visible in the proton distribution can be attributed to multi-species effects. (Bottom row) The components of the spatial distribution of the electric field amplitude in target-normal direction ( $E_x$ ), and parallel to the target surfaces ( $E_y$ ) are plotted for  $t = 0$  and  $t = 44$  fs, respectively, with maximum field values of  $E_x = 4 \times 10^{13}$  V/m and  $E_y = 2 \times 10^{12}$  V/m. Trajectories of protons reaching more than 90% of the maximum energy ( $E_{>0.9}$ ) are overlaid in black.*

along the optimum angle of  $6^\circ$  the proton energy grows significantly faster than along other angles and than in the post-pulse phase. The initial angle-dependent disparity in energy is maintained throughout the later quasi-neutral expansion phase of the sheath. The major finding is that already at  $t \sim 2\tau_L$  about half of the final energy can be reached. It is likely that this fraction constitutes only a lower limit for the intra-pulse energy gain, as 2D PIC simulations at reduced density tend to underestimate the dilution of the sheath which is responsible for the post-pulse acceleration phase.

In order to further emphasize the relevance of the directed intra-pulse acceleration, averaged trajectories of protons reaching  $(0.6 - 0.8) E_{max}$  are overlaid with the experimental spectrum in Fig. 3.7. It turns out that these sample protons, finally observed under angles deviating from the optimum, gained significant energy under initially optimum angles



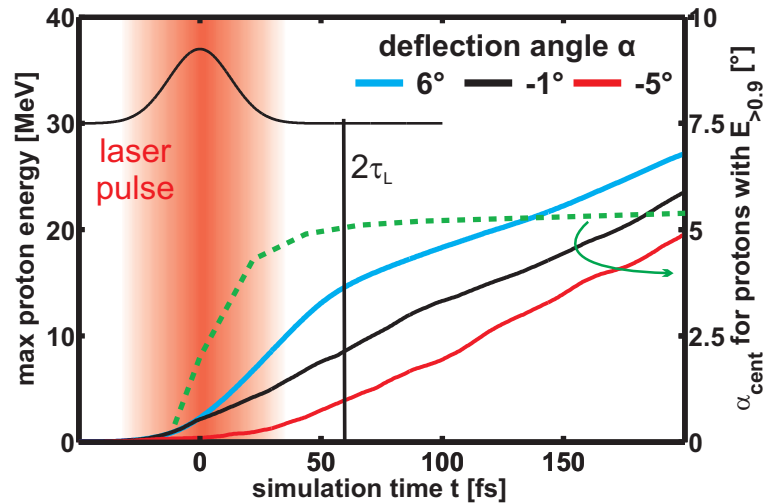


**Fig. 3.10.:** For protons reaching more than 90% of the maximum energy ( $E_{>0.9}$ ), the increase of the deflection angle  $\alpha_{\text{cent}}$  with time is shown in green together with the evolution of the maximum energy of protons emitted under sample angles  $\alpha$  of  $6^\circ$  (blue),  $-1^\circ$  (black) and  $-5^\circ$  (red). For illustration of the time-scale, the laser pulse profile is given by the red shaded region and the black gaussian shaped curve. For the duration of the laser pulse  $\tau_L$ , the asymmetry of the electron distribution translates into a non-target-normal emission of energetic protons that can be detected experimentally.

( $\alpha > 0$ ) and only later got deflected due to variations in the lateral position in the expanding plasma sheath. Summarizing so far, the detection of prominent non-target-normal emission of energetic protons may serve as a diagnostic for an efficient intra-pulse acceleration. In the following this phase of the acceleration process is called prethermal as it precedes the thermal expansion of the plasma sheath.

It has to be mentioned here, that the main conclusion of the observed non-normal emission of the energetic protons being a clear signature of the intra-pulse acceleration dynamics has so far only been drawn by the study of the time and space resolved dynamics of the interaction process on the scale of the pulse parameters in a PIC simulation. A direct measurement of the electron dynamics would clearly be beneficial. Different methods such as the measurement of coherent transition radiation or X-ray emission in principle could help to monitor aspects of the hot electron population. However, the actual task requires an intra-pulse time resolution of only tens of femtoseconds and micrometer spatial resolution for the megaelectronvolt electron population at the target surfaces during the interaction. Such measurements are technically very challenging and have never been established before. In order to give more detailed insights into the intra-pulse acceleration process and to further support the link between experiment and simulation, several independent but indirect experiments were performed and related to the intra-pulse acceleration phase, as presented in the next sections.

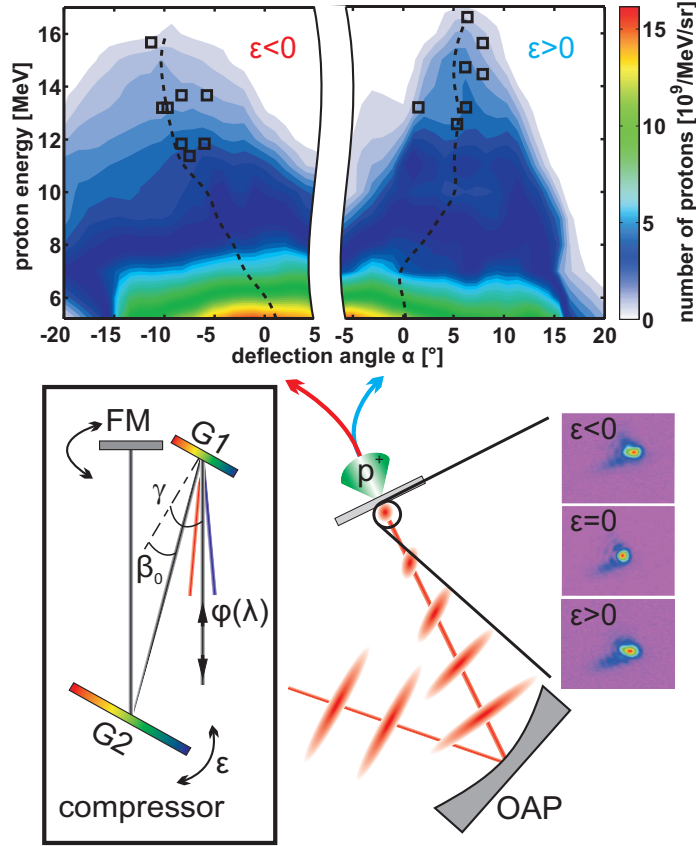


**Fig. 3.11.:** Setup of the test experiment based on a change of sign in the designed pulse front tilt. Bottom left: Grating compressor with gratings G1 and G2 (slightly tilted by angle  $\varepsilon$ ) and folding mirror FM. The tilted intensity envelope is focused by the OAP under normal incidence onto a  $2\mu\text{m}$  thick Ti foil target. Bottom right: Horizontally enlarged focal spots showing spatial chirp in the focal plane, see also Fig. 3.15. Top: Two samples of reconstructed angular proton spectra are shown for  $\varepsilon > 0$  and  $\varepsilon < 0$ . Black squares represent the scattering of the deflection angle of the most energetic protons for the full series of shots. The dashed line follows the centroid of the angular distribution.

### 3.2.2. Proton beam steering by an engineered laser pulse front tilt

An expanding sheath can inherit geometrical properties of the target rear surface such as, e.g., deformations caused by nanosecond prepulse driven hydrodynamic shocks [112, 137, 19] (see also Sec. 3.2.4). Thus, in order to unambiguously demonstrate the relevance of the intra-pulse acceleration phase, a test experiment only relying on properties of the ultra-short laser pulse itself has been designed. The basic idea of this test experiment is the introduction of a small angular chirp (AC), immediately yielding a pulse front tilt (PFT) of the ultra-short laser pulse [138]. It has recently been shown [139] that a small PFT directly influences the pointing of electrons accelerated in an underdense plasma. Here, the PFT is used to generate a spatio-temporal asymmetry in the laser-plasma interaction that is restricted to the coherent ultra-short pulse. It does not apply to the incoherent nanosecond prepulse level originating from amplified spontaneous emission (for discussion of the influence of coherent prepulses, see Sec. 3.2.4).

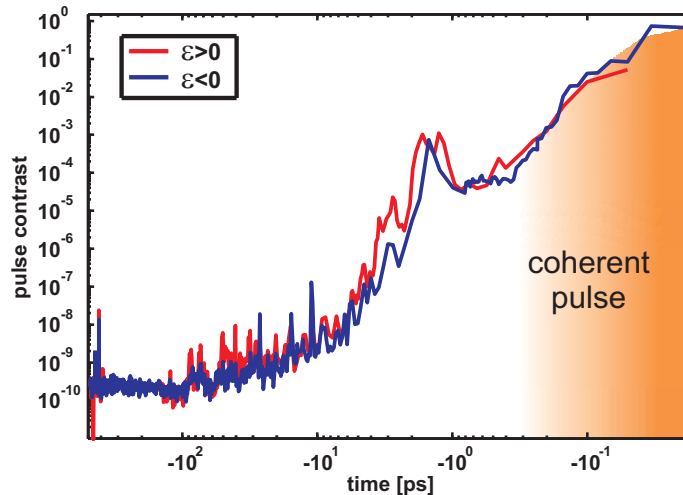


**Fig. 3.12.:** Temporal contrast curves for corresponding configuration of  $\varepsilon$ .

In the test experiment, sketched in Fig. 3.11, the foil is irradiated under normal incidence. The small angular chirp (AC) is introduced by a slight rotation of one of the compressor gratings around the axis parallel to its grooves by  $\varepsilon = \pm 0.03^\circ$ . Pointing is corrected by turning the folding mirror accordingly. Potential changes in the group delay dispersion are compensated for by the usual optimization procedures for grating distance and spectral phase control loops (c.f. chapter 2). Changes in the pulse contrast are ruled out by third-order autocorrelation measurements (see Fig. 3.12). Since various laser wavelength components exhibit different incident angles on the focusing optics, the AC further causes a spatial chirp (SC) in the focal plane, which leads to the oval focal spot in Fig. 3.11 confirming the setting. This is discussed in detail further below.

The energy resolved proton emission pattern was recorded with RCF stacks and stacked scintillators with CCD online readout for two opposite AC settings. Proton spectra reconstructed from exemplarily chosen stacks are displayed in Fig. 3.11. As in the previous experiment at oblique laser incidence, the highest proton energies are observed under angles of up to  $10^\circ$ . Clearly, the sign of the deflection from target-normal only depends on the orientation of the PFT, a quantity linked to the main pulse and therefore independent from prepulse induced target deformations. This observation confirms that protons are significantly accelerated in the intra-pulse phase of ultra-short pulse lasers, and, additionally, provides a novel method for active fine-steering of the energetic proton bunch.

Although the interpretation of the test experiment seems to be straight forward and already the presence of the spatio-temporal asymmetry initially caused by the AC in the compressor explains the experimental observation, a deeper understanding of the laser-plasma interaction process when applying phase-distorted pulses is of course desirable. In appendix A, the formation of the spatio-temporal distortions during pulse propagation and the consequences of the beam focusing will be discussed and illustrated by an analytic wave-optical treatment based on basic Fourier transformation. Confirming the intuitive assumption, there

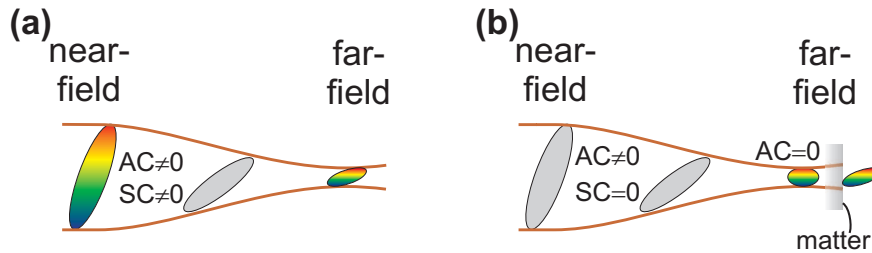


**Fig. 3.13.:** Schematic illustration of the possible origin of pulse front tilt occurring in the laser-plasma interaction. (a) Laser pulse is spatially chirped before focusing, that couples to angular chirp and therefore PFT at the focal plane immediately. (b) The focused pulse with a spatial chirp propagates through matter (e.g. preplasma) and group delay dispersion occurs and causes PFT.

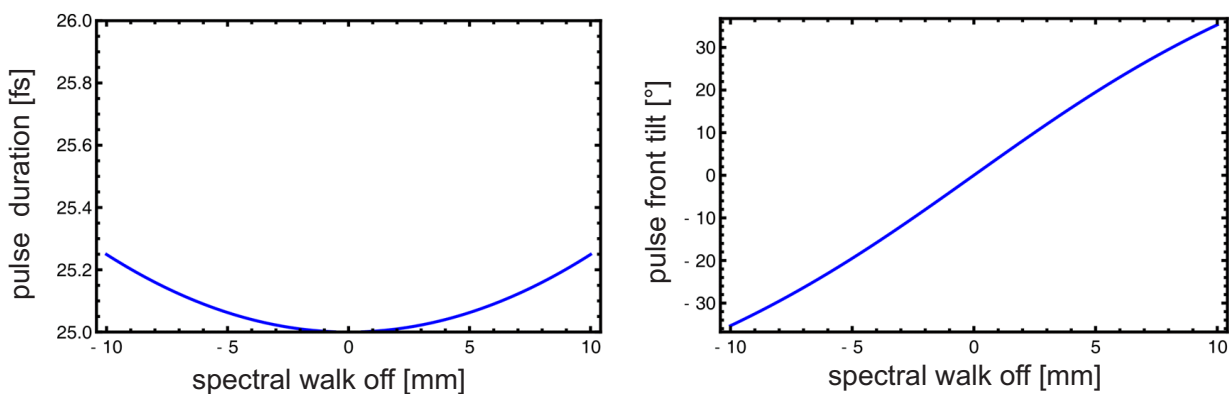


**Fig. 3.14.:** Influence of residual SC (spectral walk-off) in the beam on pulse duration and PFT in the focus, calculated for parameters closely resembling the experiment in Fig. 3.7 using the Kostenbauder matrix formalism [140, 141].

it is analytically shown that an AC in the near field of a laser beam translates into a spatial chirp (SC) when the laser beam is focused in the focal plane (far field) leading to a reduction of the focal intensity (see below). Vice versa, the presence of residual spatial chirp in the unfocused beam (near field), e.g. caused by Brewster windows in the laser chain or long distance propagation of angularly chirped pulses, leads to an AC and therefore immediately to a PFT in the focus directly, as sketched in Fig. 3.13(a). The influence of residual spatial chirp on PFT and pulse duration is depicted in Fig. 3.14 for experimental input parameters. While spatial chirp can induce a large PFT in the focus, the pulse duration (near field) stays almost unaffected.

According to exact calculations (c.f. [139]) without spatial chirp, the PFT of the beam increases when approaching the focus and completely vanishes within the Rayleigh length. In that case, a PFT in the focus could still be generated by interaction with matter (e.g. preplasma), due to the group velocity dispersion in the medium (see Fig. 3.13(b)). However, a significant contribution is only expected for a long propagation length (c.f. simulation in Ref. [139]) and therefore unlikely to occur for short plasma scale lengths as shown in Fig. 3.16 for the experimental parameters at Draco.

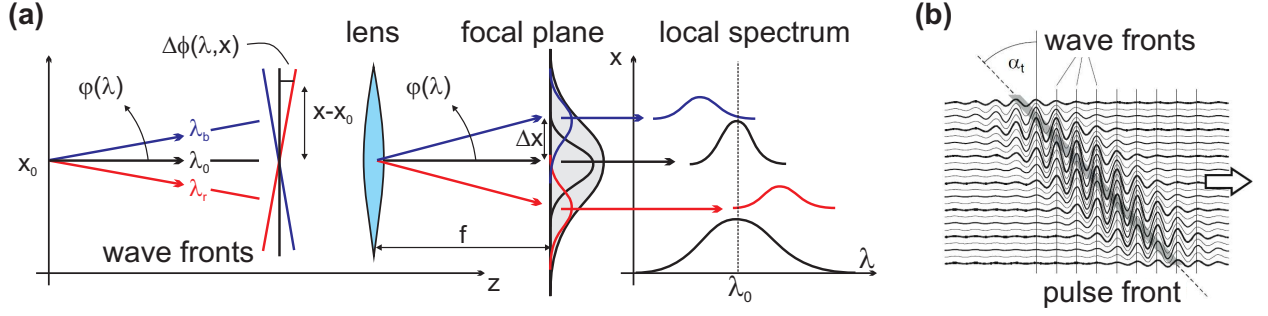


**Fig. 3.15.:** (a) Illustration of angular chirp formation (corresponding to the case depicted in Fig. 3.13(b)). Different spectral components travel at different angles  $\varphi(\lambda)$  and generate a spatial and spectral phase shift. Focusing an angularly chirped pulse yields a spectral decomposition at the focal plane and therefore leads to focal spot enlargement and elongation of the laser pulse duration due to a reduced local bandwidth. (b) Sketch of a pulse with a tilted pulse front caused by an angular chirp. While the wave fronts propagate perpendicular to the propagation direction, the pulse envelope is tilted by an angle  $\alpha_t$ . Principle of sketches extracted from Ref. [142].

In order to further illustrate the picture of PFT and to derive experimental quantities, in the following a geometrical analysis is used that was introduced by Pretzler *et al.* [55]. For convenience, the AC of the pulse propagating in  $z$  direction ( $xz$  plane, see Fig. 3.15) is defined as function of the wavelength

$$AC_\lambda = \left. \frac{\partial \varphi}{\partial \lambda} \right|_{\lambda=\lambda_0} \quad (3.30)$$

with index 0 standing for the central spectral and spatial component always.

According to the experiments discussed in the previous section, the AC is caused by a small misalignment of the two compressor gratings from exact parallelism. Hereby, only a small tilt in the horizontal beam axis ( $xz$ -plane) by an angle  $\varepsilon$  is considered, while an angular chirp may also be a result of a remaining vertical tilt or a not exactly matching groove orientation of the gratings. Given the incidence angle  $\gamma = 29.2^\circ$  of the laser onto the first grating, the diffraction angle  $\beta_0 = 44.12^\circ$  and the groove spacing  $s = 676$  nm (for angle definition refer to Fig. 3.11) the angular chirp in the horizontal beam axis

$$AC_\lambda = \left| 2\varepsilon \frac{\tan \beta_0}{s \cos \gamma} \right| \quad (3.31)$$

can be calculated [55]. In the test experiment presented above, the compressor grating was tilted by  $\varepsilon = \pm 0.03^\circ$  yielding an angular chirp of  $AC_\lambda = 1.7 \mu\text{rad}/\text{nm}$ . This value has been verified using an interferometric field autocorrelator with spatial inversion [55, 143].

Ignoring spatial dispersion and temporal dispersion, the AC can be interpreted as a small tilt of the virtual phase fronts of the single spectral component of the pulse. A spectral phase

shift can therefore be introduced ([55, 142], see Fig. 3.15)

$$\Delta\phi(\lambda, x) = \frac{2\pi c}{\lambda} \frac{\Delta z}{c} = \frac{2\pi}{\lambda} \Delta x \tan \varphi(\lambda) \approx \frac{2\pi}{\lambda} \varphi(\lambda)(x - x_0) \quad (3.32)$$

which leads to an  $x$ -dependent component of the linear phase chirp

$$\left. \frac{d\phi(x)}{d\lambda} \right|_{\lambda=\lambda_0} = \frac{2\pi}{\lambda_0} AC_\lambda(x - x_0). \quad (3.33)$$

Using  $d\omega/d\lambda = -2\pi/\lambda^2$ , a group delay component  $\Delta\tau_g$  can be introduced

$$\Delta\tau_g = \left. \frac{d\phi(x)}{d\omega} \right|_{\omega=\omega_0} = \frac{\lambda_0}{c} AC_\lambda(x_0 - x) \quad (3.34)$$

and consequently the pulse front of the propagating laser pulse is tilted with respect to the phase fronts by the angle (c.f. (A.2) for the definition of  $p$ )

$$\tan \alpha_t = \frac{c\Delta\tau_g}{x - x_0} \Rightarrow |\alpha_t| \approx \lambda_0 AC_\lambda = p. \quad (3.35)$$

In the near field this has no significant consequences for the local pulse duration which remains short at any point on the beam cross section. The spatial beam profile and also the wave fronts and therefore the propagation properties of the beam stay unchanged in a first approximation. However, the intensity of the pulse can be significantly reduced when concentrating all spatial parts of the pulse in the focus. This is a consequence of the spectral decomposition of an angularly chirped pulse being tightly focused. In fact, this yields two complementary effects as illustrated in Fig. 3.15. First, the spectral components of the pulse are focused next to each other yielding an enlargement of the focal spot in the according direction (c.f. (A.17)) and second, this leads to a reduction of the spectral width at each point and therefore to a local increase of the pulse duration. Following an analytical approach using Gaussian shaped spectral and spatial intensity profiles [55] the focal spot  $\sigma$  and pulse duration  $\tau$  are both increased by the same factor

$$\xi = \frac{\Delta\tau}{\Delta\tau_0} = \frac{\sigma}{\sigma_0} \Rightarrow I = \frac{I_0}{\xi^2}. \quad (3.36)$$

An analysis of the focal spot images in Fig. 3.11 yields an increase of the focal spot size in  $x$ -direction by  $\xi = 1.5$  which would yield an intensity reduction by about a factor of 2. In the test experiments, however, the proton acceleration performance was not influenced when introducing a small angular chirp being a result of several possible reasons. Following the discussion in appendix A concerning the coupling of the different spatio-temporal distortions, the investigation of the exact spatio-temporal configuration of the laser pulse at the interaction point is very challenging. A deeper analysis of the interaction dynamics thus deserves further precise measurements of laser parameters such as the spatial chirp at the position of the focusing optics, or the spectral phase across the full beam profile (in

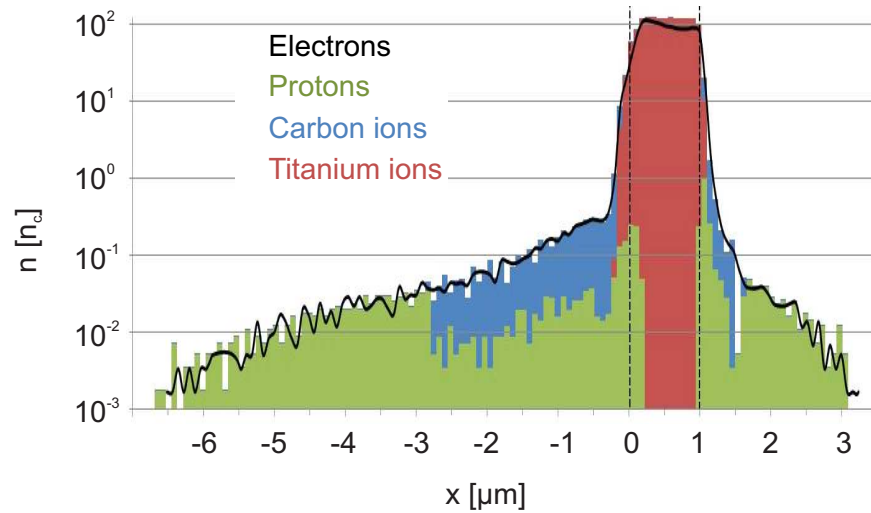


**Fig. 3.16.:** *Snapshot of simulated plasma density distribution (in units of the critical density  $n_c$ ) for electrons, proton and carbon ions as well as titanium ions, at 80 fs before the intensity peak of the main pulse reaches the foil (see Fig. 3.8, [20, 115]). Originating from the surface of a  $1\mu\text{m}$  thick titanium foil protons on the front illuminated side are leaking out into the vacuum for up to  $6\mu\text{m}$ . Thus, the main pulse interacts with underdense plasma for several micrometers before reaching the Ti-foil. The back side slope is steeper and protons can be found up to  $2\mu\text{m}$  behind the foil. The critical density surface has moved by a few hundred nanometers (both directions).*

progress). Furthermore, eq. (3.36) holds only true for Gaussian shaped spectral and spatial beam profiles and has to be adapted for flat top shaped profiles as were used in the experiment. Finally, the pulse elongation may be beneficial for the TNSA acceleration process and therefore may partially compensate for the negative effect of the focal spot enlargement. Especially these issues, the scaling of the proton beam deflection with pulse duration and the exact characterization of the spatio-temporal distribution of the focused laser pulse have to be addressed in future experiments.

### 3.2.3. Effect of laser incidence angle, polarization, pulse energy and pulse contrast onto the maximum proton energy

The given interpretation of both experiments reported in the previous sections 3.2.1 and 3.2.2 further relies on the assumption that laser energy is converted into hot electrons in a directed way as introduced in the set of simulated snapshots of spatial electron and proton energy distributions for the time steps of interest in Fig. 3.9. Complementary, a realistic simulation of a prepulse induced preplasma density distribution at 80 fs before the peak of the main pulse reaches the target is shown in Fig. 3.16. As discussed with the simulation parameters in Fig. 3.8 this simulation included all intensity contributions above the ionization threshold as deduced from a measured autocorrelator trace (Fig. 2.2). Thus, the main pulse interacts with underdense plasma for several microns before reaching the surface of the titanium foil. Directed laser light absorption into promptly accelerated electrons in the presence of a small

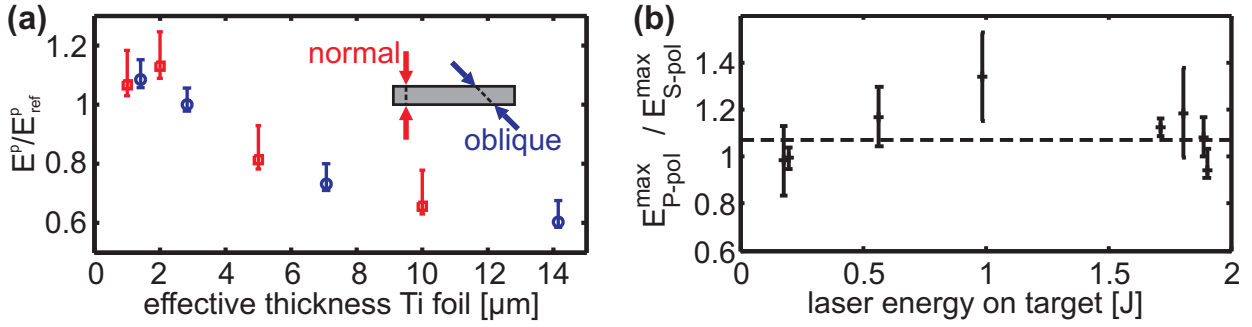


**Fig. 3.17.:** (a) Relative maximum proton energies for different angles of incidence as a function of the effective foil thickness. Shots under oblique incidence are plotted at  $d_{eff} = \sqrt{2}d_{foil}$ . Maximum proton energies are normalized to those obtained for a reproducible reference configuration ( $2\mu\text{m}$  thick titanium foil at  $\delta=45^\circ$ , p-polarization). Measurements were performed with RCF stacks. (b) Thomson parabola measurements of the maximum proton energy obtained using p-polarization normalized to that obtained with s-polarization for different laser energies on target. Different length of error bars is due to statistics.

scale length preplasma can be expected for the  $\mathbf{v} \times \mathbf{B}$  force dominated absorption mechanism, and is consistent with observations of earlier experiments measuring the angular electron distribution directly [144] or detecting Cerenkov or coherent transition radiation at the target rear side [145, 146, 147]. In particular the use of relativistic laser intensities dramatically alters the dynamics, because it is voiding the contribution of the Brunel heating mechanism [96] which only deals with non-relativistic acceleration by transverse electric fields (see Sec. 3.1.2), and therefore would accelerate electrons predominantly in laser normal direction and not along the laser direction as visible in the PIC simulation results (c.f. Fig. 3.9). The strong  $\mathbf{v} \times \mathbf{B}$  force contribution is furthermore supported by the occurrence of electron bunches at twice the laser frequency  $\omega_L$  observed in the PIC simulation as a clear and typical signature of  $\mathbf{v} \times \mathbf{B}$  heating and simultaneously opposing the Brunel effect.

The  $\mathbf{v} \times \mathbf{B}$  absorption as prevalent mechanism further implies that the performance of the proton acceleration process is mostly independent of the angle of incidence of the laser beam on the foil and of the orientation of its linear polarization. The opposite configuration, low laser intensity and extreme pulse contrast where the Brunel heating mechanism is dominant was already investigated by Ceccotti *et al.* [113] and accordingly yielded significant differences of the proton acceleration performance with respect to laser polarization and angle of incidence.

Relative maximum proton energies are presented in Fig. 3.17(a) for different angles of incidence as a function of the effective target thickness  $d_{eff}$  ( $d_{eff} = d_{foil}$  for  $\delta=0^\circ$  and  $d_{eff} = \sqrt{2}d_{foil}$  for  $\delta=45^\circ$ ) for the interaction conditions at Draco. The decrease in intensity by  $\sqrt{2}$  for the case of  $\delta=45^\circ$  has been taken into account by the proper choice of the laser energy for the normalization shots. In conclusion, the target thickness scan reveals no dependence on the angle of incidence, which compares well with recent results [148]. Independently, the laser polarization was varied with a thin half-wave plate close to the focusing optics (see Fig. 3.7). Apart from a slight enhancement of about 10% for p-polarization with respect



to s-polarization under oblique incidence no dependence of the proton acceleration on laser polarization orientation was observed as shown in Fig. 3.17(b). Both findings support the  $\mathbf{v} \times \mathbf{B}$  force dominated laser light absorption and therefore confirms the assumption that the laser incidence angle translates into the direction of the promptly accelerated electrons.

Still one can argue, that the realistic preplasma and therefore absorption conditions on target front and rear side, are not exactly known. Also the assumption that the real preplasma corresponds to the simulated density profile depicted in Fig. 3.16, and thus is only induced by the intense pedestal of picoseconds duration, can hardly be validated in the experiment. Hot electron Debye sheath expansion induced by the intense main pulse was measured with optical probing [149, 150] and by help of proton radiography [6]. However, a measurement of the sub-micron plasma expansion near the critical density surface at the front, and especially at the target rear surface as predicted by the PIC simulations for low intensity prepulses only a few picoseconds prior to the main pulse, is more challenging. There, measurement of spectral target reflectivity [151] or of the specularity [152] of the reflected light can provide indications of the preplasma conditions and therefore allow to qualitatively conclude on realistic laser pulse contrast conditions on target.

Yet, the most effective technique to study preplasma effects is the investigation of the ion, mainly proton acceleration performance as function of a tailored preplasma scale length, by truncation of the ASE pedestal of the laser pulse using pockels cells or plasma mirrors [82, 113], or by introducing additional prepulses [153, 84, 154, 83, 155, 37]. When an ASE-pedestal arrives at the target and is sufficiently intense to cause ionization of the illuminated surface, the target is heated by collisional absorption processes, as mentioned in Sec. 3.1.2. Provided the target is thin enough, the target rear surface is also affected. Additionally, the cold ablation plasma at the front surface can launch shock waves that then propagate through the target and alter the target rear surface [112]. In all cases, optimal proton acceleration within TNSA requires both, optimal laser absorption on the target front side and a steep density gradient and therefore optimal charge separation fields at the target rear [156, 157, 158]. This has been confirmed in many experiments varying laser pulse contrast and target thickness [82, 113] or by introducing additional prepulses [37, 83, 155] and studying the influence on the maximum proton energy. Active tailoring of the rear side preplasma scale length clearly revealed the high sensitivity of the TNSA process on the rear side condition [153, 84, 154].

ASE forms a pedestal that may extend several nanoseconds before the arrival of the main pulse, whereas the intensity level as well as the duration of the pedestal are relevant for the amount of preplasma to be formed (see also next section). Additionally, short pulse prepulses may occur, stemming from incomplete pulse re-compression namely higher order phase distortions or spectral clipping. At Draco, pulse compression is accompanied by active phase precompensation with a DAZZLER in combination with a measurement of the spectral phase using a SPIDER, refer to Sec. 2.1. Due to the relatively low spectral dynamic range of the SPIDER diagnostic, the phase contribution corresponding to the edge of the pulse

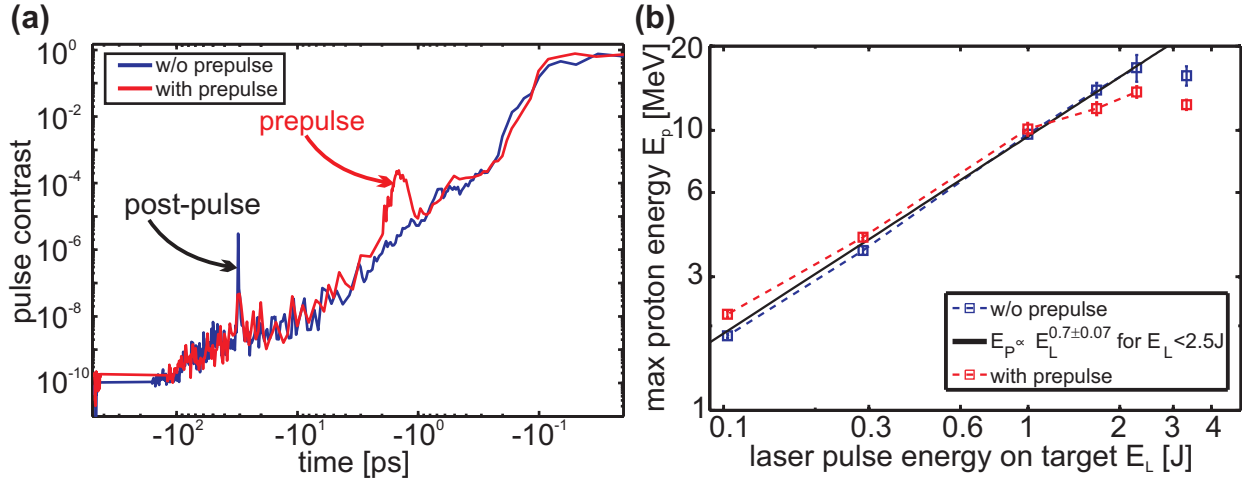


**Fig. 3.18.:** (a) Temporal laser pulse contrast as measured with a 3rd order autocorrelator for the different configurations of the active spectral phase precompensation. Setting with phase compensation corresponds to the red curve with additional prepulse, without phase compensation yields the blue curve (see main text). The prepulse artefact at  $-30$  ps corresponds to a postpulse, caused at the second saturable absorber. (b) Maximum proton energy  $E_p$  as function of the laser pulse energy  $E_L$  for the two prepulse configurations in (a). Experimental parameters ( $2 \mu\text{m}$  Ti foil,  $45^\circ$  incidence angle, p-polarization) are identical to those in Fig. 3.7. The data points obtained without prepulse (blue) are fitted by exclusion of the data point at  $E_L = 3.4$  J (see main text for details).

spectrum cannot be corrected for and even additional errors can be introduced. As shown in Fig. 3.18(a) this causes the small bump in the red contrast curve at about 2 ps prior to the main pulse. Removing the DAZZLER correction, the bump disappears but the rest of the curve remains identical (blue curve in Fig. 3.18(a)). Note that without phase correction the pulse duration is slightly increased to about 40 fs. The effect of this pulse duration change on the proton energy had been qualitatively found to be small in another run by varying the grating distance in the compressor and thus introducing a temporal dispersion. This is also in good agreement with data obtained on a similar laser system [159]. However, a change of the grating position normally requires a new phase correction loop with the DAZZLER making it difficult to clearly separate between effects of pulse duration and pulse contrast. Systematic investigations on that topic are still ongoing, whereas the dynamic range of the spectral phase measurement can be significantly improved using a WIZZLER (Fastlite).

For both contrast configurations in Fig. 3.18(a), the maximum proton energy as function of the laser energy  $E_L$  was measured and displayed in Fig. 3.18(b). The target and laser parameters were identical with those used in Fig. 3.7 ( $2 \mu\text{m}$  Ti foil,  $45^\circ$  incidence angle, p-polarization). The maximum proton energy was measured with the Thomson parabola, whereas for each laser energy configuration the target rotation was optimized to compensate for the proton beam deflection (Sec. 3.2.1) and the optimal focal position was cross-checked to exclude potential small distortions in the corrected wavefront when pump lasers in the last amplifier were switched on or off.

As expected from the discussion above, the curves in Fig. 3.18(b) behave differently. Note,

that the target thickness was initially optimized for the  $E_L = 2.3$  J configuration. Although only visible as a trend, at lower laser energy the small prepulse is beneficial and corresponds to better absorption. At higher energy the better contrast configuration yields higher maximum proton energy (black solid line). The decrease of the proton energy for the highest laser energy applied in this run remains unclear. Another experimental run, performed a few months later, revealed a possible explanation based on wave front distortion, and hence focusing problems due to thermal load in the Brewster windows of the vacuum chamber used for cryogenic cooling of the amplifier crystal in the last amplifier, once maximum pump energy is used (as it was the case for  $E_L = 3.4$  J). This is also the reason, why this point was omitted for fitting the maximum proton energy curve with  $E_p \propto E_L^{0.7 \pm 0.07}$ . The exponent of the fitting curve reveals better scaling than scaling with the square root of the laser energy and is in good agreement with the discussion in Sec. 3.1.3.

In summary, the experimental findings of Fig. 3.18 have two important implications. First, they confirm the initial conditions of the PIC simulation, because the intense but short prepulse preceding the main pulse only by a few picoseconds may indeed change the preplasma conditions on the target front side but, potentially, also on the target rear side. The achievable proton energy is given by the optimum between optimal absorption conditions and rear side gradient as suggested by the simulations (c.f. Fig. 3.16). The influence of ablation shocks induced target rear side expansion and thus worsening of the preplasma gradient can be neglected, as will be discussed in the next section. Second, these findings emphasize the challenge to experimentally investigate the proton energy scaling with laser intensity. As suspected, the proton acceleration performance is sensitive to small changes in the temporal pulse contrast, essentially in the picosecond rising edge of the main pulse. Therefore, the optimal conditions (laser pulse contrast or optimal target thickness) for each intensity configuration have to be ensured, calling not only for extreme pulse contrast but also for means to adjust it. This becomes certainly even more important when proceeding with higher laser intensity.

### 3.2.4. Alternative beam-steering by prepulse induced target pre-deformations

With regard to the test experiment using angularly chirped pulses to control the proton beam deflection in Sec. 3.2.2, it shall be mentioned that in addition to the main pulse, coherent prepulses on the picoseconds time-scale may also be affected by an angular chirp. Yet, their contribution to a shock-induced potentially asymmetric deformation of the target rear surface can be safely neglected for the given experimental conditions as will be briefly discussed in this section.

After the commissioning phase of the Draco laser first proton acceleration experiments were performed using oblique laser incidence on target, in 2009. The RCF images recorded of representative shots showed a systematic deviation of the emission angle of the most energetic

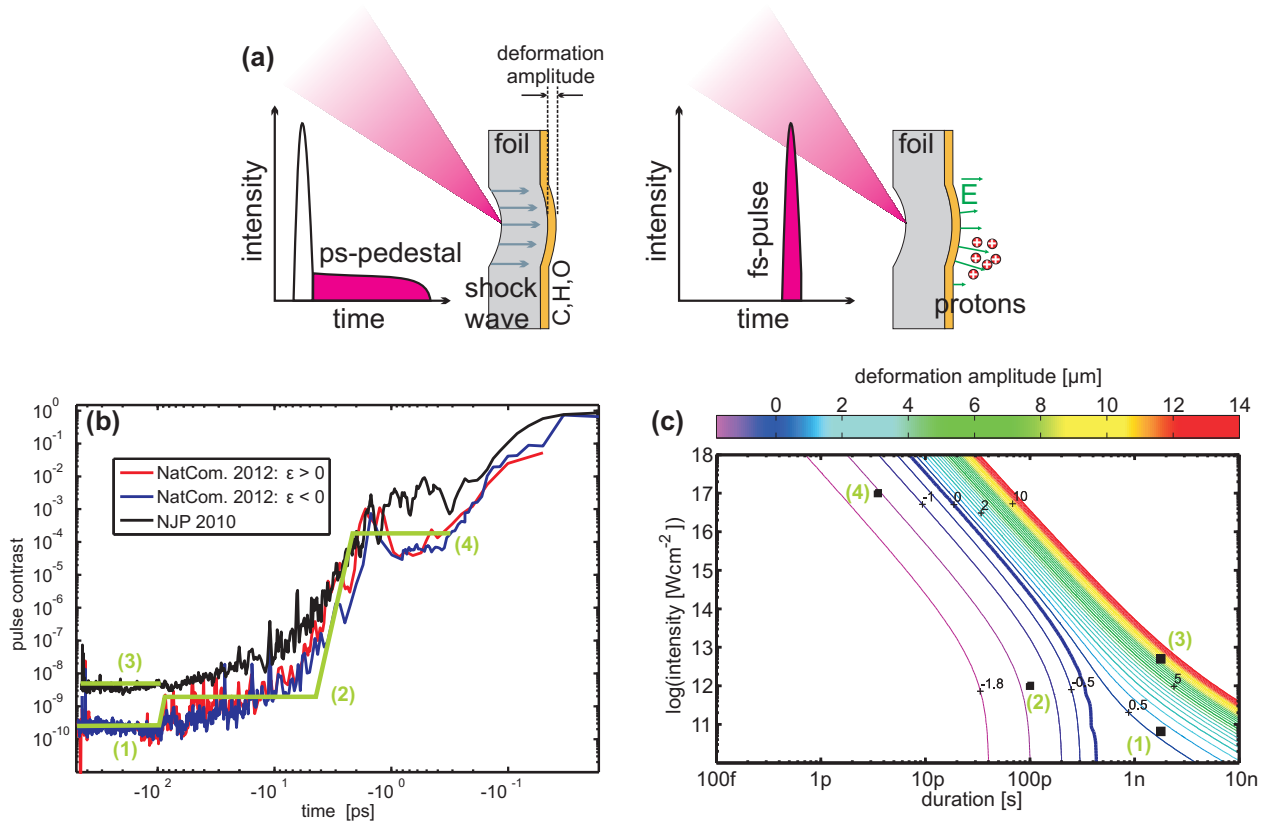


**Fig. 3.19.:** (a) Principle of the proton acceleration from a foil target after shock wave deformation. (b) Comparison of temporal contrast measured during the different experimental campaigns 2009 and end of 2010 and published in Ref. [19] and Ref. [20]. (c) Contour plot of the prepulse induced target deformation as function of prepulse intensity and prepulse duration, according to the model proposed in Ref. [112]. Thereby, the deformation amplitude as defined in (a) describes the deformation of the target rear surface, hence negative values imply that the shock wave has not even reached this surface. The black squares also indicated by the green numbers (1)-(4) correspond to the different configurations of ASE intensity level and duration marked in (b) accordingly.

protons with deflection angles of up to  $15^\circ$  from target-normal towards the direction given by the laser axis [19], very similar to the data presented in Fig. 3.7. However, the temporal pulse contrast at that time was different when compared to the experiment presented above, as it is shown in Fig. 3.19(b). Specifically, the intensity of amplified spontaneous emission (ASE) preceding the main pulse was in the order of  $5 \times 10^{12} \text{W/cm}^2$ , at comparable main pulse intensity this is almost two orders of magnitude higher than the more recent value. This level of prepulse intensity suggested an explanation of the proton beam deflection by prepulse induced target pre-deformation, schematically shown in the left part of Fig. 3.19(a). This scheme was first identified and discussed by the group at the Lund laser facility in 2005 [160, 112]. The nanosecond ASE pedestal of an ultra-short laser pulse with sufficient intensity ( $\approx 10^{12} \text{W/cm}^2$ ) can form a preplasma at the front surface of the target. As the preplasma expands into vacuum it launches a cold and plastic shock wave with a velocity in the order of  $\mu\text{m/ns}$ . The shock front breaks through the rear surface of the foil and results in a significant deformation (several  $\mu\text{m}$ ) of this surface. As long as the rear surface remains intact and the

ion density gradient remains steep, effective proton acceleration in the TNSA scheme occurs during the time the ultra-short laser pulse is interacting with the target foil. At higher ASE intensities the maximum proton energy can be reduced due to a longer plasma scale length [153, 82]. The deformed target geometry finally determines the emission direction of the energetic proton pulse. When the main laser pulse impinges on the front side of the curved target, electrons are asymmetrically distributed along the target rear surface (sketched in the right part of Fig. 3.19(a)). At the position where the laser hits the deformed target the highest field gradients are created. Hydrogen and heavier ions are completely field ionized and protons are accelerated to the highest energies. Protons originating from this area are steered toward the laser axis according to the local deformation. Since lower energetic protons stem from a larger region they experience on average less deflection.

In order to model the shape of the target deformation Lundh *et al.* [112] suggested a simple quasi-two-dimensional analytical model supported by hydrodynamic simulations for the characterization of the shock wave ballistics. The deformation amplitude depends on the velocity of the shock front  $v_s$  driving through the target and the deformation velocity  $v_d$  of the target rear surface after shock break through. From mass and momentum conservation,

$$v_s = \frac{c_s}{2} \left( \sqrt{1+x} + 1 \right) \quad \text{and} \quad v_d = \frac{c_s}{\kappa} \left( \sqrt{1+x} - 1 \right) \quad \text{with} \quad x = I^{2/3} \left( \frac{4\kappa}{\rho_0 c_s^2} \right) \quad (3.37)$$

are derived, where  $I$  is the ASE intensity of the laser,  $\rho_0$  the density,  $c_s$  the sound speed and  $\kappa$  a material specific parameter. For the experimental conditions of Draco ( $I = 5 \times 10^{12}$  W/cm<sup>2</sup>, Ti foil with  $\rho_0 = 4.53$  g/cm<sup>3</sup>,  $c_s = 5.24$   $\mu$ m/ns,  $\kappa = 1.02$  and  $d = 2$   $\mu$ m)  $v_s = 7.8$   $\mu$ m/ns and  $v_d = 5.7$   $\mu$ m/ns were chosen. For an estimated ASE duration of  $\tau_{ASE} = 1.8$  ns a maximum displacement of the target rear surface from its initial position of  $v_d(\tau_{ASE} - d/v_s) = 9$   $\mu$ m is obtained.

For a comparison of the results of the different experimental campaigns and to conclude on the influence of hydrodynamic shocks on the discussion of the intra-pulse acceleration phase, the different ASE prepulse intensity levels and their corresponding durations (indicated by the green numbers (1)-(4) in Fig. 3.19(b)) extracted from the measured 3rd order autocorrelation traces are plotted into the contour plot in Fig. 3.19(c) using constant target parameters (2  $\mu$ m Ti foils). Obviously, for such an extrapolation of the model by several orders of magnitude, the dependence between hydrodynamic pressure and the intensity of the laser pulse has to be roughly constant, as it is confirmed by hydrodynamic simulations published by Eidmann *et al.* [161] up to an laser intensity of about  $10^{16}$ W/cm<sup>2</sup>.

Regarding Fig. 3.19(c), it can be seen that the deformation amplitudes corresponding to the more recent contrast curves (red and blue line) are significantly smaller than the amplitude of 9  $\mu$ m that corresponds to the black trace and that was necessary to explain the proton beam deflection in Ref. [19]. The deformation amplitudes resulting from the red and the blue trace are too small as that they could lead to a significant deflection of the proton beam. Specifically, the very short (picoseconds) but very intense (as compared

to the very low ASE level) prepulse contributes to only a very small deformation of the target rear side of the order of a few hundred nanometer, that is also in full agreement with the 2DPIC simulation presented in Fig. 3.16 which fully considers the pedestal of interest starting 3 ps before the main pulse. The reason for this is that the expansion of laser induced hydrodynamic shocks scales stronger with time than with intensity see Fig. 3.19(c).

An effect that was not considered so far, is the influence of very small laser prepulse intensities even below the ionization threshold. In that parameter range (ASE intensities of  $10^8 - 10^9$  W/cm<sup>2</sup>) Wharton *et al.* [162] stated that the target is thermally vaporized and that the high intensity main pulse subsequently ionizes the expanded vapor plume giving rise to a preformed plasma. Such effects, however, should not contribute to target deformations and can be neglected in the presented analysis.

In conclusion, the original assumption to neglect prepulse induced target pre-deformation for the discussion of the intra-pulse acceleration phase is confirmed. Moreover the experiment with the introduced pulse front tilt in combination with the use of normal laser incidence on target clearly separates the different possible effects and the prepulse induced pre-deformation of the target may only have a small quantitative influence on the observed behavior.

### 3.3. Conclusion and outlook - Achieving proton energies relevant for therapy

As a main finding of this chapter, prominent non-target-normal emission of energetic protons, reflecting an engineered asymmetry in the field distribution of promptly accelerated electrons, was used to identify a prethermal phase of the acceleration of high energetic protons [20]. The strength of this novel diagnostic relies on the separation of prepulse and therefore preplasma effects from the interaction of the main pulse with the plasma. This allows for the investigation of the underlying time-scale of the laser-plasma interaction but also of the proton acceleration process and may trigger future development of even improved diagnostics schemes for ultra-fast processes in particular by tuning the laser pulse duration.

The experimental identification of the relevance of the intra-pulse acceleration phase for the energy gain of protons in laser-plasma acceleration provides important new insight into the understanding of TNSA in the ultra-short pulse regime. Whereas up to only recently, the quasi-self-similar expansion [3] of the electron sheath has been considered to be the most relevant process, for ultra-short and ultra-intense pulses the influence of the initial state of the isothermal expansion phase becomes important. As pointed out in Sec. 3.1.1, proton acceleration in the intra-pulse phase, when the Debye sheath is formed, is completely neglected by the plasma expansion model so far. Although the intra-pulse acceleration is of course included in PIC simulations and although the mechanism is in principle intuitively evident, the relevance of the prethermal phase for the complete acceleration process is demonstrated

for the first time in an experiment stressing the need to consider this phase in analytical models as well.

On the other hand, the strength of the quasi-static description of TNSA in predicting proton cut-off energies for a large variety of laser systems as well as the scaling behavior of the proton energy with laser power has been shown by measuring new proton energy values for the 150 TW ultra-short pulsed laser Draco and by collecting recent data from other groups, and relating them to the model by Schreiber. This in combination with the developed extrapolation of the approach to ultra-short pulse durations [19] implies, that the acceleration during the prethermal phase can well be described by quasi-static electric fields, in particular in the ultra-short pulse regime corresponding to short acceleration times. This is also the reason, why the consideration of the time limited fluid model by Mora *et al.* [3] in the limit of ultra-short laser pulses yields the same characteristic near-linear proton energy scaling, as demonstrated by Kluge *et al.* [117]. In fact, this is nothing different than to assume acceleration in the averaged static field conditions during the Debye sheath formation before the expansion starts. For increasing laser intensities, when the pulse duration, necessary to see near-linear behavior, decreases as well as the optimal acceleration time (see Sec. 3.1.3), a self-consistent time evolution treatment becomes essential and has to be included in the quasi-static approach.

The remaining question still is, what implications the novel regime has on the practical use of laser-driven proton accelerators for applications, such as radiation therapy, where a proton energy of more than 200 MeV is mandatory. It has been shown in Sec. 3.1.3 that the quasi-static near-linear intensity scaling, in principle should hold true for Draco laser pulse parameters (pulse duration, focusing etc.) up to the Petawatt level and thus proton energies of  $>100$  MeV could be in reach (see Fig. 3.20). In contrast to the far more demanding regime of radiation pressure acceleration of protons from ultra-thin linear density matched foils [29, 87, 39] exhibiting the same favorable near-linear intensity scaling, intra-pulse acceleration only requires micron thick metal targets and thus is very robust. Furthermore, prepared composition of source layers on the back of the foil could lead to well defined starting conditions of the acceleration and thus to monoenergetic features [80, 78]. With the use of two independent laser pulses, a staged approach based on an intra-pulse injector and a longer plasma post acceleration could improve the achievable energy and the control over laser-accelerated proton beams in the future. However, all these considerations are only justified as long as the laser contrast ratio does not become an issue, that means that the contrast needs to be adaptable to reach optimal conditions on target at any intensity. Furthermore, one has to be cautious with the robustness of the absorption mechanisms. As shown in Fig. 3.20 and discussed in Sec. 3.1.1, proton acceleration driven by an expanding plasma strongly depends on the exact hot electron temperature scaling and it is likely that the absorption efficiency applied in the quasi-static model and being an intensity dependent quantity has to be adapted as well, because it represents the same physical processes.

In practice, the question of the achievable proton energy can only be answered taking

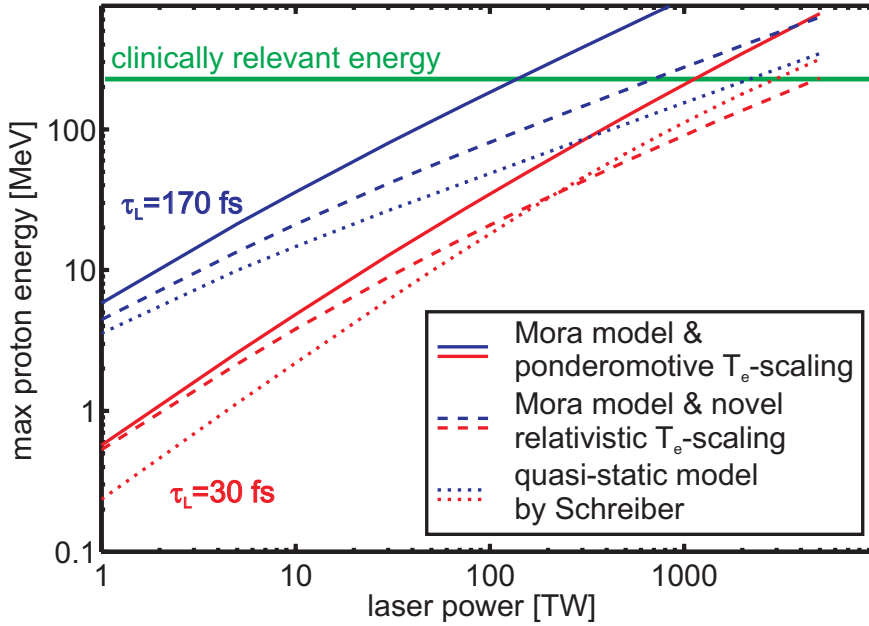


**Fig. 3.20.:** Comparison of proton energy scaling models discussed throughout this chapter and their extrapolation applying the interesting pulse durations 30 fs (red lines) and 170 fs (blue lines). Draco laser parameters  $r_L = 1.7 \mu\text{m}$ ,  $\lambda_L = 0.8 \mu\text{m}$ ,  $d = 2 \mu\text{m}$  and  $\vartheta = 10^\circ$  are used for  $\tau_L = 30 \text{ fs}$  (c.f. Fig. 3.3). For  $\tau_L = 170 \text{ fs}$ , apart from  $\lambda_L = 1 \mu\text{m}$  the same parameters are applied. In the Mora model different temperature scalings (see Sec. 3.1.2) are included, the ponderomotive scaling shown by the solid line (see equation (3.24)) and the implicit solution of the relativistic scaling in presence of a significant preplasma (dashed line) as given by eq. (11) of Ref. [117]. For the Schreiber model (dotted lines) refer to eq. (3.28). The green line corresponds to the proton energy relevant for radiation therapy.

also the progress of laser development and the technological feasibility into consideration. Applications always ask for high repetition rate as it has been shown by the systematic radiobiological studies [46, 47] in chapter 2. Although the table-top Ti:Sapphire based laser system cover this demand, the huge power consumption of the flash lamp pumped laser technology represents an important challenge for the transfer of this technology to commercial application. This issue is currently being addressed by the development of more energy efficient diode-pumped solid state lasers, such as the Polaris laser in Jena but also the Penelope laser at the HZDR. This type of high power laser exhibit longer pulse durations of about 150 fs. According to the scaling curves in Fig. 3.20 the proton acceleration performance at the power of a few Petawatt is predicted to be similar for both pulse duration regimes (30 fs and 170 fs). Which approach will thus be more sustainable, has to be answered in the near future.



## 4. Seeking the right target - The reduced mass target approach

An implementation of laser-driven proton accelerators for applications requires higher proton energies, sufficient proton yield, high beam optical quality and reproducible beam parameters. This is, last but not least, a question of applying the right laser target. Acceleration processes in the relativistic transparency regime [21, 23, 24] or the radiation pressure dominated scheme rely on ultra-thin targets [29, 30, 31]. Concerning the TNSA mechanism using micrometer thick targets, many different ideas of target manipulation have been proposed theoretically and tested in experiments. In order to increase the conversion of laser energy into energy of the plasma and thus to increase the achievable proton energy, special microstructured absorption layers at the target front side or foam targets [163, 164] can be applied. The generation of quasi-monoenergetic proton and ion spectra was demonstrated by restriction of the ion source to a small volume where the sheath field is homogeneous, transversely [78, 79] or by reduction of the source layer thickness [80]. Furthermore, three-dimensional shaping of the target geometry was successfully implemented to control the proton beam direction and divergence [165, 160] with curved foils or to increase the proton cut-off energy using conical shaped targets [85, 18, 86].

In the previous chapter the TNSA acceleration mechanism using in particular ultra-short laser pluses was explored with planar foils of titanium, that also yielded a robust reference target system (see chapter 2). In this chapter of the thesis the promising concept of using targets with reduced transverse size (so called reduced mass targets (RMT)) in order to improve the laser-proton acceleration performance is investigated.

As reported in Sec. 3.1, in TNSA protons gain their energy in the electric fields of a hot electron Debye sheath at the target rear which is generated by energetic electrons heated at the laser-illuminated target front surface and transported through the target. Thereby the longitudinal rarefaction of the plasma sheath as analytically described by the model in Sec. 3.1.1 but also the transverse dilution of the expanding hot electron Debye sheath with time limit the acceleration process. Ideally, the latter effect could be overcome by reducing the lateral target surface as illustrated in Fig. 4.1 assuming that the use of RMTs leads to confinement of the electron spreading and to recirculation of hot electrons in the sheath. The resulting increase of the hot electron density as well as of the hot electron temperature averaged over the effective sheath expansion time is supposed to provide higher accelerating fields for a longer time and thus enhance the final kinetic energy of the ions.

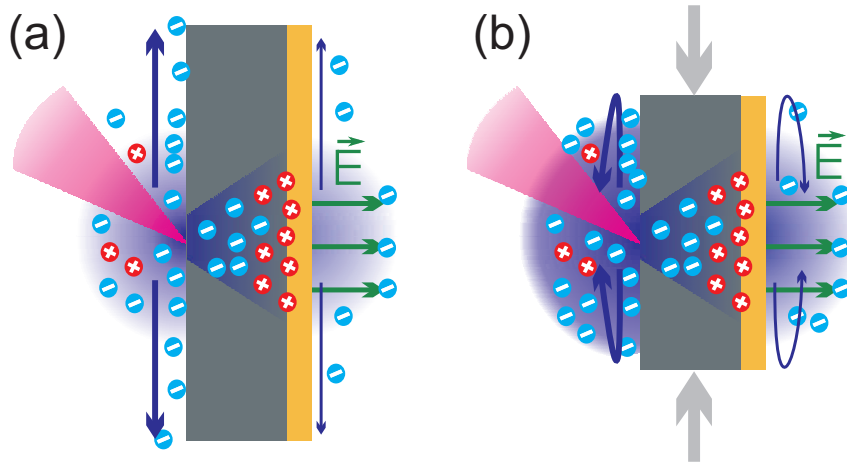


**Fig. 4.1.:** (a) Basic principle of TNSA (c.f. Fig. 1.1), here in particular illustrating the transverse dilution of the expanding plasma sheath. (b) By reducing the lateral target size (reduced mass target), sheath forming electrons are reflected at the target edges which yields an increase of electron density and hot electron temperature and hence of the accelerating fields. This potentially leads to higher maximum proton energy as well as higher proton yield.

Following theoretical proposals [110, 81, 166] various experimental studies were conducted to investigate the predicted increase of maximum ion energy and yield compared to large foil targets of the same thickness, using isolated spherical targets [167, 168, 169, 170] and metal foil sections [40, 171, 159] mounted on thin wires.

While spherical targets do not seem to increase the maximum proton energy and even perform worse than flat foils, the most promising results using RMT were obtained in a joint campaign at the 100 TW LULI laser facility reported by Buffechoux *et al.* [40]. As shown in the right part of Fig. 4.2, 2  $\mu\text{m}$  thick gold foil sections with transverse sizes between 3 mm and 30  $\mu\text{m}$  mounted on thin stalks of glass or carbon were irradiated with s-polarized pulses of 400 fs duration and an energy of  $\sim 7$  J focused onto a spot of  $\sim 6$   $\mu\text{m}$  (FWHM) yielding an intensity of about  $2 \times 10^{19} \text{W}/\text{cm}^2$ . By frequency doubling and filtering at  $\lambda_L = 529$  nm, the temporal contrast of the laser pulse was enhanced to reduce preplasma formation. For the optimum size the achieved maximum proton energy was increased almost by a factor of three (up to 14 MeV, see left plot in Fig. 4.2) as compared to flat foils. The observed effect is attributed to transverse hot electron refluxing during and shortly after the laser target interaction. This refluxing yields a time-averaged, denser, hotter, and more homogeneous electron sheath and therefore enhanced accelerating fields. However, with the same laser system (normal laser incidence) but without frequency doubling and therefore higher pulse intensity but lower contrast ratio, proton energies exceeding 20 MeV were achieved with large gold foils of 10  $\mu\text{m}$  thickness. This implies that the absolute gain in proton energy due to the RMT effect that is available for potential applications still needs to be evaluated. In addition, the role of the target thickness remained to be investigated in more detail.

Further enhancement of the initial hot electron temperature and thus the proton kinetic

energy due to a re-acceleration of electrons being reflected from the target edges and being re-injected several times into the focal region during the laser pulse duration was suggested in Ref. [81]. This special case requires the lateral target size to be small enough so that electrons have sufficient time to return back to the focal region during the pulse duration. In particular for the use of ultra-short pulses from Ti:Sapphire based systems as Draco ( $\tau$   $\propto$  tens of femtoseconds), targets with sizes down to the range of the focal spot size are necessary to observe these effects. However, the use of such a small target size may trigger further mechanisms like shock effects [169] or Coulomb explosion [81].

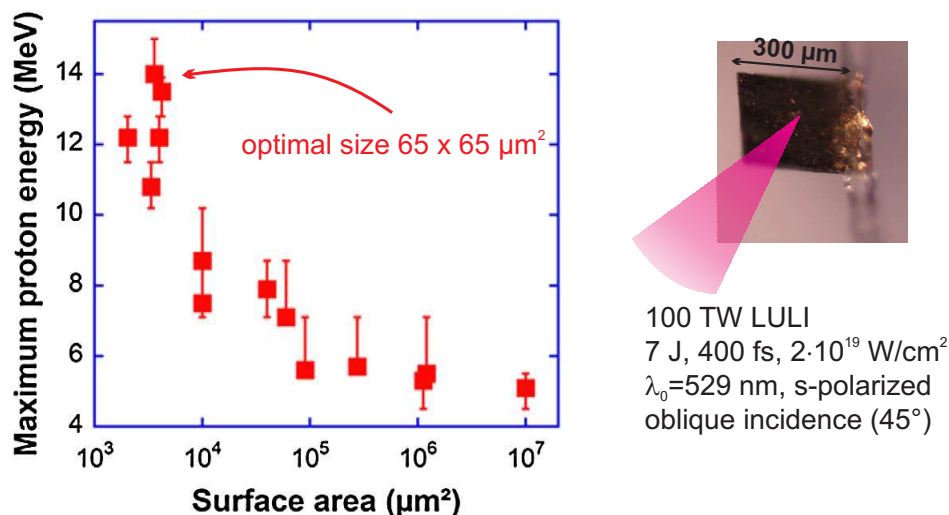


**Fig. 4.2.:** (Left) Maximum proton energy as function of target surface size, extracted from Ref. [40]. (Right) List of applied laser parameters and sample of target, 2  $\mu\text{m}$  thick foil section of gold mounted on a thin stalk. Frequency doubling was applied for contrast enhancement to reduce the influence of preformed plasma.

However, in all experimental studies so far the decrease of the target size down to the focal spot size (much smaller than targets used in Ref. [40]) did not result in the highest proton cut-off energies for given laser parameters. For the case of thin foil targets it is known that the presence of preplasma at the target rear side worsens the accelerating fields [82, 156, 172, 158, 157, 153, 126]. Considering isolated spherical targets, Sokolik *et al.* [167] developed a model based on hydrodynamic simulations estimating the drift of a prepulse-induced cold plasma corona around the target prior to the main pulse arrival. As a consequence the observed optimal target size is linked to a complex interplay between proton energy increase due to electron reflux by lateral target confinement and proton energy decrease, due to prepulse induced rear side preplasma generation.

In this chapter an experimental study is presented where gold disk targets 20 - 100  $\mu\text{m}$  in diameter and different thicknesses 100 - 1000 nm are irradiated with ultra-short laser pulses (30 fs) generated by the Draco system (c.f. Sec. 2.1). In particular, the experimental investigation of the target thickness dependence provides novel insights into the consequences of the transverse electron refluxing. Additionally, the influence of the microscopic target mounting is studied using a dedicated target design. The interpretation of the obtained

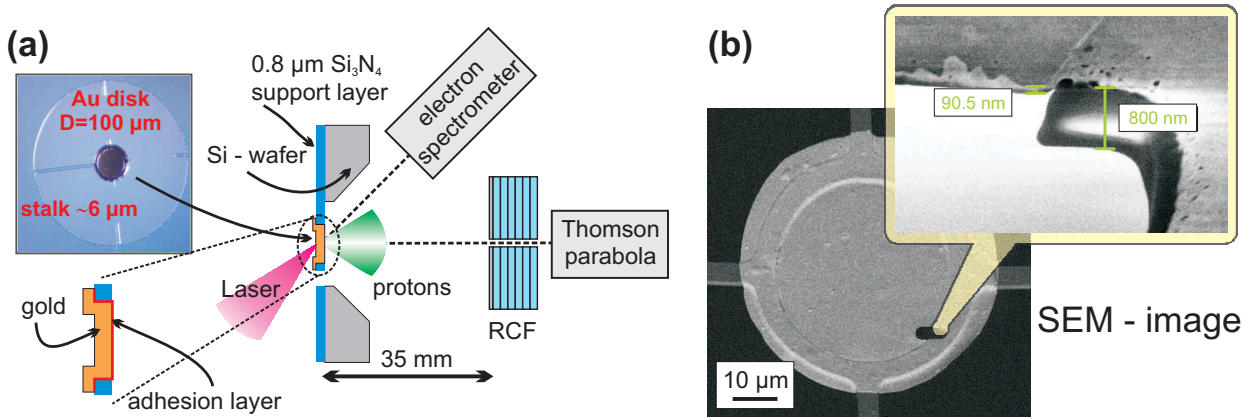


**Fig. 4.3.:** (a) Illustration of the basic experimental setup. The laser ( $\delta = 45^\circ$ ,  $p$ -polarization) is focused onto reduced mass targets (RMT) that are embedded in a structured wafer. The targets are small gold disks of different thicknesses and diameters (photograph left shows an example). The accelerated proton beam is detected using common RCF stacks and a Thomson parabola spectrometer. Electrons in laser direction are recorded with an additional magnetic spectrometer. (b) Scanning electron microscope images of a gold disk with a diameter of  $50 \mu\text{m}$  and a thickness of about  $100 \text{nm}$  measured at the edge of a hole that was drilled with an in-situ focused ion beam.

experimental results is supported by help of two-dimensional PIC simulations on the time-scale of several picoseconds with the focus on investigation of prepulse induced preplasma formation as function of the lateral target size.

## 4.1. Experimental setup

The experiments were performed using the 150 TW Draco laser providing ultra-short laser pulses (30 fs) as introduced in Sec. 2.1. The experimental setup, focusing the beam with an  $F/2.5$  off-axis parabolic mirror to a spot size of about  $3 \mu\text{m}$  (FWHM) leading to an intensity of about  $8 \cdot 10^{20} \text{W}/\text{cm}^2$ , was identical to that used in the experiments presented in the previous chapters in Sec. 3.2.1 and Sec. 2.2. The shape of the temporal contrast on the picosecond time-scale is depicted by the representative curve in Fig. 2.2. As prepulses on the nanosecond time-scale were ruled out with fast photodiode measurements and as the pedestal of amplified spontaneous emission (ASE) exhibits a low intensity, the ionization threshold intensity of  $10^{13} \text{W}/\text{cm}^2$  is exceeded only at  $t = -3 \text{ps}$  before the main pulse.

The targets were irradiated with  $p$ -polarized light at an incident angle of  $\delta = 45^\circ$  (see sketch in Fig. 4.3). By use of rear side (same diagnostic as for focal spot) as well as front side imaging between consecutive laser shots the RMTs were positioned in the laser focus. The pointing stability allowed for a focus fluctuation smaller than the focal spot size and the alignment of the target in the focal depth was achieved with a precision of about  $10 \mu\text{m}$  (see Sec. 2.2).

The angularly resolved energy distribution of the proton pulses emitted from the target rear side under target-normal direction were detected using stacks of radiochromic films

(RCF), consisting of one GafChromic HD layer followed by several GafChromic EBT layers, covered with  $13\ \mu\text{m}$  Al foil and mounted 35 mm behind the target. The used EBT films are absolutely dose calibrated whereas the usable dose range is extended by cross-calibration of the scanner signal obtained from the different color channels. For the measurement of the proton spectra with higher spectral resolution but within a small solid angle ( $0.25\ \mu\text{sr}$ ) a common Thomson parabola spectrometer with CCD readout was applied. In order to compare the proton acceleration performance of different experiment days the reference target system consisting of  $2\ \mu\text{m}$  titanium foils irradiated under  $\delta = 45^\circ$  and p-polarization as introduced in Sec. 2.2 was used. In combination with the Thomson parabola it was used for daily performance optimization and tracking of fluctuations during operation. As additional diagnostic, on the axis of the incident laser beam a magnetic spectrometer dedicated to measure electrons was implemented. The electron signal was read out with a Lanex screen, absolutely calibrated using electron bunches from the ELBE electron accelerator at the HZDR [52].

As a further development of foil sections mounted on wires, in this work an approach based on lithographic technology was introduced to prepare the RMT. This has the advantage, that a large number of targets can be produced in a single batch with high reproducibility and the spatial precision of the fabrication in principle allows for simple automation of the target alignment and thus enables their suitability for high repetition rate laser operation. Furthermore, the targets can be exactly characterized before shooting, making use of the broad range of diagnostics available in semiconductor technology and thus facilitating the study of various target parameters like geometry and composition. In contrast to fully isolated targets (e.g. [167]), one drawback of this technique is the potential influence of the mounting on the hot electron dynamics (see below).

The design of the gold disk targets (custom manufactured by GeSiM) is presented in Fig. 4.3. The disks were produced with different diameters (20, 50, 75 and  $100\ \mu\text{m}$ ) as well as thicknesses (100, 300, 400, 500 and  $1000\ \text{nm}$ ) and are supported by a thin ring structure mounted on a single stalk. During the production, first a thin support layer of  $\text{Si}_3\text{N}_4$  ( $\approx 800\ \text{nm}$  thick) was coated onto a blank wafer (gray color) later providing the supporting ring and stalk structure (marked in blue, width about  $6\ \mu\text{m}$ ). Within the support ring an adhesion layer of  $5\ \text{nm}$  thick titanium (red) followed by the gold layers (orange) of different thicknesses are deposited by sputtering. Finally, a hole of  $1\ \text{mm}$  diameter is etched through the silicon wafer substrate starting from the rear side in such a way that the gold disks remain free standing (refer to the light micrograph left in Fig. 4.3(a)). The geometry of the gold disks was verified with a scanning electron microscope (SEM). As shown by the SEM micrographs in Fig. 4.3(b) the edges of a hole, drilled with an in-situ focused ion beam device, can be used to measure the thickness of the layers with high accuracy. In the initial design the disk targets exhibited four supporting stalks for sufficient stability during the different processing steps. Afterwards three of those stalks were cut manually with a scalpel. In the experiment the laser impinges onto the front of the wafer structure such that

the adhesion layer is positioned at the non-illuminated target rear side (see Fig. 4.3(a)). Although mechanically very stable, the single targets do not withstand the laser-induced shock on the wafer when a neighboring target is irradiated. Consequently, the targets had to be separated from the wafer, usually comprising dozens of single targets, and hence irradiated separately. For future application, this problem can be circumvented by dedicated target holder designs ensuring strict shock isolation.

## 4.2. Experimental results

Maximum proton energies obtained for gold disk targets of the used diameters and for large gold foil targets are presented in Fig. 4.4(a) with different colors according to target thicknesses. In order to compare different experiment days with slightly different performance, all values are normalized to the 2  $\mu\text{m}$  Ti foil reference configuration. Multiple shots on the same target geometry are averaged taking into account the complementary measurements of both the last irradiated RCF stack layer and the Thomson spectrometer output. For large gold foils the thickness scan reveals the usual energy decrease below the optimal thickness of 500 nm, which is due to plasma gradient formation on the non-illuminated surface induced by prepulses or the main pulse itself worsening the accelerating conditions of the TNSA mechanism (see Sec. 3.2.3).

In the case of laterally limited targets the same trend in the thickness dependency can be observed, whereas the maximum energy for the diameters 50, 75 and 100  $\mu\text{m}$  is significantly increased by more than 50% as compared to the large foils. The performance of the smallest diameter target (20  $\mu\text{m}$ ) clearly decreases, although this diameter would favor an energy enhancement due to recirculation and reacceleration of hot electrons being reflected from the target edges in the first place. Equally interesting is the fact that the target thickness dependence is less pronounced for the disk targets than for the extended foils. This implies that the relative proton energy gain using RMTs as compared to large foils of the same thickness shows an increase with decreasing target thickness. This observation is emphasized in the inset of Fig. 4.4(a) for the disk diameter of 75  $\mu\text{m}$ .

Using the angular distribution of the proton fluence recorded with the RCF stacks the proton spectra were reconstructed taking into account spatial distortions of the proton beam profile. Since all gold disk targets (diameters  $>50 \mu\text{m}$ ) yielded similar proton energy spectra (c.f. Fig. 4.4(a)) a representative averaged spectrum comprising all shots on  $>50 \mu\text{m}$  diameter disks of 300 and 1000 nm thickness is plotted in Fig. 4.4(b) and compared to the spectrum of the best performing large gold foil of 500 nm thickness. The proton yield and therefore the laser to proton energy conversion is considerably larger for the disk targets.

In Fig. 4.4(c) preliminary results of the hot electron temperature measurement along the laser incidence axis (see Fig. 4.3(a)) are depicted for the used diameters and thicknesses of the gold disk targets. For gold disks the measured spectra were fitted according to a simple exponential  $\propto \exp(-E/k_B T_e)$  where  $k_B T_e$  denotes the hot electron temperature. The

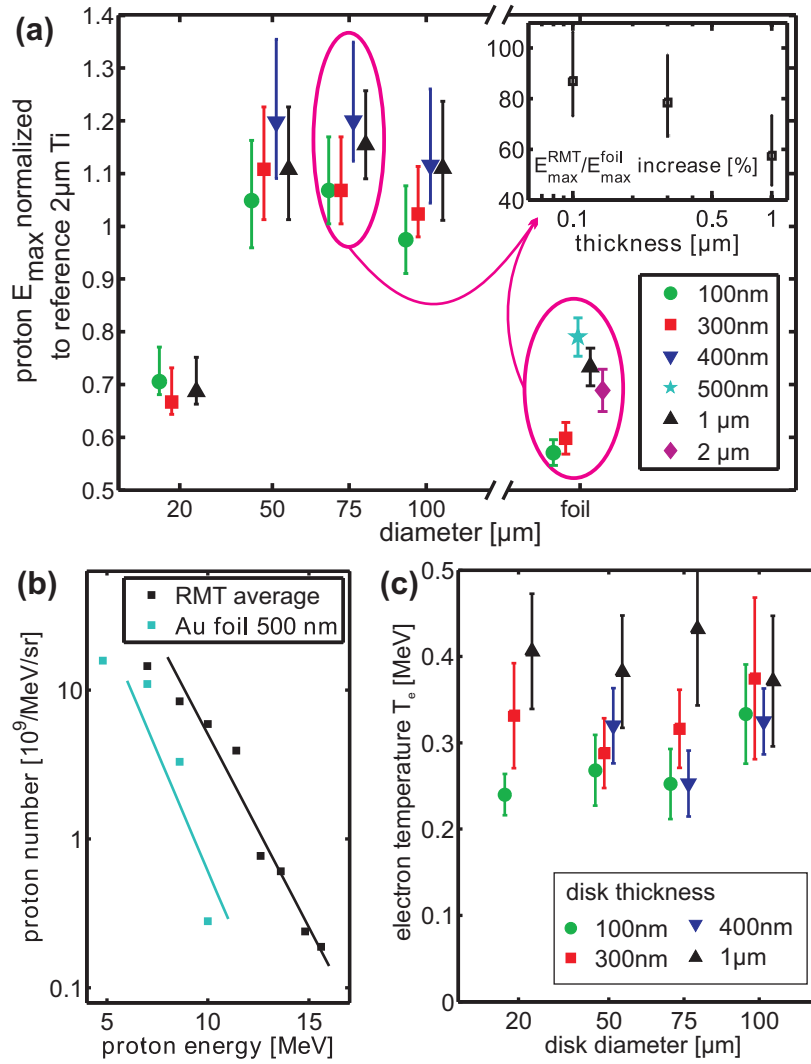


**Fig. 4.4.:** (a) Maximum proton energies using gold disk targets plotted as function of the disk diameter and compared to the performance of large gold foils of the corresponding thickness (color coded). All energy values are normalized to the reference configuration (2  $\mu\text{m}$  Ti foil). (Inset:) For the best performing diameter of 75  $\mu\text{m}$  the percentaged increase of the achieved proton energy using RMTs versus that achieved with the large foil of the same thickness is shown. A slight increase with decreasing target thickness can be observed. (b) Comparison of proton spectrum of the 500 nm thick gold foil and an average spectrum for all shots on gold disks with diameter  $> 50 \mu\text{m}$  and 300 and 1000 nm thickness analyzed along the axis of the proton dose maximum on the RCF layers. The solid lines indicate an exponentially fitted slope of the according proton spectrum. (c) Hot electron temperature measured in the direction of the laser incident axis (see Fig. 4.3(a)) for the gold disks of different diameters and thicknesses.

derived electron temperature is much less than that usually predicted in simulations because in this measurement the low energy component dominates the spectra (insufficient dynamic range to resolve the high electron energy signal). Therefore, the obtained data only allows for a qualitative discussion. However, the interesting signature is that in contrast to the proton energy the electron temperature is not decreasing for the smallest disk diameter of 20  $\mu\text{m}$  (Fig. 4.4(c)). This indicates that the absorption of the laser energy into hot electrons,

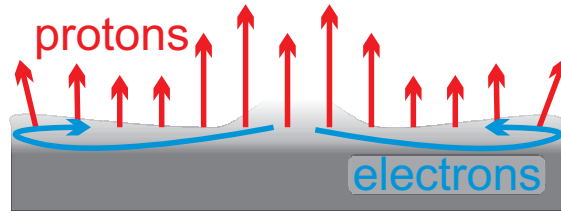


**Fig. 4.5.:** Schematic drawing of the hot electron sheath and electric field generation at the target rear side in the presence of a lateral target confinement. The length of the red arrows indicate the accelerating field strength experienced by the protons. A detailed description is given in the main text.

that is correlated to the  $k_B T_e$  measurement (see discussion in Sec. 3.2.3 and Ref. [144]), is not affected by the lateral target size.

The presented experimental results, namely the increase of proton cut-off energy and proton yield are in good agreement with other studies [40, 171, 159], and are consistent with the model of hot electron reflux as long as one considers that the ultra-short laser pulse triggers a plasma sheath expansion of several hundreds of femtoseconds as effective acceleration time so that electrons being reflected at the target edges can further contribute to the hot electron sheath formation.

The effect that the target thickness dependence is less pronounced for the laterally confined gold disks than for the large foils of the same thickness (shown in the inset of Fig. 4.4(a)) can be attributed to the electron reflux induced plasma sheath homogenization. In Fig. 4.5 a sketch of a scenario here proposed to interpret the experimental findings is depicted. It shows how a more homogeneous sheath along the target surface is formed when electrons are reflected at the target edges and therefore contribute to a larger sheath density at the edges as it would be the case for a large foil at the position of the corresponding edge. The idea is that the region where high accelerating electric fields are available is increased which likewise enables a larger source size of protons potentially being accelerated to highest energies. This leads to the observed proton yield increase in the experiment (Fig. 4.4(b)) and potentially to higher measurable maximum proton energies, and is also consistent with PIC simulations. For thinner targets the plasma gradient generation due to longitudinal electron refluxing in the focal region worsens the acceleration process at the target rear side. However, in the transverse direction the highest accelerating fields in the more homogeneous sheath are available in a larger region. Potentially, this effect can partially compensate for the field reduction in the focal region as it is illustrated by the longer red arrows next to that in the center which corresponds to the focal region (see Fig. 4.5). This scenario remains also consistent with results obtained in previous studies [40, 81] that report on more collimated proton beams for small targets when comparing to large foils.



### 4.3. Investigation of preformed plasma influence and proton source size using PIC simulations

Target diameters supporting an even further enhancement of the kinetic proton energy to that observed in Fig. 4.4 due to re-acceleration of hot electrons during the laser pulse duration were not achieved as seen by the decrease of the maximum proton energy obtained for targets smaller than  $50 \mu\text{m}$ . As mentioned earlier this behavior was recently attributed to preplasma leakage from the laser-illuminated target front surface around the target to the rear surface, resulting in preplasma expansion and thus leading to a reduced formation of the charge separation fields driving the proton acceleration. However, only a correlation of the induced preplasma conditions at the target front surface, where the preplasma strongly affects the absorption mechanisms (c.f. Sec. 3.2.3), and at the rear side with the lateral target dimension would effectively describe the presented experimental results. In the following, this issue will be discussed on the basis of numerical results.

For isolated spherical targets Sokolik *et al.* [167] presented a model based on 2D hydrodynamic simulations estimating the diffusion of a prepulse induced cold plasma corona around the target prior to the main pulse arrival. Assuming a prepulse intensity level of  $10^{12}\text{W}/\text{cm}^2$  with a duration of 0.5 ns, they derived a diffusion length of  $20 \mu\text{m}$  for an oxygen surface plasma. For the experiment presented here the temporal laser pulse contrast curve in Fig. 2.2 shows that an intensity level of  $10^{12}\text{W}/\text{cm}^2$  is not reached before 50 to 10 ps prior to the main pulse. If the model predictions hold true for the laser parameters used in this work and assuming a linear dependence of the diffusion length on the prepulse duration, the influence of a cold plasma diffusion around the gold disks can very likely be neglected, even for the smallest disk diameter used ( $20 \mu\text{m}$ ). This means, the preplasma conditions at the target rear are predominantly influenced by the direct leakage of electrons through the target. The surrounding plasma cloud, in any case less dense and hot, will not reach the rear side focal region before the main pulse arrives at the target.

The contribution of the intense pulse pedestal reaching an intensity level of about  $10^{16}\text{W}/\text{cm}^2$  for a few ps ahead of the main pulse was investigated by applying the 2D3V PIC code PICLS [135, 136]. The simulation parameters were identical to the input in Sec. 3.2.1 and closely resembled the experiment at Draco: laser wavelength 800 nm, laser pulse duration of 30 fs, linear p-polarization, angle of incidence  $45^\circ$  and focal spot size  $5 \mu\text{m}$  FWHM yielding a peak intensity of  $10^{21}\text{W}/\text{cm}^2$ . As depicted in Fig. 3.8 the complete temporal profile of the laser pulse was considered starting at  $t = -3.5$  ps prior to the main pulse where the intensity ionization threshold is reached. When fully ionized, the resulting electron density in the bulk was  $122n_c$ , where  $n_c$  denotes the critical density. Ionization and collisions were included in the simulation. Thick titanium foils ( $1 \mu\text{m}$ ) covered on both sides with a 30 nm thick layer of hydrogen and carbon atoms (edges remained uncovered), and exhibiting different lateral width  $d$  of 20, 40 and  $120 \mu\text{m}$  were implemented as targets.

Emphasizing the most important simulation results, Fig. 4.6(a) shows snapshots of elec-

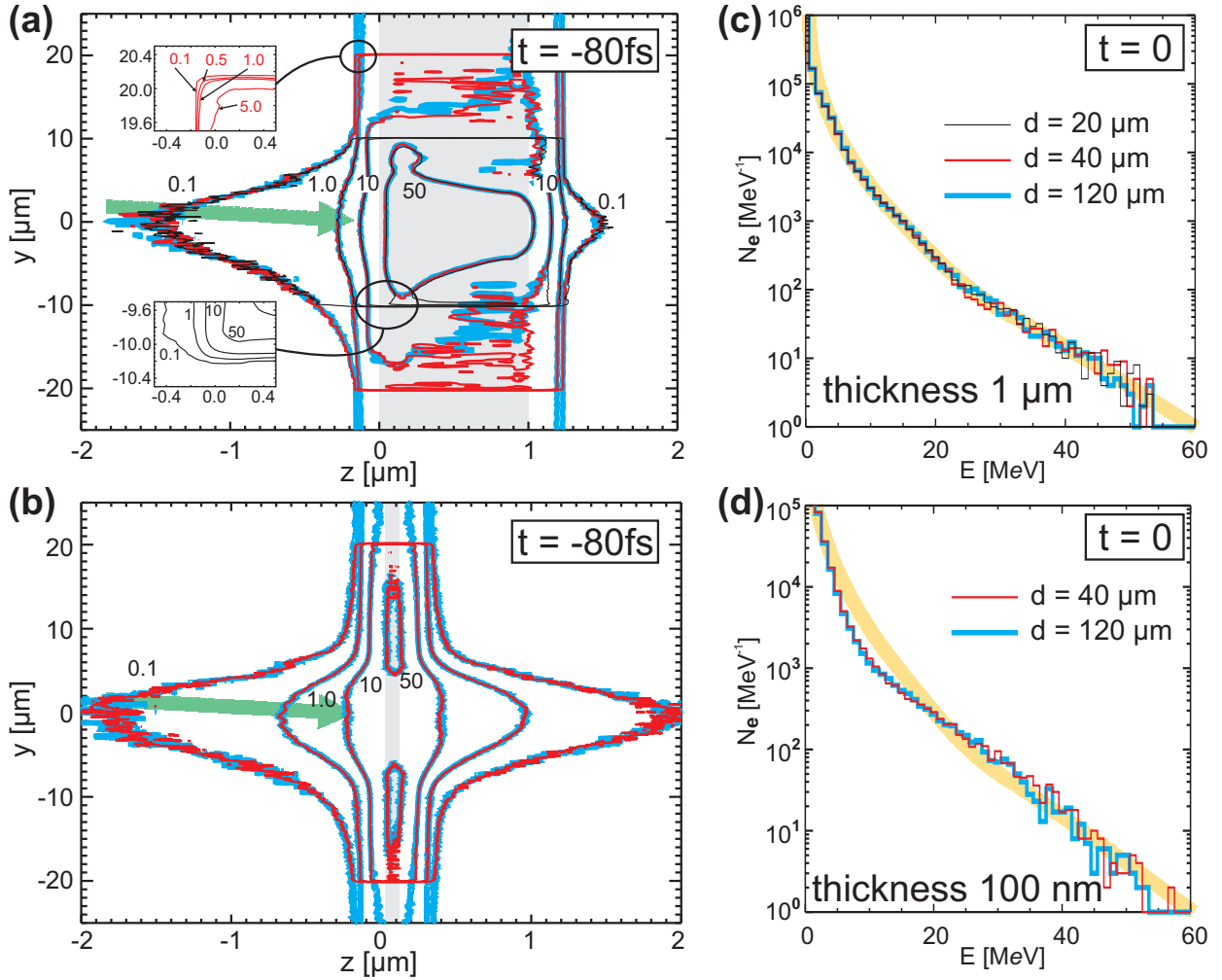


**Fig. 4.6.:** (a) 2D PIC simulation of preplasma conditions at 80 fs before the main pulse ( $t = -80$  fs) interaction induced by an intense ( $10^{16} \text{ W/cm}^2$ ) prepulse starting at  $t = -3.5$  ps (c.f. Fig. 3.8). Electron density contour plots for  $0.1n_c$ ,  $n_c$ ,  $10n_c$ ,  $50n_c$  and different lateral target dimensions  $d$  of 20 (black), 40 (red) and  $120 \mu\text{m}$  (blue). Thereby the  $z$ -direction denotes the target-normal direction just as shown in (a) and the green shaded arrow indicates the laser propagation direction. The insets show magnifications of the target corners for  $d = 20 \mu\text{m}$  and  $d = 40 \mu\text{m}$  at symmetric  $y$  and  $z$ -axis ranges. The thickness of the target (illustrated by the gray shaded area) amounts to  $1 \mu\text{m}$  in (a) and  $100 \text{ nm}$  in (b). (c) and (d) show spectra of all electrons in the simulation box at the time the maximum of the main pulse reaches the target ( $t = 0$ ) plotted for the different target size and thickness configurations. The orange shaded area represents a smoothed curve of the spectra in (c) and is again overlaid in (d) in order to identify the small but significant differences between both target thicknesses.

tron density contour plots  $0.1n_c$ ,  $n_c$ ,  $10n_c$  and  $50n_c$  at 80 fs before the peak of the main pulse reaches the target front surface. In order to analyze the effect of the lateral target confinement, the density contours are compared for the different target widths. The insets of Fig. 4.6(a) represent magnifications of the target corners using symmetric  $y$  and  $z$  axis ranges to illustrate the smooth plasma expansion also at the corners. For all three configurations ( $1 \mu\text{m}$  thickness), a significant preplasma expansion can be observed on either side of the target leaking out into the vacuum at the target front (up to  $1.5 \mu\text{m}$  for  $0.1n_c$ ) and at the

target rear side (up to  $0.5 \mu\text{m}$  for  $0.1n_c$ ). Clearly, the preplasma development on both sides, target rear and front side, is seen to be independent of the target transverse dimension as the different density contours exactly match for the three different target widths. At the target front the laser pulse (green shaded arrow) interacts always with the same amount of underdense preplasma for several microns before reaching the critical density surface that has moved already by a few hundred nanometers. For the large target case of  $d = 120 \mu\text{m}$ , the complete density distribution for electrons, protons and carbon ions at the target center ( $y = 0$ , also for  $t = -80$ ) is given in Fig. 3.16 of the previous chapter.

For the same time step  $t = -80$ , Fig. 4.6(b) shows the density contours for 100 nm thick targets with a width of  $d = 40 \mu\text{m}$  as well as  $d = 120 \mu\text{m}$ . The critical density surface has moved further away from the initial target surface. In particular at the target rear side, the preplasma expansion is significantly enhanced when comparing to the case of the thicker target (Fig. 4.6(a)). However, again no influence of the target width on the expansion of the preformed plasma can be observed.

To no surprise the spectrum of all hot electrons in the simulation box at the time the peak of the main pulse reaches the target  $t = 0$  is identical for the different target widths as depicted in Fig. 4.6(c) and 4.6(d) for the  $1 \mu\text{m}$  and 100 nm thick target, respectively. The reason for this is that the laser interacts with the same preplasma gradient leading to the same absorption efficiency. Only the difference in target thickness is responsible for a small change of the electron temperature (slope of exponential spectra, c.f. Sec. 3.1) as indicated by the orange shaded curve representing the trend of the spectra in Fig. 4.6(c) that is again overlaid in (d) for direct comparison. The small but significant electron temperature increase for the 100 nm thick target is due to the different front side preplasma expansion. As discussed with the plasma expansion model in Sec. 3.1.1, the temperature of the hot electron spectra describes the initial condition for the starting sheath expansion phase that, according to the presented simulation results using realistic laser prepulse contrast, is independent of the lateral target dimension of the order of tens of micrometers.

Only during the expansion phase, hot electron reflux leads to a time-averaged hotter and denser sheath responsible for an enhancement of the maximum proton energy for reduced lateral target sizes. This is shown in Fig. 4.7(a)-(e), where simulated spatial proton and ion density distributions are depicted for the different target widths 20, 40 and  $120 \mu\text{m}$  and thicknesses 0.1 and  $1 \mu\text{m}$  at  $t = 500$  fs after the peak of the main pulse had reached the target (end of simulation). As a clear trend, the maximum proton energy, given in the upper left corner of the images, is increased with reduced transverse target size which supports the experimental results presented in the previous section. Considering the short pulse duration of 30 fs and identical absorption conditions as discussed above, this trend can only be due to the electron reflux effect during the plasma expansion.

Furthermore, the ion density plots, in particular the spatial distributions of protons finally reaching kinetic energies of  $E > 0.5E_{\text{max}}$  (marked in red), reveal the improved sheath homogeneity for the case of the smaller target size. By comparing Fig. 4.7(a) and (b),

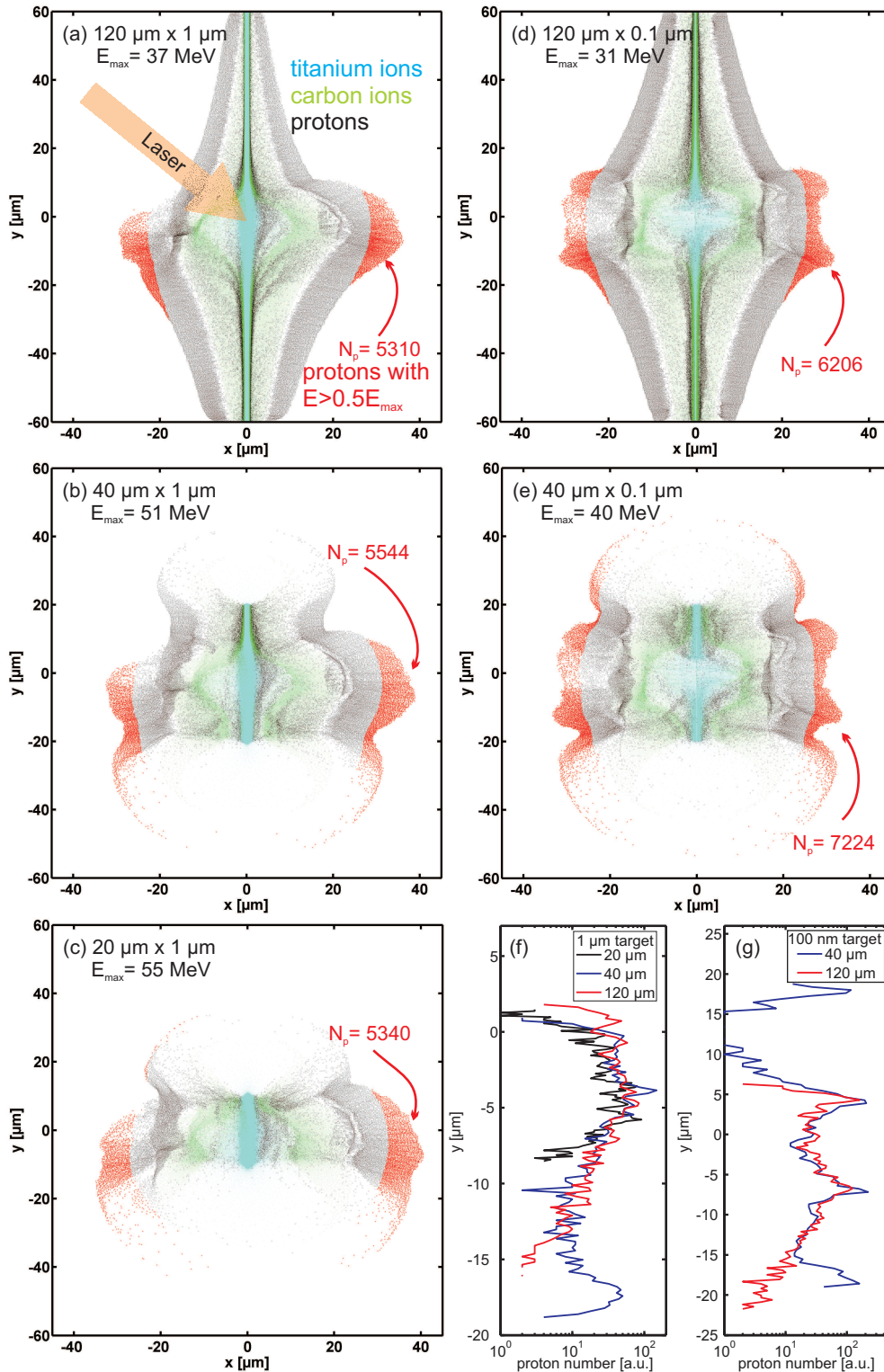


**Fig. 4.7.:** (a)-(e) Simulated spatial proton (black), carbon (green) and titanium (blue) ion density distributions for 0.1 and 1  $\mu\text{m}$  thick targets with different lateral sizes (20, 40, 120  $\mu\text{m}$ ) at  $t = 500\ \text{fs}$  after peak of main pulse had reached target. Maximum proton energy is given with target configuration (upper left corner). Protons with final energy  $E > 0.5E_{\text{max}}$  are plotted in red,  $N_p$  corresponds to the number of these protons in the simulation box. For the same protons, (f) and (g) show histograms of y-coordinate when projected back on  $x = 0$  taking into account the according direction of propagation.

an additional contribution of high energy protons initially stemming from the region in the vicinity of the target edge is visible for the 40  $\mu\text{m}$  target. Simultaneously, the total number of the energetic protons, denoted by  $N_p$ , is increased which is in good agreement with the experiment. This effect is further illustrated by Fig. 4.7(f) presenting histograms of the  $y$ -coordinate of the protons at their initial position on the target surface  $x = 0$ . In contrast to the red curve (120  $\mu\text{m}$ ), the blue curve (40  $\mu\text{m}$ ) exhibits a bump at  $y \sim -17 \mu\text{m}$ , corresponding to the position of the target edge. Thereby, the initial values of  $y$  were derived by projecting the proton position for  $t = 500$  fs back to that at  $t = 0$  by taking the final direction of propagation into account. Considering laminar expansion since the first microns of propagation, this is an appropriate approximation.

Although the hot electron temperature at  $t = 0$  is higher for the thin than for the thick targets, which was attributed to the different absorption, the thin targets (100 nm) yield a smaller maximum proton energy due to the worse rear side preplasma conditions (see Fig. 4.6(b) at  $t = -80$  fs). In the spatial proton distribution Fig. 4.7(d) and (e), and in particular (g) this is correlated to the dip of the proton number ( $E > 0.5E_{\text{max}}$ ) around  $y = 0$  initially corresponding to the focal region. However, for the smaller target, the distribution in (e) and correspondingly the blue curve in (g) again show significant high energy proton emission from the vicinity of the target edges leading to about 16% more energetic protons than for the large target case in (d), and thus reflecting enhanced sheath fields in the edge region during the plasma expansion.

This analysis therefore provides clear indications of a larger size of the region with highest accelerating fields (proton source) when the transverse target size is reduced, because refluxing of electrons at the edges has a significant influence on the spatial distribution of the most energetic protons. This is consistent with the discussion of the thickness effect in Fig. 4.5 as well, where the increased sheath homogenization is suggested to compensate for the gradient degradation in the focal region, especially in the case of thin targets. A quantitative confirmation of this effect in the simulation and a determination of the possible absolute energy gain, however, deserves further parameter scans, such as the investigation of intermediate thickness values between 0.1 and 1  $\mu\text{m}$ .

It should be emphasized again, that the effects discussed here rely on a time-scale of hundreds of femtoseconds that is significantly larger than the pulse duration. However, still the effects are fully consistent with an efficient intra-pulse phase of the proton acceleration process that was addressed in chapter 3. This is confirmed by the prominent non-normal emission of the most energetic protons prevalent in the distributions of Fig. 4.7(a)-(c) and the asymmetric curves in Fig. 4.7(f) and (g) whose center of mass is also shifted towards the direction of the incoming laser beam.

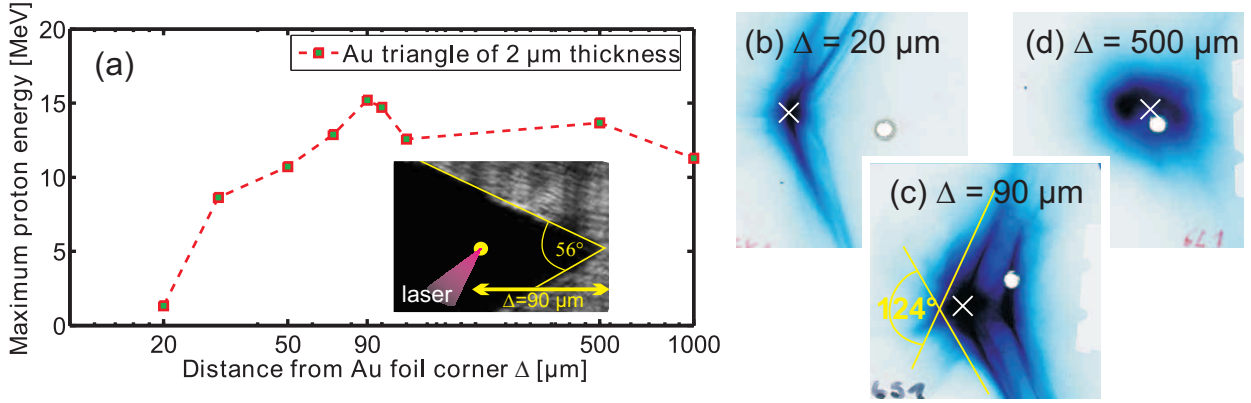


**Fig. 4.8.:** (a) Maximum proton energy measured as function of the distance  $\Delta$  to the tip of corner shaped gold foil sections. The inset shows an image of a target sample to illustrate the setup. The angle between the two edges typically amounted to  $50\text{-}60^\circ$ . (b)-(d) show the first RCF layer of stacks detecting the proton emission pattern for different values of  $\Delta = 20, 90$  and  $500 \mu\text{m}$ . The yellow lines in (c) are perpendicular to the edges of the corner shaped target depicted in inset of (a). As the tip of the foil corner was slightly bent during target preparation, the alignment hole visible on the RCF images did not necessarily correspond to the target-normal direction. The assumed position of the target-normal axis is therefore marked with a white cross.

#### 4.4. Influence of target edges and mounting structure

In contrast to the PIC simulation result for the small  $20 \mu\text{m}$  target in Fig. 4.7(c) yielding higher proton energies than larger targets, in the experiment the gold disk targets with a diameter of  $20 \mu\text{m}$  lead to significantly reduced maximum proton energies (Fig. 4.4(a)). On the other hand, for this target diameter the electron temperature measured along the laser incidence axis behind the target (Fig. 4.4(c)) is comparable to that obtained for the larger targets. As discussed in the previous section, these results cannot be sufficiently described by prepulse induced preplasma effects. A possible explanation could provide the fully three dimensional target mounting structure including the target edges, where the hot electron refluxing enables the generation of accelerating fields that are in the order of the fields in the focal region as discussed above with Fig. 4.7. When the focal region approaches target edges or mounting structure, the dynamics of the Debye sheath could be strongly influenced. On the other hand, inclusion of the real three-dimensional character of the small targets into simulations at solid density is challenging. The 2D-approximation applied here, likely underestimates the edge effects and the complex mounting structure was not considered so far.

Focusing first on the potential influence of the target edges on the proton acceleration performance, small sections of  $2 \mu\text{m}$  thick gold foil with a sharp corner as presented in the inset of Fig. 4.8(a) were prepared and investigated in the experiment. The laser was focused onto the corner shaped targets at different distances from the position of the corner  $\Delta$  and the maximum proton energy as well as the proton beam pattern were detected using RCF stacks see Fig. 4.3. As depicted in Fig. 4.8(a), the general trend of the maximum proton

energy showing an optimum at  $\Delta = 90 \mu\text{m}$  and then decreasing with smaller values of  $\Delta$  is consistent with the experimental results using the gold disk targets in Fig. 4.4.

The distortion of the angular proton beam emission pattern caused by the enhanced electric fields at the target edges is shown in Fig. 4.8(b)-(d). For the three configurations  $\Delta = 20, 90$  and  $500 \mu\text{m}$ , the first RCF stack layer (corresponding to a Bragg peak energy of 1.2 MeV) is presented. While for  $\Delta = 500 \mu\text{m}$  a typical round proton beam can be observed that is overlaid by a faint distortion signal, the proton beam profile for  $\Delta = 20 \mu\text{m}$  and  $\Delta = 90 \mu\text{m}$  is dominated by a strong streak-like distortion. As a clear trend, the round signal in target-normal direction (assumed axis position indicated by white crosses) disappears when the focal region approaches the target edge. The yellow lines in Fig. 4.8(c) are perpendicular to the lines defining the edges of the foil section depicted in the inset of Fig. 4.8(a). Thus the form of the measured proton beam pattern can be attributed to the special sheath field distribution at the target edges, resembling the radial-symmetrical structure of the electric field generated by a linear charge density. Similar findings were recently obtained by Tresca *et al.* [171] in experiments using a long laser pulse duration of 1 ps.

To investigate the influence of the target mounting, another wafer-based but more simple and therefore more cost-saving target design was developed. Square-shaped pure silicon targets were fabricated, all with an edge length of  $100 \mu\text{m}$ , a thickness of  $2 \mu\text{m}$  and with stalks of different width of 2, 5, 10, 20 and  $50 \mu\text{m}$ . An example of the specific RMT configuration is shown in the corner of Fig. 4.9(a). The advantage of the design lies in the reduced number of processing steps. The basic idea is to use silicon wafers consisting of three layers, a thick silicon substrate layer, a buried very thin silicon oxide layer and on top again a thin (in this case  $2 \mu\text{m}$ ) silicon layer. This wafer design allows for structuring of the substrate and the top layer separately and to etch the top and the substrate silicon layers down to the silicon oxide layer serving as etching boundary. After finally releasing the oxide layer, free standing targets remain in the center of a surrounding hole in the substrate (here  $0.5 \text{ mm}$  edge length). Again, three out of the four supporting stalks of the initial design were cut manually such that all targets were supported by one single stalk or two stalks for the case of  $2 \mu\text{m}$  width due to stability constraints. Additionally, with the same technique  $2 \mu\text{m}$  thick large silicon foils were produced for comparison.

The silicon RMTs were irradiated with laser pulses in the same configuration as shown in Fig. 4.3 and the angularly resolved proton energy distributions were again measured with RCF stacks. A representative selection of RCF output for each stalk configuration including the large foil case is depicted in Fig. 4.9(a). Each RCF layer corresponds to a dose distribution at a certain depth in the RCF material and the Bragg peak energy of protons stopping in the according layer is marked on the  $x$ -axis. Starting with the large foil case, a smooth proton dose distribution was obtained being very similar to those usually measured with large metal foils at similar laser parameters as expected for TNSA. By application of the RMTs, the proton emission distribution is distorted as revealed by the peculiarly disturbed

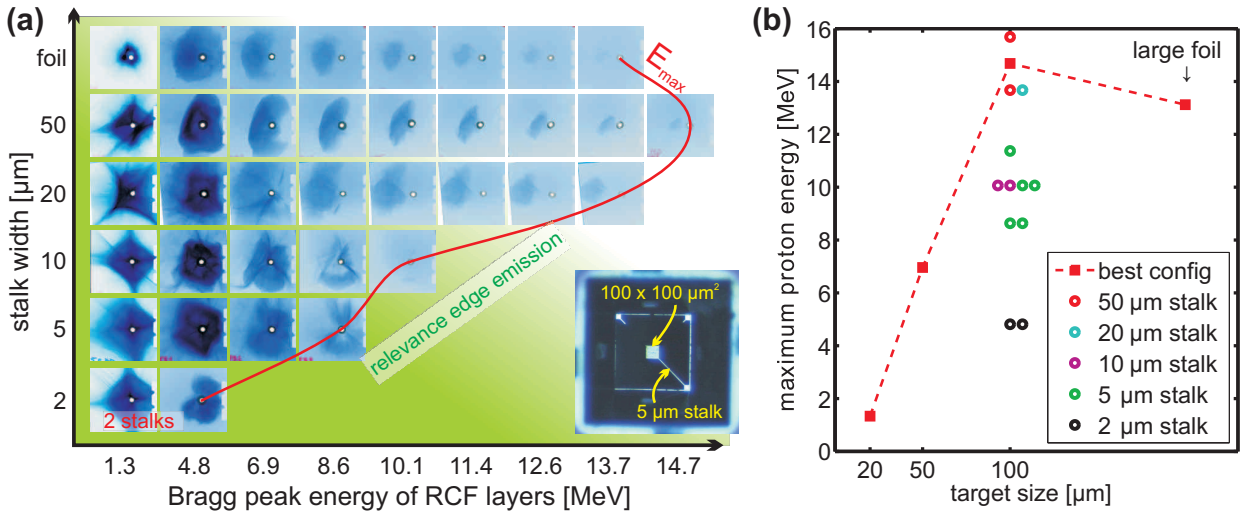


**Fig. 4.9.:** (a) Representative selection of RCF stack data measured for silicon RMTs. All targets have the same size of  $100 \times 100 \mu\text{m}^2$  but the width of the mounting stalk is varied from 2 to  $50 \mu\text{m}$ . The red curve shows the trend of the achieved maximum proton energy corresponding to the last RCF layer that detects any dose signal. The relevance of the distortion of the proton emission characteristic induced by edge field effects is indicated by the background shaded in green. (b) Maximum proton energy as function of the target size at the best performing stalk configuration. The colored circles represent the scattering of the proton energy for the shots on the targets with a size of  $100 \mu\text{m}$  as in (a) and varied stalk width.

proton emission pattern. For the  $50 \mu\text{m}$  stalk width only the first layer exhibits this structure while for decreasing stalk width the distribution at higher energy layers is affected as well. In parallel, the maximum proton energy, corresponding to the last irradiated film layer, is slightly increased for the RMT ( $50 \mu\text{m}$  stalk) compared to the large foil but then decreases with decreasing stalk width. For better comparison the set of achieved maximum proton energy data is shown again in Fig. 4.9(b). Additionally, the maximum proton energy as function of the target size is plotted for the best performing stalk configuration for each specific target size. Comparing to Fig. 4.4 and Fig. 4.8 the same trend can be observed, namely that a reduced target size yields better proton energies as the large foil, although not so pronounced as for the gold disks in Fig. 4.4, and then targets with sizes of  $50 \mu\text{m}$  and below perform significantly worse.

Similar to the experiment using the small foil sections with the sharp corner in Fig. 4.8, the most evident assumption is that the distortion of the proton emission distributions is directly linked to strong electric fields at the target edges and here additionally to those occurring in the vicinity of the stalks. These strong edge fields not only provide for an efficient proton acceleration at the edges but on the other hand seem to suppress efficient acceleration conditions in the focal region. The presence of residuals of the disturbed emission pattern at the 4th RCF layer ( $5$  and  $10 \mu\text{m}$  stalks) corresponding to proton energies exceeding  $8 \text{ MeV}$  suggests that hot electrons initially generated in the focal region induce proton acceleration at the edges, being similarly effective as at the focal region. By shaping the supporting



stalks more wire-like, i.e. by further reducing their widths, the edge field effect even seems to increase because the energy of protons stemming from the focal region decreases dramatically indicating to a significant reduction of the accelerating fields there. Note that the maximum proton energy is smaller for two stalks of  $2\ \mu\text{m}$  thickness than for one stalk of  $5\ \mu\text{m}$ . This complex behavior can be related to results reported on hot electron transport in wires. A simulation in Kodama *et al.* [173] shows hot electrons generated at the surface of a laser-illuminated cone target and being captured in the huge electric fields generated around a wire structure attached to the tip of that cone. Experiments to identify such an effect for the silicon targets based on optical probing measurements as well as further numerical studies are in progress.

For the gold disk targets showing high proton acceleration performance, although stalk width of only  $6\ \mu\text{m}$  were used (see Fig. 4.4), the influences of mounting and edges seem to be less important, which could be due to the different target material (see appendix B). However, reducing the disk diameter and thus shifting the focal region closer to the mounting evidently changes the situation and the edge field effect could therefore serve as an explanation for the reduced maximum proton energies observed for the disks with  $20\ \mu\text{m}$  diameter.

Since the targets all exhibit the same lateral size and only the stalk width is varied, the assumption that prepulse induced preformed plasma in particular at the target rear surface is predominantly generated in the focal region directly is confirmed. An influence of the surrounding plasma corona on the trend of the proton energy decrease presented in Fig. 4.9(a) can be neglected as this effect should be insensitive to the stalk width. However, a prepulse induced ionization of the surface atoms before the main pulse arrival (see Fig. 4.6) could influence the scenario described in this section. A further analysis therefore demands time resolved measurements of the electric field structure before but also during the main pulse interaction with high temporal resolution. Numeric modeling is also very challenging because, clearly, three dimensional effects on the picosecond as well as on the femtoseconds time-scale have to be considered.

## 4.5. Summary

Small gold disks exhibiting diameters of tens of micrometers and different thicknesses were investigated as reduced mass targets for the effective generation of intense proton pulses using ultra-short laser pulses (30 fs). Similar to previous studies the maximum achievable proton energy (up to 80%) as well as the proton yield were significantly increased compared to large foils of the same thickness and material. Likewise, this result was attributed to hot electron reflux caused by the lateral confinement of electrons and yielding a denser, hotter and in particular a more homogeneous hot electron sheath during the effective sheath expansion time of the proton acceleration process. It is important to note, that in particular for the case of ultra-short laser pulses, this is still fully consistent with an efficient intra-pulse

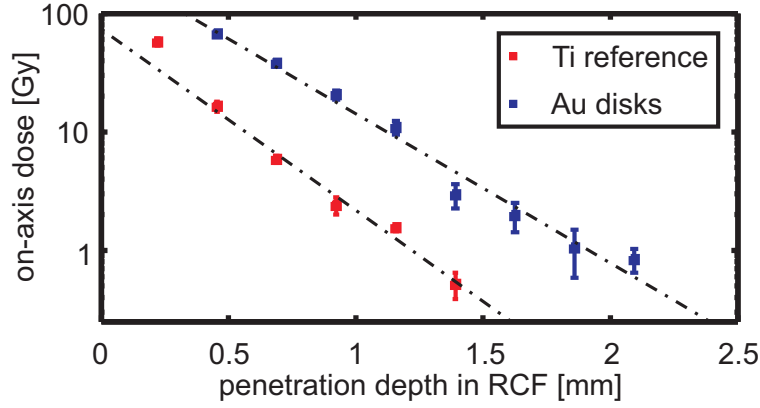


**Fig. 4.10.:** *On axis depth dose distribution, measured at 35 mm behind the target and averaged over shots onto titanium reference foil target and RMT (c.f. Fig. 4.4).*

phase of the proton acceleration process in which protons can already gain a relevant part of their final kinetic energy as discussed in the previous chapter (see Sec. 3.2).

As a novel experimental signature a reduced dependence on the target thickness for RMTs compared to large foils was demonstrated and explained by the homogenization of the electron sheath giving rise to an enlarged proton source size. This robustness with respect to the change of the target thickness indicates that RMTs are valuable targets in order to optimally exploit the available accelerating fields for given laser parameters. A reduced thickness dependence allows for the opposite conclusion that the proton acceleration performance is less sensitive with respect to fluctuations of the laser pulse contrast. This in combination with the lithographic technology based target fabrication makes RMT suitable for applications such as radiobiological studies [47] using lasers with full 10 Hz operation. In order to emphasize the positive RMT effect a direct comparison of the proton acceleration performance obtained with the gold disk RMT and the robust and well established reference configuration using flat titanium foils is presented in Fig. 4.10. The measured depth dose profiles show an increase of the accessible dose per pulse by a factor of 6 for the RMT. By choice of another target material this could potentially be further improved (see appendix B). Therefore the here developed gold disk targets are a promising tool to increase the proton dose per pulse when implemented into the setup of the envisaged *in vivo* irradiation experiments depicted in Fig. 2.9.

Moreover, it was demonstrated that a further reduction of the target size down to the focal spot size promising a further improvement of the proton beam parameters by re-acceleration of hot electrons during the laser pulse duration is difficult and requires the mounting to be significantly improved. Here this was explained by large electric fields generated at the target mounting and thus perturbing the expanding hot electron sheath. This important effect, in particular the question why and how exactly the electric field distribution at the target edges as well as the mounting structure suppress efficient proton acceleration conditions in the focal region needs to be further investigated in order to improve the target design and to increase the achievable proton energy.

## 5. Conclusion

This thesis provides detailed understanding of the TNSA mechanism in the ultra-short pulse regime and demonstrates the feasibility of a laser-driven proton accelerator for radiobiological studies. An important result of this work is the first demonstration of effective acceleration of proton pulses to energies around 20 MeV in the established TNSA regime using state-of-the-art 100 TW class ultra-short pulse lasers such as the Draco system at the HZDR. This was achieved with plain micron-thick foil targets and non-destructive laser pulse cleaning techniques (i.e. no plasma mirrors) so that stable and reliable operation making use of the full repetition rate of the laser can be provided for application. Within this work, an application of this system has been realized. A laser-driven dose delivery system dedicated for the *in vitro* cell irradiation with proton pulses was implemented and operated at a performance level sufficient for radiobiological studies on a shot-to-shot basis as well as on long time-scales of several weeks and with a precise delivery of prescribed doses. Methods and components of the presented approach such as real-time transmission dose monitoring can be directly scaled to higher proton energies, later required for proton cancer therapy. To validate this performance level, a dose effect curve was measured with laser-accelerated proton pulses and compared to a curve measured using a continuous Tandem source. No difference of the biological effect has been observed and taking further existing studies into account it seems that in the therapeutically relevant dose range of a few Gy, even if applied in a single pulse of only few nanoseconds duration, non-linear radiobiological effects due to simultaneous multiple damages in cells and thus below any time-scale of repair mechanisms are unlikely to arise. The next step to bring laser-driven proton beams closer to clinical application will be the extension of the experiments to volume irradiation in animal experiments. However, in comparison to the studies on biological effects in two-dimensional cell monolayers these experiments are more complex and require higher and tunable proton energies.

This leads over to the investigation of feasible routes to increase the proton energies to up to 250 MeV as required for radiation therapy with high power lasers, and that is being addressed in the second part of this thesis. Measurements of the achievable maximum proton energy as function of the Draco laser power presented in this work suggest that already with 500 TW class lasers, the present maximum proton energy of about 70 MeV reached with high-energy long pulse lasers could be realized. This estimation is based on a theoretical consideration that builds on the established model by Schreiber *et al.* [75] and that is here extended to the ultra-short pulse regime (tens of femtoseconds) thereby predicting a near-linear scaling of the proton energy increase with laser power, rather than the square-root

scaling previously established for long laser pulse durations  $> 100$  fs. If this faster scaling holds true for the envisaged increase in intensities by application of the upcoming class of ultra-compact Petawatt lasers with high pulse repetition rate, the presently achieved proton energy level suggests that 100 MeV proton pulses could be in reach.

This hypothesis is furthermore supported by the experimental results on investigating the proton acceleration processes within the target-normal sheath acceleration regime with respect to their effective time-scale and their contribution to the achievable maximum proton energy. Using the ultra-short laser pulses (30 fs) from the Draco system at oblique laser incidence, it was shown that the thermal (or adiabatic) plasma expansion [3], giving TNSA its name, in fact is preceded by an effective quasi-static component (prethermal) induced by electrons promptly accelerated by the laser at the target front surface. This implies that for ultra-short and ultra-intense pulses the time evolution of the initial state (intra-pulse) of the quasi-self-similar plasma expansion has to be taken into account to predict achievable maximum proton energies.

The relevance of the intra-pulse phase was shown by measuring angular proton beam deflection induced by angularly chirped laser pulses as a diagnostic. The next step will be to investigate the contribution of both phases (prethermal and thermal expansion) to the acceleration process by, e.g., studying the influence of the laser pulse duration on the relation of proton beam deflection and chirp parameter. By using two independent laser pulses, a staged approach based on an efficient intra-pulse injector and a longer plasma post acceleration could improve energy and control of laser-accelerated proton beams in the future. In principle, this can be combined with a prepared composition of source layers on the back of the foil to well define the starting conditions of the acceleration and thus to enable to monoenergetic features [80, 78]. However, it is evident that efficient proton acceleration, in particular when increasing the laser intensity, calls for optimal temporal laser contrast on target implying not only that initially extreme contrast has to be provided but also that means to control and even adjust certain preplasma conditions are indispensable.

As another promising approach in the last part of this work it was demonstrated that the choice of an appropriate target geometry improves the proton acceleration efficiency during the plasma expansion phase. Confinement of the lateral target size leads to a reduction of the electron spreading being responsible for the dilution of the expanding plasma sheath and thus limiting the time-averaged strength of the accelerating fields. The results of experiments conducted with small targets of different diameter and different thickness suggest that the sheath electrons get reflected at the target edges and contribute to a time-averaged hotter, denser and in particular more homogeneous expanding sheath. This yields significant higher proton energies (up to 80 % increase) as when compared with large planar foils of the same thickness. The increased homogeneity of the expanding plasma sheath leads to an enlarged proton source size, or in other words increases the number of protons experiencing the largest accelerating fields. In the experiment this is shown by the significant increase of the yield of high energy protons by about one order of magnitude when compared with planar foils

and being of high interest for the envisaged *in vivo* irradiation experiments. Moreover the larger size of the high energy proton source leads to a less sensitive proton acceleration performance with respect to fluctuations of the laser pulse contrast that will also assist to exploit the maximum achievable proton energy at increased laser intensities.

## A. Coupling of spatio-temporal distortions

This section is related to the test experiment using angularly chirped pulses in Sec. 3.2.2. Here the formation of spatio-temporal distortions and the consequences of focusing will be discussed and illustrated by an analytic wave-optical treatment based on basic Fourier transformation. Conceptually, this discussion is mainly based on the publication by Akturk *et al.* [138] as well as the book by Goodman [174]. A general theory and derivation of the first-order spatio-temporal distortions of Gaussian pulses and beams based on the Kostenbauder matrix formalism [140] can be consulted in Ref. [175].

Usually, the space and time dependencies of the electric field of an ultra-short laser pulse are assumed to be independent. If coupling between those components occurs, it is referred to as spatio-temporal distortion. The most important quantities for the presented experiment in a first-order approximation are angular chirp (AC), pulse front tilt (PFT) and spatial chirp (SC), and are given by

$$\begin{aligned}
 \text{AC} & : \quad \left. \frac{\partial \varphi}{\partial \omega} \right|_{\varphi=\varphi_0} \\
 \text{PFT} & : \quad \left. \frac{\partial t}{\partial x} \right|_{t=t_0} \\
 \text{SC} & : \quad \left. \frac{\partial x}{\partial \omega} \right|_{x=x_0},
 \end{aligned} \tag{A.1}$$

where  $\varphi$  denotes the propagation angle,  $\omega$  the frequency,  $t$  the time and  $x$  the spatial coordinate (only AC in  $x$ -direction is considered). Ideally, the propagating pulse is free from such distortions, but very small misalignments within the stages of pulse stretching and pulse recompression are often impossible to avoid when generating an ultra-short intense laser pulse in the chirped pulse amplification scheme (CPA), as for example with the Draco system. In the proton acceleration experiment discussed above, a small AC is intentionally introduced in order to change the spatio-temporal properties of the focused laser pulse and therefore the spatio-temporal dynamics of the laser-plasma interaction.

In a simple picture, AC and PFT are regarded to be equivalent, which can be shown using Fourier transformation. Omitting the  $y$ -dependence and assuming no further correlation of coordinates, the components of the complex field of a beam in the  $k\omega$ -domain including an

AC can be written as

$$\hat{U}(k_x, k_z, \omega) = \hat{U}_{k_x, k_z}(k_x - p\omega, k_z) \hat{U}_\omega(\omega). \quad (\text{A.2})$$

Here, the AC  $\partial\varphi/\partial\omega = p/k_0$  is expressed by  $\partial k_x/\partial\omega = p$ , with  $k_0$  being the nominal wave-number in vacuum. Applying a standard inverse Fourier transform of the complex field with respect to its space coordinates

$$\mathcal{F}^{-1}\{\hat{U}(k_x, k_y)\} = U(x, y) = \int_{-\infty}^{\infty} \hat{U}(k_x, k_y) \exp[j2\pi(k_x x + k_y y)] dk_x dk_y \quad (\text{A.3})$$

in combination with the shift theorem expressed for an arbitrary function  $G(x, y)$  by

$$\mathcal{F}\{G(x - a, y - b)\} = \hat{G}(k_x, k_y) \exp[-j2\pi(k_x a + k_y b)], \quad (\text{A.4})$$

and simply meaning that a translation in the space domain introduces a linear phase shift in the frequency domain, (A.2) becomes

$$\tilde{U}(x, z, \omega) = \tilde{U}_{xz}(x, z) \tilde{U}_\omega(\omega) \exp[j2\pi p\omega x]. \quad (\text{A.5})$$

Another inverse Fourier transform with respect to  $\omega$ , and reapplying the shift theorem finally leads to

$$U(x, z, t) = U_{xz}(x, z) U_t(t - px) \quad (\text{A.6})$$

corresponding to the field of a laser beam with a pulse front tilt  $\partial t/\partial x = p$  in the  $xt$ -domain. While this transformation seems quite fundamental, Akturk *et al.* have shown in Ref. [138], that this equivalence only holds true for fields in the above form and is violated for example by the presence of a SC in the beam. In that case, (A.5) is not sufficiently general anymore, because in addition to the phase term another coupling in the  $x\omega$ -domain has to be included for the SC (c.f. (A.1))

$$\tilde{U}(x, z, \omega) = \tilde{U}_{xz}(x - \gamma\omega, z) \tilde{U}_\omega(\omega) \exp[j2\pi p\omega x]. \quad (\text{A.7})$$

In the following, it will be shown that such a coupling in the  $x\omega$ -domain, can immediately be generated by transferring a field with a linear phase shift as given by the simple exponential in (A.5) into the focal plane (far field), as it is in principle done in the experiment. With other words, an AC in the near field is translated into a SC in the far field because focusing can be represented by another Fourier transform of the spatial coordinates. Vice versa, the presence of a SC in the near field will cause an AC in the focus and therefore will contribute to a PFT in the focal plane of the laser.

But before continuing to demonstrate this relationship, the useful property of a thin lens being able to perform as a phase transformation and Fourier transformer within the diffraction theory of light, will be briefly reviewed. The side view of a general lens geometry

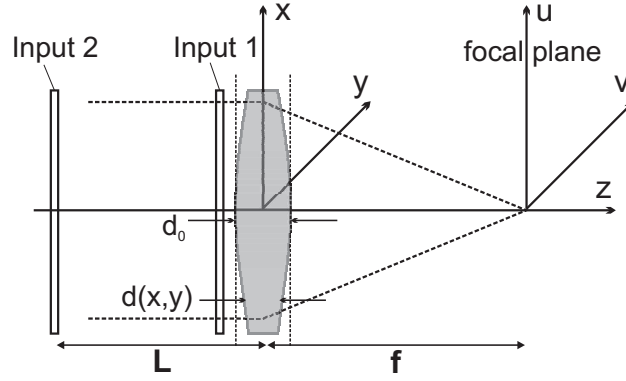


**Fig. A.1.:** Schematic overview of a lens performing a Fourier transform operation of the input field.

is shown in Fig. A.1. The maximum thickness is  $d_0$  and the thickness at coordinates  $(x, y)$  is  $d(x, y)$ . The total phase delay experienced by a wave when passing through the lens is given by

$$\Phi(x, y) = knd(x, y) + k[d_0 - d(x, y)] \quad (\text{A.8})$$

where  $n$  is the refractive index of the lens material,  $knd(x, y)$  is the phase delay caused by the lens and  $k[d_0 - d(x, y)]$  the delay corresponding to the remaining free space between the two planes. Consequently, the complex field in front of the lens  $U(x, y)$  (Input 1 in Fig. A.1) is transformed by a multiplicative phase and the field immediately behind the lens  $U'(x, y)$  then reads

$$U'(x, y) = U(x, y) \exp[jkd_0] \exp[jk(n-1)d(x, y)]. \quad (\text{A.9})$$

With the help of the paraxial approximation the thickness function  $d(x, y)$  becomes

$$d(x, y) = d_0 - \frac{x^2 + y^2}{2} \left( \frac{1}{R_1} - \frac{1}{R_2} \right) \quad (\text{A.10})$$

with  $R_1$  denoting the curvature radius of the right-hand lens surface and  $R_2$  for the left-hand one. Together with the well-known expression of the focal length for a thin lens  $f^{-1} = (n-1)(1/R_1 - 1/R_2)$  and neglecting the constant phase factor, (A.9) finally reads

$$U'(x, y) = U(x, y) \exp \left[ -j \frac{k}{2f} (x^2 + y^2) \right]. \quad (\text{A.11})$$

In order to determine the field distribution (in  $(u, v)$  coordinates) in the back focal plane of the lens  $U_{z=f}(u, v)$  the Fresnel diffraction formula [174] as an approximation of the Huygens-Fresnel principle

$$U_f(u, v) = \frac{\exp[jkf] \exp \left[ j \frac{k}{2f} (u^2 + v^2) \right]}{j\lambda f} \times \int_{-\infty}^{\infty} U'(x, y) \exp \left[ j \frac{k}{2f} (x^2 + y^2) \right] \exp \left[ -j \frac{2\pi}{\lambda f} (xu + yv) \right] dx dy \quad (\text{A.12})$$



has to be applied. Substituting (A.11) into (A.12), the quadratic phase factors within the integrand exactly cancel, and assuming an input field smaller than the lens aperture,  $U_f(u, v)$  finally reads

$$U_f(u, v) = \frac{\exp[jkf] \exp\left[j\frac{k}{2f}(u^2 + v^2)\right]}{j\lambda f} \times \int_{-\infty}^{\infty} U(x, y) \exp\left[-j\frac{2\pi}{\lambda f}(xu + yv)\right] dx dy. \quad (\text{A.13})$$

Thus the complex field amplitude in the focal plane of a thin lens is proportional to the Fourier transform of the incident field with

$$k_x = \frac{u}{\lambda f} \quad \text{and} \quad k_y = \frac{v}{\lambda f}. \quad (\text{A.14})$$

For the case the input is placed in front of the lens at a distance  $L$  (Input 2 in Fig. A.1) the field in the focal plane can be rewritten as

$$U_f(u, v) = \frac{\exp[jkf] \exp\left[j\frac{k}{2f}\left(1 - \frac{L}{f}\right)(u^2 + v^2)\right]}{j\lambda f} F_0\left(\frac{u}{\lambda f}, \frac{v}{\lambda f}\right) \quad (\text{A.15})$$

with  $F_0(k_x, k_y) = \mathcal{F}\{U(x, y)\}$  where  $U(x, y)$  is still the field that incidents normally against the lens (c.f. (A.9)). Exemplarily, for the special case of a propagation distance  $L = f$  the quadratic phase term cancels, and apart from constant factors this leads to

$$U_f(u, v) = F_0\left(\frac{u}{\lambda f}, \frac{v}{\lambda f}\right) \quad (\text{A.16})$$

illustrating the ability of the lens as a Fourier transformer. Applying the relation of (A.16) to the field expression in the  $x\omega$ -domain (A.5) yields

$$\begin{aligned} \tilde{U}_f(u, \omega) &= \mathcal{F}\left\{\tilde{U}(x, \omega)\right\}\Big|_{k_x=u/f\lambda} \\ &= \int_{-\infty}^{\infty} \tilde{U}_x(x) \tilde{U}_\omega(\omega) \exp[j2\pi p\omega x] \exp[-j2\pi x k_x] dx \Big|_{k_x=u/f\lambda} \\ &= \tilde{U}_u\left(\frac{1}{f\lambda}(u - p\omega f\lambda)\right) \tilde{U}_\omega(\omega) \end{aligned} \quad (\text{A.17})$$

corresponding to a field in the focus exhibiting a SC  $\partial u/\partial\omega = pf\lambda$  as introduced in (A.7).

In conclusion, (A.17) confirms the intuitive assumption that an AC in the near field, being equivalent to a PFT for fields of the form in (A.2) translates into an SC in the far field. Vice versa, the presence of SC in the unfocused beam (near field) leads to an AC and therefore PFT in the focus directly, which can be seen by simply exchanging the role of the spatial variables  $u$  and  $x$ .

## B. Influence of the target material

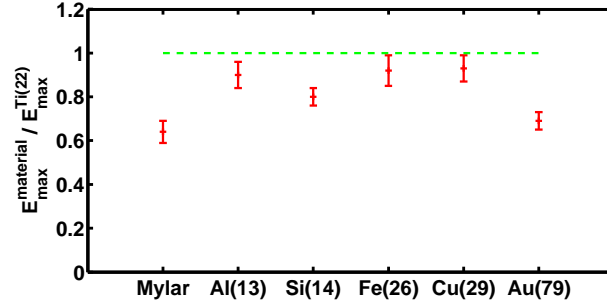


**Fig. B.1.:** Maximum proton energy obtained as function of the material of flat foil targets. The target thickness was always  $2 \mu\text{m}$ . Multiple consecutive shots were averaged and normalized by the performance achieved with the titanium foil as reference. The ion charge number  $Z$  of the materials is given in parenthesis.

As already visible by the comparison of the obtained maximum proton energies using gold foils and the titanium reference foil in Fig. 4.4(a), the question of the ideal target is of course also a question of the right target material. However, not only for the achievable maximum proton energy the target material seems to be important as indicated by the different target size dependence of silicon and gold RMTs in Fig. 4.4(a) and Fig. 4.9(b). For the more simple case of flat foils, exhibiting a thickness of  $2 \mu\text{m}$ , the proton acceleration performance as function of the target material was investigated using the same experimental setup and laser parameters as described in Fig. 4.3. The results, again normalized to the titanium reference are plotted in Fig. B.1. For the experimental conditions at Draco, the titanium foil reveals the best performance. A clear dependence on the ion charge number, however, cannot be observed. This is in contrast to recent results obtained at the Polaris laser (Jena, Germany), showing that the maximum proton energy seems to increase with the ion charge number  $Z$  [176]. Yet, a complete understanding of the material influence on the proton acceleration and the RMT effect demands further extensive experimental and numerical investigations which are still in progress. The expansion of the target surfaces induced by the prepulses or the main pulse depends on the ion sound speed (see Sec. 3.1.1) and is therefore affecting the laser absorption and the quality of the target rear side gradient. Even for laser intensities below the ionization threshold, prepulses can influence the thermal properties of the target, that then can be sensitive to the exact material in use [162]. In addition, the electron transport through the target can be very sensitive to the particular target material due to resistivity effects as was recently introduced in Ref. [177].

# Bibliography

- [1] D. Strickland and G. Mourou. Compression of amplified chirped optical pulses. *Optics Communications*, 56:219, 1985.
- [2] S.C. Wilks, A.B. Langdon, T.E. Cowan, M. Roth, M. Singh, S. Hatchett, M.H. Key, D. Pennington, A. MacKinnon, and R.A. Snavely. Energetic proton generation in ultra-intense laser–solid interactions. *Physics of Plasmas*, 8(2):542–549, 2001.
- [3] P. Mora. Thin-foil expansion into a vacuum. *Physical Review E*, 72(5):056401, 2005.
- [4] T.E. Cowan, J. Fuchs, H. Ruhl, A. Kemp, P. Audebert, M. Roth, R. Stephens, I. Barton, A. Blazevic, E. Brambrink, J. Cobble, J. Fernández, J.-C. Gauthier, M. Geissel, M. Hegelich, J. Kaae, S. Karsch, G.P. Le Sage, S. Letzring, M. Manclossi, S. Meyeroneinc, A. Newkirk, H. Pépin, and N. Renard-LeGalloudec. Ultralow emittance, multi-MeV proton beams from a laser virtual-cathode plasma accelerator. *Physical Review Letters*, 92:204801, 2004.
- [5] C.K. Li, F.H. Séguin, J.A. Frenje, J.R. Rygg, R.D. Petrasso, R.P.J. Town, P.A. Amendt, S.P. Hatchett, O.L. Landen, A.J. Mackinnon, P.K. Patel, V.A. Smalyuk, T.C. Sangster, and J.P. Knauer. Measuring E and B fields in laser-produced plasmas with mmoenergetic proton radiography. *Physical Review Letters*, 97:135003, 2006.
- [6] L. Romagnani, J. Fuchs, M. Borghesi, P. Antici, P. Audebert, F. Ceccherini, T. Cowan, T. Grismayer, S. Kar, A. Macchi, P. Mora, G. Pretzler, A. Schiavi, T. Toncian, and O. Willi. Dynamics of electric fields driving the laser acceleration of multi-MeV protons. *Physical Review Letters*, 95:195001, 2005.
- [7] P.V. Nickles, M. Schnürer, T. Sokollik, S. Ter-Avetisyan, W. Sandner, M. Amin, T. Toncian, O. Willi, and A. Andreev. Ultrafast laser-driven proton sources and dynamic proton imaging. *Journal of the Optical Society of America B*, 25:B155, 2008.
- [8] P. Antici, M. Fazi, A. Lombardi, M. Migliorati, L. Palumbo, P. Audebert, and J. Fuchs. Postacceleration of laser-generated high-energy protons through conventional accelerator linacs. *Plasma Science, IEEE Transactions on*, 36(4):1843–1846, 2008.
- [9] M. Nishiuchi, I. Daito, M. Ikegami, H. Daido, M. Mori, S. Orimo, K. Ogura, A. Sagisaka, A. Yogo, A. S. Pirozhkov, H. Sugiyama, H. Kiriyaama, H. Okada, S. Kanazawa, S. Kondo, T. Shimomura, M. Tanoue, Y. Nakai, H. Sasao, D. Wakai, H. Sakaki,

- P. Bolton, I.W. Choi, J.H. Sung, J. Lee, Y. Oishi, T. Fujii, K. Nemoto, H. Souda, A. Noda, Y. Iseki, and T. Yoshiyuki. Focusing and spectral enhancement of a repetition-rated, laser-driven, divergent multi-MeV proton beam using permanent quadrupole magnets. *Applied Physics Letters*, 94:061107, 2009.
- [10] M. Roth, I. Alber, V. Bagnoud, C.R.D. Brown, R. Clarke, H. Daido, J. Fernandez, K. Flippo, S. Gaillard, C. Gauthier, M. Geissel, S. Glenzer, G. Gregori, M. Günther, K. Harres, R. Heathcote, A. Kritcher, N. Kugland, S. LePape, B. Li, M. Makita, J. Mithen, C. Niemann, F. Nürnberg, D. Offermann, A. Otten, A. Pelka, D. Riley, G. Schaumann, M. Schollmeier, J. Schütrumpf, M. Tampo, A. Tauschwitz, and An. Tauschwitz. Proton acceleration experiments and warm dense matter research using high power lasers. *Plasma Physics and Controlled Fusion*, 51(12):124039, 2009.
- [11] T. Burris-Mog, K. Harres, F. Nürnberg, S. Busold, M. Bussmann, O. Deppert, G. Hoffmeister, M. Joost, M. Sobiella, A. Tauschwitz, B. Zielbauer, V. Bagnoud, T. Herrmannsdoerfer, M. Roth, and T.E. Cowan. Laser accelerated protons captured and transported by a pulse power solenoid. *Physical Review Special Topics - Accelerators and Beams*, 14:121301, 2011.
- [12] S.V. Bulanov, T.Z. Esirkepov, V.S. Khoroshkov, A.V. Kunetsov, and F. Pegoraro. Oncological hadrontherapy with laser ion accelerators. *Physics Letters A*, 299:240–247, 2002.
- [13] S.V. Bulanov and V.S. Khoroshkov. Feasibility of using laser ion accelerators in proton therapy. *Plasma Physics Reports*, 28:453–456, 2002.
- [14] E. Fourkal, J.S. Li, M. Ding, T. Tajima, and C.-M. Ma. Particle selection for laser-accelerated proton therapy feasibility study. *Medical Physics*, 30:1660–1670, 2003.
- [15] V. Malka, S. Fritzler, E. Lefebvre, E. d’Humières, R. Ferrand, G. Grillon, C. Albaret, S. Meyroneinc, J.-P. Chambaret, A. Antonetti, and D. Hulin. Practicability of proton-therapy using compact laser systems. *Medical Physics*, 31:1587–1592, 2004.
- [16] C.-M. Ma, I. Veltchev, E. Fourkal, J.S. Li, W. Luo, J. Fan, T. Lin, and A. Pollack. Development of a laser-driven proton accelerator for cancer therapy. *Laser Physics*, 16:639–646, 2006.
- [17] K.W.D. Ledingham and W. Galster. Laser-driven particle and photon beams and some applications. *New Journal of Physics*, 12:045005, 2010.
- [18] S.A. Gaillard, T. Kluge, K.A. Flippo, M. Bussmann, B. Gall, T. Lockard, M. Geissel, D.T. Offermann, M. Schollmeier, Y. Sentoku, and T.E. Cowan. Increased laser-accelerated proton energies via direct laser-light-pressure acceleration of electrons in microcone targets. *Physics of Plasmas*, 18(5):056710, 2011.

- [19] K. Zeil, S.D. Kraft, S. Bock, M. Bussmann, T.E. Cowan, T. Kluge, J. Metzkes, T. Richter, R. Sauerbrey, and U. Schramm. The scaling of proton energies in ultrashort pulse laser plasma acceleration. *New Journal of Physics*, 12(4):045015, 2010.
- [20] K. Zeil, J. Metzkes, T. Kluge, M. Bussmann, T.E. Cowan, S.D. Kraft, R. Sauerbrey, and U. Schramm. Direct observation of prompt pre-thermal laser ion sheath acceleration. *Nature Communications*, 3:874, 2012.
- [21] E. d’Humières, E. Lefebvre, L. Gremillet, and V. Malka. Proton acceleration mechanisms in high-intensity laser interaction with thin foils. *Physics of Plasmas*, 12:062704, 2005.
- [22] T. Kluge, W. Enghardt, S.D. Kraft, U. Schramm, Y. Sentoku, K. Zeil, T.E. Cowan, R. Sauerbrey, and M. Bussmann. Efficient laser-ion acceleration from closely stacked ultrathin foils. *Physical Review E*, 82(1):016405, 2010.
- [23] T. Esirkepov, M. Yamagiwa, and T. Tajima. Laser ion-acceleration scaling laws seen in multiparametric particle-in-cell simulations. *Physical Review Letters*, 96(10):105001, 2006.
- [24] L. Yin, B.J. Albright, B.M. Hegelich, and J.C. Fernández. GeV laser ion acceleration from ultrathin targets: The laser break-out afterburner. *Laser and Particle Beams*, 24(02):291–298, 2006.
- [25] A. Macchi, F. Cattani, T.V. Liseykina, and F. Cornolti. Laser acceleration of ion bunches at the front surface of overdense plasmas. *Physical Review Letters*, 94:165003, 2005.
- [26] X.Q. Yan, C. Lin, Z.M. Sheng, Z.Y. Guo, B.C. Liu, Y.R. Lu, J.X. Fang, and J.E. Chen. Generating High-Current Monoenergetic Proton Beams by a Circularly Polarized Laser Pulse in the Phase-Stable Acceleration Regime. *Physical Review Letters*, 100(13):135003, 2008.
- [27] A.P.L. Robinson, M. Zepf, S. Kar, R.G. Evans, and C. Bellei. Radiation pressure acceleration of thin foils with circularly polarized laser pulses. *New Journal of Physics*, 10:013021, 2008.
- [28] S.G. Rykovanov, J. Schreiber, J. Meyer-ter Vehn, C. Bellei, A. Henig, H.C. Wu, and M. Geissler. Ion acceleration with ultra-thin foils using elliptically polarized laser pulses. *New Journal of Physics*, 10:113005, 2008.
- [29] A. Henig, S. Steinke, M. Schnürer, T. Sokollik, R. Hörlein, D. Kiefer, D. Jung, J. Schreiber, B.M. Hegelich, X.Q. Yan, J. Meyer-ter Vehn, T. Tajima, P.V. Nickles, W. Sandner, and D. Habs. Radiation-pressure acceleration of ion beams driven by circularly polarized laser pulses. *Physical Review Letters*, 103(24):245003, 2009.

- [30] S. Steinke, A. Henig, M. Schnürer, T. Sokollik, P.V. Nickles, D. Jung, D. Kiefer, R. Hörlein, J. Schreiber, T. Tajima, X.Q. Yan, M. Hegelich, J. Meyer-ter Vehn, W. Sandner, and D. Habs. Efficient ion acceleration by collective laser-driven electron dynamics with ultra-thin foil targets. *Laser and Particle Beams*, 28(01):215–221, 2010.
- [31] F. Dollar, C. Zülück, A.G.R. Thomas, V. Chvykov, J. Davis, G. Kalinchenko, T. Matsuoka, C. McGuffey, G.M. Petrov, L. Willingale, V. Yanovsky, A. Maksimchuk, and K. Krushelnick. Finite spot effects on radiation pressure acceleration from intense high-contrast laser interactions with thin targets. *Physical Review Letters*, 108:175005, 2012.
- [32] M. Durante and J. S. Loeffler. Charged particles in radiation oncology. *Nature Reviews Clinical Oncology*, 7:37–43, 2010.
- [33] D. Schardt, T. Elsässer, and D. Schulz-Ertner. Heavy-ion tumor therapy: Physical and radiobiological benefits. *Review of Modern Physics*, 82:383–425, 2010.
- [34] M.H. Baron, P. Pommier, V. Favrel, G. Truc, J. Balosso, J. Rochat, and ETOILE project. A “One-day survey”: As a reliable estimation of the potential recruitment for proton- and carbon-ion therapy in France. *Radiotherapy and Oncology*, 73(2):15–17, 2004.
- [35] R. Mayer, U. Mock, R. Jäger, R. Potter, C. Vutuc, H. Eiter, K. Krugmann, J. Hammer, B. Hirn, R. Hawliczek, T.H. Knocke-Abulesz, P. Lukas, E. Nechville, B. Pakisch, M. Papauschek, R. Wolfgang, W. Rhomberg, H. Sabitzer, A. Schratte-Sehn, S. Felix, I. Wedrich, and T. Auberger. Epidemiological aspects of hadron therapy: A prospective nationwide study of the Austrian project MedAustron and the Austrian Society of Radiooncology (OEGRO). *Radiotherapy and Oncology*, 73(2):24–28, 2004.
- [36] K.W.D. Ledingham, P. McKenna, and R.P. Singhal. Applications for nuclear phenomena generated by ultra-intense lasers. *Science*, 300:1107–1111, 2003.
- [37] F. Dollar, T. Matsuoka, G.M. Petrov, A.G.R. Thomas, S.S. Bulanov, V. Chvykov, J. Davis, G. Kalinchenko, C. McGuffey, L. Willingale, V. Yanovsky, A. Maksimchuk, and K. Krushelnick. Control of energy spread and dark current in proton and ion beams generated in high-contrast laser solid interactions. *Physical Review Letters*, 107:065003, 2011.
- [38] R. Prasad, S. Ter-Avetisyan, D. Doria, K.E. Quinn, L. Romagnani, P.S. Foster, C.M. Brenner, J.S. Green, P. Gallegos, M.J.V. Streeter, D.C. Carroll, O. Tresca, N.P. Dover, C.A.J. Palmer, J. Schreiber, D. Neely, Z. Najmudin, P. McKenna, M. Zepf, and M. Borghesi. Proton acceleration using 50 fs, high intensity ASTRA-Gemini laser pulses. *Nuclear Instruments and Methods in Physics Research Section A: Accelerators, Spectrometers, Detectors and Associated Equipment*, 653:113 – 115, 2011.

- [39] C.A.J. Palmer, N.P. Dover, I. Pogorelsky, M. Babzien, G.I. Dudnikova, M. Ispiriyani, M.N. Polyanskiy, J. Schreiber, P. Shkolnikov, V. Yakimenko, and Z. Najmudin. Monoenergetic proton beams accelerated by a radiation pressure driven shock. *Physical Review Letters*, 106(1):014801, 2011.
- [40] S. Buffechoux, J. Psikal, M. Nakatsutsumi, L. Romagnani, A. Andreev, K. Zeil, M. Amin, P. Antici, T. Burris-Mog, A. Compant-La-Fontaine, E. d’Humières, S. Fourmaux, S. Gaillard, F. Gobet, F. Hannachi, S. Kraft, A. Mancic, C. Plaisir, G. Sarri, M. Tarisien, T. Toncian, U. Schramm, M. Tampono, P. Audebert, O. Willi, T.E. Cowan, H. Pépin, V. Tikhonchuk, M. Borghesi, and J. Fuchs. Hot electrons transverse refluxing in ultraintense laser-solid interactions. *Physical Review Letters*, 105:015005, 2010.
- [41] M. Baumann, S.M. Bentzen, W. Doerr, M.C. Joiner, M. Saunders, I. F. Tannock, and H.D. Thames. The translational research chain: is it delivering the goods? *International Journal of Radiation Oncology\*Biophysics\*Physics*, 49(2):345 – 351, 2001.
- [42] T.E. Schmid, G. Dollinger, A. Hauptner, V. Hable, C. Greubel, S. Auer, A.A. Friedl, M. Molls, and B. Röper. No evidence for a different RBE between pulsed and continuous 20 MeV protons. *Radiation Research*, 172(5):567–574, 2009.
- [43] A. Yogo, T. Maeda, T. Hori, H. Sakaki, K. Ogura, M. Nishiuchi, A. Sagisaka, H. Kiriya, H. Okada, S. Kanazawa, T. Shimomura, Y. Nakai, M. Tanoue, F. Sasao, P.R. Bolton, M. Murakami, T. Nomura, S. Kawanishi, and K. Kondo. Measurement of relative biological effectiveness of protons in human cancer cells using a laser-driven quasimonoenergetic proton beamline. *Applied Physics Letters*, 98(5):053701–053701–3, 2011.
- [44] D. Doria, K.F. Kakolee, S. Kar, S.K. Litt, F. Fiorini, H. Ahmed, S. Green, J.C.G. Jaynes, J. Kavanagh, D. Kirby, K.J. Kirkby, C.L. Lewis, M.J. Merchant, G. Nersisyan, R. Prasad, K.M. Prise, G. Schettino, M. Zepf, and M. Borghesi. Biological effectiveness on live cells of laser driven protons at dose rates exceeding  $10^9$  Gy/s. volume 2, page 011209. AIP, 2012.
- [45] J. Bin, K. Allinger, W. Assmann, G. Dollinger, G.A. Drexler, A.A. Friedl, D. Habs, P. Hilz, R. Hoerlein, N. Humble, S. Karsch, K. Khrennikov, D. Kiefer, F. Krausz, W. Ma, D. Michalski, M. Molls, S. Raith, S. Reinhardt, B. Röper, T.E. Schmid, T. Tajima, J. Wenz, O. Zlobinskaya, J. Schreiber, and J.J. Wilkens. A laser-driven nanosecond proton source for radiobiological studies. *Applied Physics Letters*, 101(24):243701, 2012.
- [46] S.D. Kraft, C. Richter, K. Zeil, M. Baumann, E. Beyreuther, S. Bock, M. Bussmann, T.E. Cowan, Y. Dammene, W. Enghardt, U. Helbig, L. Karsch, T. Kluge, L. Laschinsky, E. Lessmann, J. Metzkes, D. Naumburger, R. Sauerbrey, M. Schürer, M. Sobiella,

- J. Woithe, U. Schramm, and J. Pawelke. Dose dependent biological damage of tumour cells by laser-accelerated proton beams. *New Journal of Physics*, 12:085003, 2010.
- [47] K. Zeil, M. Baumann, E. Beyreuther, T. Burris-Mog, T.E. Cowan, W. Enghardt, L. Karsch, S.D. Kraft, L. Laschinsky, J. Metzkes, D. Naumburger, M. Oppelt, C. Richter, R. Sauerbrey, M. Schürer, U. Schramm, and J. Pawelke. Dose-controlled irradiation of cancer cells with laser-accelerated proton pulses. *Applied Physics B*, pages 1–8, 2012.
- [48] C. Richter. *in preparation*. PhD thesis.
- [49] C. Richter, L. Karsch, Y. Dammene, S.D. Kraft, J. Metzkes, U. Schramm, M. Schürer, M. Sobiella, A. Weber, K. Zeil, and J. Pawelke. A dosimetric system for quantitative cell irradiation experiments with laser-accelerated protons. *Physics in Medicine and Biology*, 56(6):1529, 2011.
- [50] M. Oppelt. *in preparation*. PhD thesis.
- [51] K. Zeil, S.D. Kraft, A. Jochmann, F. Kroll, W. Jahr, U. Schramm, L. Karsch, J. Pawelke, B. Hidding, and G. Pretzler. Absolute response of Fuji imaging plate detectors to picosecond-electron bunches. *Review of Scientific Instruments*, 81(1):013307, 2010.
- [52] A. Buck, K. Zeil, A. Popp, K. Schmid, A. Jochmann, S.D. Kraft, B. Hidding, T. Kudyakov, C.M.S. Sears, L. Veisz, S. Karsch, J. Pawelke, R. Sauerbrey, T. Cowan, F. Krausz, and U. Schramm. Absolute charge calibration of scintillating screens for relativistic electron detection. *Review of Scientific Instruments*, 81(3):033301, 2010.
- [53] L. Karsch, E. Beyreuther, T. Burris-Mog, S.D. Kraft, C. Richter, K. Zeil, and J. Pawelke. Dose rate dependence for different dosimeters and detectors: TLD, OSL, EBT films, and diamond detectors. *Medical Physics*, 39(5):2447–2455, 2012.
- [54] L. Karsch, C. Richter, and J. Pawelke. Experimental investigation of the collection efficiency of a PTW Roos ionization chamber irradiated with pulsed beams at high pulse dose with different pulse lengths. *Zeitschrift für Medizinische Physik*, 21(1):4–10, 2011.
- [55] G. Pretzler, A. Kasper, and K.J. Witte. Angular chirp and tilted light pulses in CPA lasers. *Applied Physics B: Lasers and Optics*, 70:1–9, 2000.
- [56] J. Metzkes, T.E. Cowan, L. Karsch, S.D. Kraft, J. Pawelke, C. Richter, T. Richter, K. Zeil, and U. Schramm. Preparation of laser-accelerated proton beams for radiobiological applications. *Nuclear Instruments and Methods in Physics Research Section A: Accelerators, Spectrometers, Detectors and Associated Equipment*, 653(1):172–175, 2011.



- [57] J. Metzkes, L. Karsch, S.D. Kraft, J. Pawelke, C. Richter, M. Schürer, M. Sobiella, N. Stiller, K. Zeil, and U. Schramm. A scintillator-based online detector for the angularly resolved measurement of laser-accelerated proton spectra. *Review of Scientific Instruments*, 83(12):123301–123301–7, 2012.
- [58] F. Nürnberg, M. Schollmeier, E. Brambrink, A. Blažević, D.C. Carroll, K. Flippo, D.C. Gautier, M. Geißel, K. Harres, B.M. Hegelich, et al. Radiochromic film imaging spectroscopy of laser-accelerated proton beams. *Review of Scientific Instruments*, 80:033301, 2009.
- [59] T. Richter. Entwicklung zweier Spektrometer für laserbeschleunigte Protonenstrahlen. Master's thesis, TU Dresden, 2009.
- [60] J Metzkes. Charakterisierung laserbeschleunigter Protonen und Elektronen. Master's thesis, Martin-Luther-Universität Halle-Wittenberg, 2009.
- [61] R. Cambria, J. Hérault, N. Brassart, M. Silari, and P. Chauvel. Proton beam dosimetry: a comparison between the faraday cup and an ionization chamber. *Physics in Medicine and Biology*, 42:1185, 1997.
- [62] A. Yogo, K. Sato, M. Nishikino, M. Mori, T. Teshima, H. Numasaki, M. Murakami, Y. Demizu, S. Akagi, S. Nagayama, K. Ogura, A. Sagisaka, S. Orimo, M. Nishiuchi, A.S. Pirozhkov, M. Ikegami, M. Tampo, H. Sakaki, M. Suzuki, I. Daito, Y. Oishi, H. Sugiyama, H. Kiriyama, H. Okada, S. Kanazawa, S. Kondo, T. Shimomura, Y. Nakai, M. Tanoue, H. Sasao, D. Wakai, P.R. Bolton, and H. Daido. Application of laser-accelerated protons to the demonstration of DNA double-strand breaks in human cancer cells. *Applied Physics Letters*, 94:181502, 2009.
- [63] U. Kasten-Pisula, A. Menegakis, I. Brammer, K. Borgmann, W.Y. Mansour, S. Degenhardt, M. Krause, A. Schreiber, J. Dahm-Daphi, C. Petersen, E. Dikomey, and M. Baumann. The extreme radiosensitivity of the squamous cell carcinoma SKX is due to a defect in double-strand break repair. *Radiotherapy and Oncology*, 90:257–264, 2009.
- [64] E. Beyreuther, E. Lessmann, J. Pawelke, and S. Pieck. DNA double strand breaks signaling: X-ray energy dependence residual co-localised foci of  $\gamma$ -H2AX and 53BP1. *International Journal of Radiation Biology*, 85:1042–1050, 2009.
- [65] L. Laschinsky, M. Baumann, E. Beyreuther, W. Enghardt, M. Kaluza, L. Karsch, E. Lessmann, D. Naumburger, M. Nicolai, C. Richter, R. Sauerbrey, H.-P. Schlenvoigt, and J. Pawelke. Radiobiological effectiveness of laser accelerated electrons in comparison to electron beams from a conventional linear accelerator. *Journal of Radiation Research*, 53(3):395–403, 2012.

- [66] A. Menegakis, A. Yaromina, W. Eicheler, A. Dörfler, B. Beuthien-Baumann, H.D. Thames, M. Baumann, and Krause M. Prediction of clonogenic cell survival curves based on the number of residual DNA double strand breaks measured by  $\gamma$ H2AX staining. *International Journal of Radiation Biology*, 85:1032–1041, 2009.
- [67] E.P. Rogakou, D.R. Pilch, A.H. Orr, V.S. Ivanova, and W.M. Bonner. DNA double-stranded breaks induce histone H2AX phosphorylation on serine 139. *Journal of Biological Chemistry*, 273(10):5858–5868, 1998.
- [68] I. Rappold, K. Iwabuchi, T. Date, and J. Chen. Tumor suppressor p53 binding protein 1 (53bp1) is involved in DNA damage signaling pathways. *The Journal of Cell Biology*, 153(3):613–620, 2001.
- [69] O. Zlobinskaya, G. Dollinger, D. Michalski, V. Hable, C. Greubel, G. Du, G. Multhoff, B. Röper, M. Molls, and T.E. Schmid. Induction and repair of DNA double-strand breaks assessed by gamma-H2AX foci after irradiation with pulsed or continuous proton beams. *Radiation and Environmental Biophysics*, 51:23–32, 2012.
- [70] Dan Haberberger, Sergei Tochitsky, Frederico Fiuza, Chao Gong, Ricardo A. Fonseca, Luis O. Silva, Warren B. Mori, and Chan Joshi. Collisionless shocks in laser-produced plasma generate monoenergetic high-energy proton beams. *Nature Physics*, 8(1):95–99, 2012.
- [71] F. Fiuza, A. Stockem, E. Boella, R.A. Fonseca, L. O. Silva, D. Haberberger, S. Tochitsky, C. Gong, W. B. Mori, and C. Joshi. Laser-driven shock acceleration of monoenergetic ion beams. *ArXiv e-prints*, 2012.
- [72] S.P. Hatchett, C.G. Brown, T.E. Cowan, E.A. Henry, J.S. Johnson, M.H. Key, J.A. Koch, A.B. Langdon, B.F. Lasinski, R.W. Lee, A.J. Mackinnon, D.M. Pennington, M.D. Perry, T.W. Phillips, M. Roth, T.C. Sangster, M.S. Singh, R.A. Snavely, M.A. Stoyer, S.C. Wilks, and K. Yasuike. Electron, photon, and ion beams from the relativistic interaction of Petawatt laser pulses with solid targets. *Physics of Plasmas*, 7(5):2076–2082, 2000.
- [73] J. Fuchs, P. Antici, E. d’Humieres, E. Lefebvre, M. Borghesi, E. Brambrink, C.A. Cecchetti, M. Kaluza, V. Malka, M. Manclossi, S. Meyroneinc, P. Mora, J. Schreiber, T. Toncian, H. Pepin, and P. Audebert. Laser-driven proton scaling laws and new paths towards energy increase. *Nature Physics*, 2:48, 2006.
- [74] L. Robson, P.T. Simpson, R.J. Clarke, K.W.D. Ledingham, F. Lindau, Lundh O., T. McCanny, P. Mora, D. Neely, C.-G. Wahlström, M. Zepf, and P. McKenna. Scaling of proton acceleration driven by Petawatt-laser-plasma interactions. *Nature Physics*, 3:58, 2006.

- [75] J. Schreiber, F. Bell, F. Grüner, U. Schramm, M. Geissler, M. Schnürer, S. Ter-Avetisyan, B.M. Hegelich, J. Cobble, E. Brambrink, J. Fuchs, P. Audebert, and D. Habs. Analytical model for ion acceleration by high-intensity laser pulses. *Physical Review Letters*, 97, 2006.
- [76] S. Tochitsky and M. Hegelich. Summary report of working group 6: Laser-plasma acceleration of ions. *AIP Conference Proceedings*, 1507(1):231–239, 2012.
- [77] H. Daido, M. Nishiuchi, and A.S. Pirozhkov. Review of laser-driven ion sources and their applications. *Reports on Progress in Physics*, 75(5):056401, 2012.
- [78] H. Schworer, S. Pfotenhauer, O. Jäckel, K.-U. Amthor, B. Liesfeld, W. Ziegler, R. Sauerbrey, K.W.D. Ledingham, and T. Esirkepov. Laser-plasma acceleration of quasi-monoenergetic protons from microstructured targets. *Nature*, 439:445, 2006.
- [79] S.M. Pfotenhauer, O. Jäckel, A. Sachtleben, J. Polz, W. Ziegler, H.-P. Schlenvoigt, K.-U. Amthor, M.C. Kaluza, K.W.D. Ledingham, R. Sauerbrey, P. Gibbon, A.P.L. Robinson, and H. Schworer. Spectral shaping of laser generated proton beams. *New Journal of Physics*, 10(3):033034, 2008.
- [80] B.M. Hegelich, B.J. Albright, J. Cobble, K. Flippo, S. Letzring, M. Paffett, H. Ruhl, J. Schreiber, R.K. Schulze, and J.C. Fernandez. Laser acceleration of quasi-monoenergetic MeV ion beams. *Nature*, 439:441–444, 2006.
- [81] T. Kluge, W. Enghardt, S.D. Kraft, U. Schramm, K. Zeil, T.E. Cowan, and M. Bussmann. Enhanced laser ion acceleration from mass-limited foils. *Physics of Plasmas*, 17:123103, 2010.
- [82] M. Kaluza, J. Schreiber, M.I.K. Santala, G. Tsakiris, K. Eidmann, J. Meyer-ter Vehn, and K. Witte. Influence of the laser prepulse on proton acceleration in thin-foil experiments. *Physical Review Letters*, 93:045003, 2004.
- [83] K. Markey, P. McKenna, C.M. Brenner, D.C. Carroll, M.M. Günther, K. Harres, S. Kar, K. Lancaster, F. Nürnberg, M.N. Quinn, A.P.L. Robinson, M. Roth, M. Zepf, and D. Neely. Spectral enhancement in the double pulse regime of laser proton acceleration. *Physical Review Letters*, 105:195008, 2010.
- [84] J. Fuchs, C.A. Cecchetti, M. Borghesi, T. Grismayer, E. d’Humières, P. Antici, S. Atzeni, P. Mora, A. Pipahl, L. Romagnani, A. Schiavi, Y. Sentoku, T. Toncian, P. Audebert, and O. Willi. Laser-foil acceleration of high-energy protons in small-scale plasma gradients. *Physical Review Letters*, 99:015002, 2007.
- [85] J. Rassuchine, E. d’Humières, S.D. Baton, P. Guillou, M. Koenig, M. Chahid, F. Perez, J. Fuchs, P. Audebert, R. Kodama, M. Nakatsutsumi, N. Ozaki, D. Batani, A. Morace, R. Redaelli, L. Gremillet, C. Rousseaux, F. Dorchies, C. Fourment, J.J. Santos,

- J. Adams, G. Korgan, S. Malekos, S.B. Hansen, R. Shepherd, K. Flippo, S. Gaillard, Y. Sentoku, and T.E. Cowan. Enhanced hot-electron localization and heating in high-contrast ultraintense laser irradiation of micro-cone targets. *Physical Review E*, 79:036408, 2009.
- [86] T. Kluge, S.A. Gaillard, K.A. Flippo, T. Burris-Mog, W. Enghardt, B. Gall, M. Geissel, A. Helm, S.D. Kraft, T. Lockard, J. Metzkes, D.T. Offermann, M. Schollmeier, U. Schramm, K. Zeil, M. Bussmann, and T.E. Cowan. High proton energies from cone targets: electron acceleration mechanisms. *New Journal of Physics*, 14(2):023038, 2012.
- [87] B. Qiao, M. Zepf, M. Borghesi, B. Dromey, M. Geissler, A. Karmakar, and P. Gibbon. Radiation-pressure acceleration of ion beams from nanofoil targets: The leaky light-sail regime. *Physical Review Letters*, 105(15):155002, 2010.
- [88] V. Yanovsky, V. Chvykov, G. Kalinchenko, P. Rousseau, T. Planchon, T. Matsuoka, A. Maksimchuk, J. Nees, G. Cheriaux, G. Mourou, and K. Krushelnick. Ultra-high intensity 300 TW laser at 0.1 Hz repetition rate. *Optics Express*, 16(3):2109–2114, 2008.
- [89] P. Gibbon. *Short pulse laser interactions with matter: An introduction*. Number ISBN 1-86094-135-4. Imperial College Press London, 2005.
- [90] P. Mulser and D. Bauer. *High power laser-matter interaction*. Number ISBN 978-3-540-50669-0. Springer-Verlag Berlin Heidelberg, 2010.
- [91] W. Kruer. *The physics of laser plasma interactions*, volume 73. Reading, MA, Addison-Wesley Publishing Co. (Frontiers in Physics.), 1988.
- [92] T. Tajima and J.M. Dawson. Laser electron accelerator. *Physical Review Letters*, 43(4):267–270, 1979.
- [93] S.P.D. Mangles, C.D. Murphy, Z. Najmudin, A.G.R. Thomas, J.L. Collier, A.E. Dangor, E.J. Divall, P.S. Foster, J.G. Gallacher, C.J. Hooker, D.A. Jaroszynski, A.J. Langley, W.B. Mori, P.A. Norreys, F.S. Tsung, R. Viskup, B.R. Walton, and K. Krushelnick. Monoenergetic beams of relativistic electrons from intense laser-plasma interactions. *Nature*, 431(7008):535–538, 2004.
- [94] J. Faure, Y. Glinec, A. Pukhov, S. Kiselev, S. Gordienko, E. Lefebvre, J.-P. Rousseau, F. Burgy, and V. Malka. A laser-plasma accelerator producing monoenergetic electron beams. *Nature*, 431(7008):541–544, 2004.
- [95] C.G.R. Geddes, Cs. Toth, J. van Tilborg, E. Esarey, C.B. Schroeder, D. Bruhwiler, C. Nieter, J. Cary, and W.P. Leemans. High-quality electron beams from a laser wakefield accelerator using plasma-channel guiding. *Nature*, 431(7008):538–541, 2004.

- [96] F. Brunel. Not-so-resonant, resonant absorption. *Physical Review Letters*, 59:52–55, 1987.
- [97] W.L. Kruer and K. Estabrook.  $J \times B$  heating by very intense laser light. *Physics of Fluids*, 28:430, 1985.
- [98] S.C. Wilks, W.L. Kruer, M. Tabak, and A.B. Langdon. Absorption of ultra-intense laser pulses. *Physical Review Letters*, 69(9):1383, 1992.
- [99] P. Mulser, D. Bauer, and H. Ruhl. Collisionless laser-energy conversion by anharmonic resonance. *Physical Review Letters*, 101:225002, 2008.
- [100] J.E. Crow, P.L. Auer, and J.E. Allen. The expansion of a plasma into a vacuum. *Journal of Plasma Physics*, 14:65–76, 1975.
- [101] P. Mora. Plasma expansion into a vacuum. *Physical Review Letters*, 90:185002, 2003.
- [102] M. Lontano and M. Passoni. Electrostatic field distribution at the sharp interface between high density matter and vacuum. *Physics of Plasmas*, 13(4):042102, 2006.
- [103] M. Passoni and M. Lontano. Theory of light-ion acceleration driven by a strong charge separation. *Physical Review Letters*, 101:115001, 2008.
- [104] M. Passoni, L. Bertagna, and A. Zani. Target normal sheath acceleration: theory, comparison with experiments and future perspectives. *New Journal of Physics*, 12(4):045012, 2010.
- [105] A.V. Gurevich, L.V. Pariiskaia, and L.P. Pitaevskii. Self-similar motion of a rarefied plasma (nonlinear kinetic equation of self-similar motion of rarefied collisionless electron-ion plasma). *ZHURNAL EKSPERIMENTAL'NOI I TEORETICHESKOI FIZIKI*, 49:647–654, 1965.
- [106] T. Grismayer, P. Mora, J.C. Adam, and A. Héron. Electron kinetic effects in plasma expansion and ion acceleration. *Physical Review E*, 77:066407, 2008.
- [107] P. Mora and T. Grismayer. Rarefaction acceleration and kinetic effects in thin-foil expansion into a vacuum. *Physical Review Letters*, 102:145001, 2009.
- [108] J. Fuchs, Y. Sentoku, E. d’Humières, T.E. Cowan, J. Cobble, P. Audebert, A. Kemp, A. Nikroo, P. Antici, E. Brambrink, A. Blazevic, E.M. Campbell, J.C. Fernández, J.-C. Gauthier, M. Geissel, M. Hegelich, S. Karsch, H. Popescu, N. Renard-LeGalloudec, M. Roth, J. Schreiber, R. Stephens, and H. Pépin. Comparative spectra and efficiencies of ions laser-accelerated forward from the front and rear surfaces of thin solid foils. *Physics of Plasmas*, 14(5):053105, 2007.

- [109] A.J. Kemp and H. Ruhl. Multispecies ion acceleration off laser-irradiated water droplets. *Physics of Plasmas*, 12(3):033105, 2005.
- [110] J. Psikal, V.T. Tikhonchuk, J. Limpouch, A.A. Andreev, and A.V. Brantov. Ion acceleration by femtosecond laser pulses in small multispecies targets. *Physics of Plasmas*, 15:053102, 2008.
- [111] T. Toncian, M. Borghesi, J. Fuchs, E. d’Humieres, P. Antici, P. Audebert, E. Brambrink, C.A. Cecchetti, A. Pipahl, L. Romagnani, and O. Willi. Ultrafast laser-driven microlens to focus and energy-select mega-electron volt protons. *Science*, 312(410):410–413, 2006.
- [112] O. Lundh, F. Lindau, A. Persson, C.G. Wahlström, P. McKenna, and D. Batani. Influence of shock waves on laser-driven proton acceleration. *Physical Review E*, 76:26404, 2007.
- [113] T. Ceccotti, A. Lévy, H. Popescu, F. Réau, P. D’Oliveira, P. Monot, J. P. Geindre, E. Lefebvre, and Ph. Martin. Proton acceleration with high-intensity ultrahigh-contrast laser pulses. *Physical Review Letters*, 99:185002, 2007.
- [114] J.R. Davies. Laser absorption by overdense plasmas in the relativistic regime. *Plasma Physics and Controlled Fusion*, 51(1):014006, 2009.
- [115] T. Kluge. *Enhanced laser ion acceleration from solids*. PhD thesis, TU Dresden, 2012.
- [116] T. Kaluza. *Characterisation of Laser-Accelerated Proton Beams*. PhD thesis, TU München, 2004.
- [117] T. Kluge, T. Cowan, A. Debus, U. Schramm, K. Zeil, and M. Bussmann. Electron temperature scaling in laser interaction with solids. *Physical Review Letters*, 107(20):205003, 2011.
- [118] D. Neely, P. Foster, A. Robinson, F. Lindau, O. Lundh, A. Persson, C.-G. Wahlström, and P. McKenna. Enhanced proton beams from ultrathin targets driven by high contrast laser pulses. *Applied Physics Letters*, 89:021502, 2006.
- [119] A.S. Pirozhkov, M. Mori, A. Yogo, H. Kiriya, K. Ogura, A. Sagisaka, J.-L. Ma, S. Orimo, M. Nishiuchi, H. Sugiyama, T.Zh. Esirkepov, S.V. Bulanov, H. Okada, S. Kondo, S. Kanazawa, Y. Nakai, A. Akutsu, T. Motomura, M. Tanoue, T. Shimomura, M. Ikegami, T. Shirai, Y. Iwashita, A. Noda, I.W. Choi, S.K. Lee, J. Lee, Y. Oishi, T. Kimura, T. Tajima, and H. Daido. Laser-driven proton acceleration and plasma diagnostics with J-KAREN laser. volume 7354, page 735414. SPIE, 2009.
- [120] S. Steinke and T. Sokollik. private communication, 2009.

- [121] S. Fritzler, V. Malka, G. Grillon, J.P. Rousseau, F. Burgy, E. Lefebvre, E. d'Humieres, P. McKenna, and K.W.D. Ledingham. Proton beams generated with high-intensity lasers: Applications to medical isotope production. *Applied Physics Letters*, 83:3039, 2003.
- [122] I. Spencer, K.W.D. Ledingham, P. McKenna, T. McCanny, R.P. Singhal, P.S. Foster, D. Neely, A.J. Langley, E.J. Divall, C.J. Hooker, R.J. Clarke, P.A. Norreys, E.L. Clark, K. Krushelnick, and J.R. Davies. Experimental study of proton emission from 60-fs, 200-mJ high-repetition-rate tabletop-laser pulses interacting with solid targets. *Physical Review E*, 67(4):046402, 2003.
- [123] O. Jäckel. *Characterization of ion acceleration with relativistic laser pulses*. PhD thesis, FSU Jena, 2009.
- [124] K. Ogura, M. Nishiuchi, A.S. Pirozhkov, T. Tanimoto, A. Sagisaka, T.Zh. Esirkepov, M. Kando, T. Shizuma, T. Hayakawa, H. Kiriya, T. Shimomura, S. Kondo, S. Kanazawa, Y. Nakai, H. Sasao, F. Sasao, Y. Fukuda, H. Sakaki, M. Kanasaki, A. Yogo, S.V. Bulanov, P.R. Bolton, and K. Kondo. Proton acceleration to 40 MeV using a high intensity, high contrast optical parametric chirped-pulse amplification/Ti:sapphire hybrid laser system. *Optics Letters*, 37(14):2868–2870, 2012.
- [125] S.D. Kraft. private communication, 2012.
- [126] A.J. Mackinnon, Y. Sentoku, P.K. Patel, D.W. Price, S. Hatchett, M.H. Key, C. Andersen, R. Snavely, and R.R. Freeman. Enhancement of proton acceleration by hot-electron recirculation in thin foils irradiated by ultraintense laser pulses. *Physical Review Letters*, 88:215006, 2002.
- [127] R.A. Snavely, M.H. Key, S.P. Hatchett, T.E. Cowan, M. Roth, T.W. Phillips, M.A. Stoyer, E.A. Henry, T.C. Sangster, M.S. Singh, S.C. Wilks, A. MacKinnon, A. Offenberger, D.M. Pennington, K. Yasuike, A.B. Langdon, B.F. Lasinski, J. Johnson, M.D. Perry, and E.M. Campbell. Intense high-energy proton beams from Petawatt-laser irradiation of solids. *Physical Review Letters*, 85:2945, 2000.
- [128] M. Zepf, E.L. Clark, K. Krushelnick, F.N. Beg, C. Escoda, A.E. Dangor, M.I.K. Santala, I.F. Tatarakis, M. Watts, P.A. Norreys, R.J. Clarke, J.R. Davies, M.A. Sinclair, R.D. Edwards, T.J. Goldsack, I. Spencer, and K.W.D. Ledingham. Fast particle generation and energy transport in laser-solid interactions. *Physics of Plasmas*, 8:2323, 2001.
- [129] K.A. Flipppo, J. Workman, D.C. Gautier, S. Letzring, R.P. Johnson, and T. Shimada. Scaling laws for energetic ions from the commissioning of the new Los Alamos National Laboratory 200 TW Trident laser. *Review of Scientific Instruments*, 79:10E534, 2008.

- [130] S. Gaillard and K.A. Flippo. private communication, 2009.
- [131] M. Roth. private communication, 2009.
- [132] M. Schnürer, A.A. Andreev, S. Steinke, T. Sokollik, T. Paasch-Colberg, P.V. Nickles, A. Henig, D. Jung, D. Kiefer, R. Hörlein, J. Schreiber, T. Tajima, D. Habs, and W. Sandner. Comparison of femtosecond laser-driven proton acceleration using nanometer and micrometer thick target foils. *Laser and Particle Beams*, 29(04):437–446, 2011.
- [133] S. Buffechoux. *Augmentation de l'énergie des faisceaux de protons accélérés par laser ultra-intense et étude caractéristique des faisceaux accélérés par laser ultra-court*. PhD thesis, L'université Paris sud XI, 2011.
- [134] J. Schreiber. *Ion Acceleration driven by High-Intensity Laser Pulses*. PhD thesis, LMU München, 2006.
- [135] Y. Sentoku and A.J. Kemp. Numerical methods for particle simulations at extreme densities and temperatures: Weighted particles, relativistic collisions and reduced currents. *Journal of Computational Physics*, 227(14):6846, 2008.
- [136] The PICLS code was run by T. Kluge. The input parameters of the simulations closely resembling the experiments performed in this thesis and the interpretation of the results were developed in close collaboration.
- [137] O. Lundh, Y. Glinec, C. Homann, F. Lindau, A. Persson, C.G. Wahlström, D.C Carroll, and P. McKenna. Active steering of laser-accelerated ion beams. *Applied Physics Letters*, 92:011504, 2008.
- [138] S. Akturk, X. Gu, E. Zeek, and R. Trebino. Pulse-front tilt caused by spatial and temporal chirp. *Optics Express*, 12(19):4399–4410, 2004.
- [139] A. Popp, J. Vieira, J. Osterhoff, Zs. Major, R. Hörlein, M. Fuchs, R. Weingartner, T.P. Rowlands-Rees, M. Marti, R.A. Fonseca, S.F. Martins, L.O. Silva, S.M. Hooker, F. Krausz, F. Grüner, and S. Karsch. All-optical steering of laser-wakefield-accelerated electron beams. *Physical Review Letters*, 105(21):215001, 2010.
- [140] A.G. Kostenbauder. Ray-pulse matrices: a rational treatment for dispersive optical systems. *Quantum Electronics, IEEE Journal of*, 26(6):1148–1157, 1990.
- [141] A. Debus. private communication, 2012.
- [142] G. Pretzler. Höchstleistungs-Kurzpulslaser. *Sommersemester, LMU München*, 2000.
- [143] F. Kroll. Aufbau und Charakterisierung eines Vakuumaufkorrelators zur Messung von ultrakurzen Hochleistungslaserpulsen. Master's thesis, TFH Wildau, 2009.



- [144] M.I.K. Santala, M. Zepf, I. Watts, F.N. Beg, E. Clark, M. Tatarakis, K. Krushelnick, A.E. Dangor, T. McCanny, I. Spencer, R.P. Singhal, K.W.D. Ledingham, S.C. Wilks, A.C. Machacek, J.S. Wark, R. Allott, R.J. Clarke, and P.A. Norreys. Effect of the plasma density scale length on the direction of fast electrons in relativistic laser-solid interactions. *Physical Review Letters*, 84:1459–1462, 2000.
- [145] F. Brandl, G. Pretzler, D. Habs, and E. Fill. Cerenkov radiation diagnostics of hot electrons generated by fs-laser interaction with solid targets. *Europhysics Letters*, 61(5):632, 2003.
- [146] S.D. Baton, J.J. Santos, F. Amiranoff, H. Popescu, L. Gremillet, M. Koenig, E. Martinnoli, O. Guilbaud, C. Rousseaux, M. Rabec Le Gloahec, T. Hall, D. Batani, E. Perelli, F. Scianitti, and T.E. Cowan. Evidence of ultrashort electron bunches in laser-plasma interactions at relativistic intensities. *Physical Review Letters*, 91(10):105001, 2003.
- [147] S. Ter-Avetisyan, M. Schnürer, T. Sokollik, P.V. Nickles, W. Sandner, H.R. Reiss, J. Stein, D. Habs, T. Nakamura, and K. Mima. Proton acceleration in the electrostatic sheaths of hot electrons governed by strongly relativistic laser-absorption processes. *Physical Review E*, 77:016403, 2008.
- [148] D.C. Carroll, O. Tresca, R. Prasad, L. Romagnani, P.S. Foster, P. Gallegos, S. Ter-Avetisyan, J.S. Green, M.J.V. Streeter, N. Dover, C.A.J. Palmer, C.M. Brenner, F.H. Cameron, K.E. Quinn, J. Schreiber, A.P.L. Robinson, T. Baeva, M.N. Quinn, X.H. Yuan, Z. Najmudin, M. Zepf, D. Neely, M. Borghesi, and P. McKenna. Carbon ion acceleration from thin foil targets irradiated by ultrahigh-contrast, ultraintense laser pulses. *New Journal of Physics*, 12(4):045020, 2010.
- [149] O. Jäckel, J. Polz, S.M. Pfotenhauer, H.-P. Schlenvoigt, H. Schwöerer, and M.C. Kaluza. All-optical measurement of the hot electron sheath driving laser ion acceleration from thin foils. *New Journal of Physics*, 12(10):103027, 2010.
- [150] P. Antici, J. Fuchs, M. Borghesi, L. Gremillet, T. Grismayer, Y. Sentoku, E. d’Humières, C.A. Cecchetti, A. Mančić, A.C. Pipahl, T. Toncian, O. Willi, P. Mora, and P. Audebert. Hot and cold electron dynamics following high-intensity laser matter interaction. *Physical Review Letters*, 101:105004, 2008.
- [151] S. Mondal, A.D. Lad, S. Ahmed, V. Narayanan, J. Pasley, P.P. Rajeev, A.P.L. Robinson, and G.R. Kumar. Doppler spectrometry for ultrafast temporal mapping of density dynamics in laser-induced plasmas. *Physical Review Letters*, 105:105002, 2010.
- [152] A.S. Pirozhkov, I.W. Choi, J.H. Sung, S.K. Lee, T. J. Yu, T.M. Jeong, I.J. Kim, N. Hafz, C.M. Kim, K.H. Pae, Y.-C. Noh, D.-K. Ko, J. Lee, A.P.L. Robinson, P. Foster, S. Hawkes, M. Streeter, C. Spindloe, P. McKenna, D.C. Carroll, C.-G. Wahlström,

- M. Zepf, D. Adams, B. Dromey, K. Markey, S. Kar, Y.T. Li, M.H. Xu, H. Nagatomo, M. Mori, A. Yogo, H. Kiriya, K. Ogura, A. Sagisaka, S. Orimo, M. Nishiuichi, H. Sugiyama, T.Zh. Esirkepov, H. Okada, S. Kondo, S. Kanazawa, Y. Nakai, A. Akutsu, T. Motomura, M. Tanoue, T. Shimomura, M. Ikegami, I. Daito, M. Kando, T. Kameshima, P. Bolton, S.V. Bulanov, H. Daido, and D. Neely. Diagnostic of laser contrast using target reflectivity. *Applied Physics Letters*, 94(24):241102, 2009.
- [153] A.J. Mackinnon, M. Borghesi, S. Hatchett, M.H. Key, P.K. Patel, H. Campbell, A. Schiavi, R. Snavely, S.C. Wilks, and O. Willi. Effect of plasma scale length on multi-MeV proton production by intense laser pulses. *Physical Review Letters*, 86:1769, 2001.
- [154] A. Lévy, R. Nuter, T. Ceccotti, P. Combis, M. Drouin, L. Gremillet, P. Monot, H. Popescu, F. Réau, E. Lefebvre, and P. Martin. Effect of a nanometer scale plasma on laser-accelerated ion beams. *New Journal of Physics*, 11(9):093036, 2009.
- [155] P. McKenna, D.C. Carroll, O. Lundh, F. Nürnberg, K. Markey, S. Bandyopadhyay, D. Batani, R.G. Evans, R. Jafer, S. Kar, D. Neely, D. Pepler, M.N. Quinn, R. Redaelli, M. Roth, C.-G. Wahlström, X.H. Yuan, and M. Zepf. Effects of front surface plasma expansion on proton acceleration in ultraintense laser irradiation of foil targets. *Laser and Particle Beams*, 26(04):591–596, 2008.
- [156] A.A. Andreev, R. Sonobe, S. Kawata, S. Miyazaki, K. Sakai, K. Miyauchi, T. Kikuchi, K. Platonov, and K. Nemoto. Effect of a laser prepulse on fast ion generation in the interaction of ultra-short intense laser pulses with a limited-mass foil target. *Plasma Physics and Controlled Fusion*, 48(11):1605, 2006.
- [157] Y. Sentoku, T.E. Cowan, A. Kemp, and H. Ruhl. High energy proton acceleration in interaction of short laser pulse with dense plasma target. *Physics of Plasmas*, 10:2009, 2003.
- [158] P. McKenna, F. Lindau, O. Lundh, D. Neely, A. Persson, and C.-G. Wahlström. High-intensity laser-driven proton acceleration: influence of pulse contrast. *Philosophical Transactions of the Royal Society A: Mathematical, Physical and Engineering Sciences*, 364(1840):711–723, 2006.
- [159] T. Toncian, M. Swantusch, M. Toncian, O. Willi, A.A. Andreev, and K.Y. Platonov. Optimal proton acceleration from lateral limited foil sections and different laser pulse durations at relativistic intensity. *Physics of Plasmas*, 18(4):043105, 2011.
- [160] F. Lindau, O. Lundh, A. Persson, P. McKenna, K. Osvay, D. Batani, and C.G. Wahlström. Laser-accelerated protons with energy-dependent beam direction. *Physical Review Letters*, 95:175002, 2005.

- [161] K. Eidmann, J. Meyer-ter Vehn, T. Schlegel, and S. Hüller. Hydrodynamic simulation of subpicosecond laser interaction with solid-density matter. *Physical Review E*, 62:1202–1214, 2000.
- [162] K.B. Wharton, C.D. Boley, A.M. Komashko, A.M. Rubenchik, J. Zweiback, J. Crane, G. Hays, T.E. Cowan, and T. Ditmire. Effects of nonionizing prepulses in high-intensity laser-solid interactions. *Physical Review E*, 64:025401, 2001.
- [163] O. Klimo, J. Psikal, J. Limpouch, J. Proska, F. Novotny, T. Ceccotti, V. Floquet, and S. Kawata. Short pulse laser interaction with micro-structured targets: simulations of laser absorption and ion acceleration. *New Journal of Physics*, 13(5):053028, 2011.
- [164] L. Willingale, S.R. Nagel, A.G.R. Thomas, C. Bellei, R.J. Clarke, A.E. Dangor, R. Heathcote, M.C. Kaluza, C. Kamperidis, S. Kneip, K. Krushelnick, N. Lopes, S.P.D. Mangles, W. Nazarov, P.M. Nilson, and Z. Najmudin. Characterization of high-intensity laser propagation in the relativistic transparent regime through measurements of energetic proton beams. *Physical Review Letters*, 102:125002, 2009.
- [165] T. Bartal, M.E. Foord, C. Bellei, M. H. Key, K.A. Flippo, S.A. Gaillard, D.T. Offermann, P.K. Patel, L.C. Jarrott, D.P. Higginson, M. Roth, A. Otten, D. Kraus, R.B. Stephens, H.S. McLean, E.M. Giraldez, M.S. Wei, D.C. Gautier, and F.N. Beg. Focusing of short-pulse high-intensity laser-accelerated proton beams. *Nature Physics*, advance online publication, 2011.
- [166] J. Limpouch, J. Psikal, A.A. Andreev, K. YU. Platonov, and S. Kawata. Enhanced laser ion acceleration from mass-limited targets. *Laser and Particle Beams*, 26(02):225–234, 2008.
- [167] T. Sokollik, T. Paasch-Colberg, K. Gorling, U. Eichmann, M. Schnürer, S. Steinke, P.V. Nickles, A. Andreev, and W. Sandner. Laser-driven ion acceleration using isolated mass-limited spheres. *New Journal of Physics*, 12(11):113013, 2010.
- [168] S. Ter-Avetisyan, M. Schnürer, P.V. Nickles, M. Kalashnikov, E. Risse, T. Sokollik, W. Sandner, A. Andreev, and V. Tikhonchuk. Quasimonoeenergetic deuteron bursts produced by ultraintense laser pulses. *Physical Review Letters*, 96:145006, 2006.
- [169] A. Henig, D. Kiefer, M. Geissler, S.G. Rykovanov, R. Ramis, R. Hörlein, J. Osterhoff, Zs. Major, L. Veisz, S. Karsch, F. Krausz, D. Habs, and J. Schreiber. Laser-driven shock acceleration of ion beams from spherical mass-limited targets. *Physical Review Letters*, 102:095002, 2009.
- [170] T. Sokollik, M. Schnürer, S. Steinke, P. V. Nickles, W. Sandner, M. Amin, T. Toncian, O. Willi, and A.A. Andreev. Directional laser-driven ion acceleration from microspheres. *Physical Review Letters*, 103:135003, 2009.

- [171] O. Tresca, D.C. Carroll, X.H. Yuan, B. Aurand, V. Bagnoud, C.M. Brenner, M. Coury, J. Fils, R.J. Gray, T. Kühn, C. Li, Y.T. Li, X.X. Lin, M.N. Quinn, R.G. Evans, B. Zielbauer, M. Roth, D. Neely, and P. McKenna. Controlling the properties of ultraintense laser-proton sources using transverse refluxing of hot electrons in shaped mass-limited targets. *Plasma Physics and Controlled Fusion*, 53(10):105008, 2011.
- [172] P. McKenna, K.W.D. Ledingham, J.M. Yang, L. Robson, T. McCanny, S. Shimizu, R.J. Clarke, D. Neely, K. Spohr, R. Chapman, R.P. Singhal, K. Krushelnick, M.S. Wei, and P.A. Norreys. Characterization of proton and heavier ion acceleration in ultrahigh-intensity laser interactions with heated target foils. *Physical Review E*, 70:036405, 2004.
- [173] R. Kodama, Y. Sentoku, Z.L. Chen, G.R. Kumar, S.P. Hatchett, Y. Toyama, T.E. Cowan, R.R. Freeman, J. Fuchs, Y. Izawa, M.H. Key, Y. Kitagawa, K. Kondo, T. Matsuoka, H. Nakamura, M. Nakatsutsumi, P. A. Norreys, T. Norimatsu, R.A. Snavely, R.B. Stephens, M. Tampo, K.A. Tanaka, and T. Yabuuchi. Plasma devices to guide and collimate a high density of MeV electrons. *Nature*, 432(7020):1005–1008, 2004.
- [174] Joseph W. Goodman. *Introduction to Fourier Optics*. Roberts & Company Publishers, 3 edition, 2004.
- [175] S. Akturk, X. Gu, P. Gabolde, and R. Trebino. The general theory of first-order spatio-temporal distortions of Gaussian pulses and beams. *Optics Express*, 13(21):8642–8661, 2005.
- [176] O Jäckel. private communication, 2012.
- [177] Y. Sentoku, E. d’Humières, L. Romagnani, P. Audebert, and J. Fuchs. Dynamic control over mega-ampere electron currents in metals using ionization-driven resistive magnetic fields. *Physical Review Letters*, 107:135005, 2011.

## Danksagung

Das Schreiben einer Doktorarbeit ist eine große Herausforderung, die man unmöglich allein bewältigen kann. Auf diesem Weg möchte ich mich bei allen die mich in den letzten Jahren unterstützt und zum Gelingen dieser Arbeit beigetragen haben von ganzem Herzen bedanken.

An erster Stelle bedanke ich mich bei Herrn Prof. Dr. R. Sauerbrey, der das interessante Feld der Laserteilchenbeschleunigung nach Dresden gebracht und mir die Möglichkeit gegeben hat, in der damals neugegründeten Gruppe mitzuarbeiten. Es war toll mitzuerleben, wie aus der anfangs drei Personen umfassenden Arbeitsgruppe ein großes Team mit nunmehr fast 30 Kollegen entstanden ist.

Besonders möchte ich Ulrich Schramm für die exzellente Betreuung dieser Arbeit im Verlauf der zurückliegenden Jahre danken. Er unterstützte mich mit Rat und Tat, ob bei Experimenten im Labor, beim Veröffentlichen der Ergebnisse oder auch gerne mal bei der Beschaffung eines Kinderfahrrads. In diesem Zuge gilt mein Dank auch Stephan Kraft für seine Unterstützung sowie das gemeinsame Kennenlernen der Laser-Plasma Physik und des Experimentierens mit einem Hochleistungslaser.

Tom Cowan möchte ich ebenfalls für die wissenschaftliche Betreuung meiner Arbeit danken. Seine ständige Bereitschaft begeistert über Plasmaphysik und neue Experimentideen zu diskutieren hat entscheidend dazu beigetragen, Interpretationen zu den hier gemessenen Daten zu entwickeln. Zudem bin ich Tom dankbar, dass er mich in die Kollaboration mit Julien Fuchs eingeführt hat und ich bei Experimenten am LULI System, bei denen ich viel vom Handwerk der Laserteilchenbeschleunigung gelernt habe, teilnehmen durfte.

Josefine Metzkes gebührt besonderer Dank für eine tolle Zeit beim Experimentieren, für viel Durchhaltevermögen während unzähliger, oft endloser Tage im Labor. Vielen Dank auch für die unschätzbare Unterstützung und Aufmunterung beim Schreiben der diversen Texte und fürs „Mitnachdenken“. Tom Richter sei an dieser Stelle ebenfalls für seine Unterstützung bei Laborarbeit und manchmal auch zäher Datenauswertung gedankt.

Thomas Kluge, unserem PIC-Simulanten, möchte ich für die vielen Stunden danken, die er in die theoretische Beschreibung der hier gezeigten Experimente gesteckt hat. Seine Hilfe war von entscheidender Bedeutung für die Interpretation der gemessenen Daten. Ähnliches gilt für Michael Bussmann, dem ich für viele Diskussion danke, die etwas Licht ins Dunkel der Laser-Plasma Wechselwirkung gebracht haben.

Jörg Pawelke, Christian Richter, Leo Karsch, Lydia Laschinsky, Doreen Naumburger, Michael Schürer, Elke Beyreuther und Melanie Oppelt möchte ich für die produktive und partnerschaftliche Zusammenarbeit bei den Zellbestrahlungsexperimenten danken. Besonders Jörg sei an dieser Stelle für sein Engagement während der ELBE Experimente in der ersten Zeit gedankt und dafür, dass er mir so manches Mal den Weg geebnet hat.

Ohne die Hilfe des Draco Laserteams um Stefan Bock und Uwe Helbig hätte wohl kaum eines der hier beschriebenen Experimente funktioniert, dafür vielen Dank. Aufgrund ihres hohen Engagements ist es gelungen aus unserem französischen Turn-Key-System einen ex-

perimenttauglichen Laser zu machen. Uwe sei außerdem für die abwechslungsreichen und bereichernden Debatten zu politischen wie auch erziehungstheoretischen Fragen gedankt.

Eine nicht ganz unbeträchtliche Zeit hat es gekostet die Laser- und Experimentieranlagen aufzubauen, was ohne die fantastische Hilfe der Institutswerkstatt wohl kaum möglich gewesen wäre. Deswegen gilt mein Dank dem Werkstattteam um Matthias Langer, Mathias Boeck, Marco Böse und Rolf Hensel. Ganz besonders sei Manfred Sobiella gedankt, der mit unerschöpflichem Ideenreichtum immer wieder Lösungen für ganz besonders knifflige Probleme findet.

Bernd Schmidt und Steffen Howitz danke ich für die Unterstützung bei der Entwicklung und natürlich der Herstellung der kleinen Laser-Targets, die die Basis für eine Reihe sehr anspruchsvoller aber auch sehr interessanter Experimente darstellten.

Bei Fabian Roeser und Alexander Debus bedanke ich mich für ihre Hilfe, mir die Schönheit von pulsfrontverkippten und räumlich gechirpten Laserpulsen näher zu bringen.

Axel Jochmann, Markus Löser und Jurjen Couperus danke ich vor allem für die Zeit abseits des Laboralltags. Wenn mal was nicht so richtig funktioniert, ist geteiltes Leid ja bekanntlich oft nur noch halbes Leid.

Besonders möchte ich mich bei meiner Familie und meinen Freunden bedanken, die mich immer und zu jeder Zeit bedingungslos unterstützt haben. Peter, danke ich für seine Hilfe erst als Praktikant und dann fürs Lesen dieser Arbeit. Vor allem meinen Eltern sowie Helga und Hans danke ich für die enorme Hilfe bei der Kinderbetreuung ohne die das Unterfangen Doktorarbeit wohl schon vor langer Zeit gescheitert wäre.

Mein größter Dank gilt meiner Frau Bine sowie meinen Kindern Emil, Olli und Ella, die immer Geduld mit mir haben, immer für mich da sind und mich immer wieder aufs Neue motivieren und inspirieren. Um sich erfolgreich durch ein solches Projekt wie eine Doktorarbeit zu kämpfen, bedarf es auch der nötigen Abwechslung um den Kopf frei zu bekommen, wofür ihr zweifellos sorgt, vielen Dank dafür.

## Eidesstattliche Erklärung

Hiermit versichere ich, Karl Zeil, geboren am 02.02.1982 in Dresden, im Rahmen meines Promotionsverfahrens an der Fakultät Mathematik und Naturwissenschaften der Technischen Universität Dresden und an Eides statt, dass

1. ich die vorliegende Arbeit ohne unzulässige Hilfe Dritter und ohne Benutzung anderer als der angegebenen Hilfsmittel angefertigt habe; die aus fremden Quellen direkt oder indirekt übernommenen Gedanken sind als solche kenntlich gemacht. Die Arbeit wurde bisher weder im Inland noch im Ausland in gleicher oder ähnlicher Form einer anderen Prüfungsbehörde vorgelegt.
2. ich die vorliegende Arbeit am Helmholtz-Zentrum Dresden-Rossendorf am Institut für Strahlenphysik unter der wissenschaftlichen Betreuung von Prof. Roland Sauerbrey angefertigt habe.
3. mir die geltende Promotionsordnung (Stand 23.02.2011, Fakultät Mathematik und Naturwissenschaften der TU Dresden) bekannt ist und ich diese anerkenne.

Dresden, June 26, 2013